DOKUZ EYLÜL UNIVERSITY
GRADUATE SCHOOL OF NATURAL AND APPLIED SCIENCES

BEHAVIOUR OF COMPOSITE MATERIALS UNDER IMPACT LOADING

by
Semih BENLİ

July, 2010
İZMİR

BEHAVIOUR OF COMPOSITE MATERIALS UNDER IMPACT LOADING

A Thesis Submitted to the
Graduate School of Natural and Applied Sciences of Dokuz Eylül University
In Partial Fulfillment of the Requirements for the Degree of Doctor of Philosophy in Mechanical Engineering, Mechanics Program

by
Semih BENLİ

July, 2010
İZMİR

Ph.D. THESIS EXAMINATION RESULT FORM

We have read the thesis entitled **"BEHAVIOUR OF COMPOSITE MATERIALS UNDER IMPACT LOADING"** completed by **SEMİH BENLİ** under supervision of **PROF. DR. ONUR SAYMAN** and we certify that in our opinion it is fully adequate, in scope and in quality, as a thesis for the degree of Doctor of Philosophy.

Prof. Dr. Onur SAYMAN

Supervisor

Prof. Dr. Ramazan KARAKUZU	Associate Prof. Dr. Mustafa TOPARLI
Thesis Committee Member	Thesis Committee Member
Associate Prof. Dr. Cesim ATAŞ	Prof. Dr. Ahmet AVCI
Examining Committee Member	Examining Committee Member

Prof. Dr. Mustafa SABUNCU
Director
Graduate School of Natural and Applied Sciences

ACKNOWLEDGMENTS

I would like to offer my thanks and my gratitude to my supervisor, Prof. Dr. Onur SAYMAN, for his excellent guidance, tolerant approach and continuous encouragement throughout the preparation of this study.

Special thanks also extend to my dissertation committee members, Professor Dr. Ramazan KARAKUZU and Associate Professor Dr. Mustafa TOPARLI, for their academic support and encouragement through my theses.

I would also like to express my appreciation for the financial support of The Scientific & Technological Research Council of Turkey (TÜBİTAK) (Project No: 107M332). Thanks to Izoreel firm for the manufacturing of the composite specimens.

I would like to thank Associate Professor Dr. Cesim ATAS, Assistant Professor Dr. Bülent Murat İÇTEN and Research Assistant Yusuf ARMAN for their academic support and encouragement through my theses.

I would like to thank all my coworkers in the Composite Research Laboratory and Mechanical Test and Research Laboratory.

I am very grateful to my parents for their understanding, support and love.

Semih BENLİ

BEHAVIOUR OF COMPOSITE MATERIALS UNDER IMPACT LOADING

ABSTRACT

In this study, low velocity impact tests on the glass/epoxy, carbon/epoxy and glass/carbon hybrid laminated composite plates at 20, 90 and -50 °C temperatures were performed to investigate impact behaviors of the laminates. Impact responses of the composite specimens were characterized in terms of impact parameters such as permanent deflection, maximum contact force, maximum contact time, energy to maximum contact force, and total energy absorption at low, intermediate, and high impact energy levels. Energy profile diagrams and force versus deflection curves were plotted for each temperature and specimen type. Impact tests on the saturated specimens kept in seawater for 7 months were also conducted at the same impact energy levels as that of dry specimens. The initial damage, perforation and propagation energies were obtained for each temperature and specimen type. The impacted specimens were observed by visual inspection. A high-intensity light was used to identify the projected delamination areas in the impacted glass/epoxy composite laminates. The photographs of the cross-sections of the impacted specimens were taken. Delaminated surfaces were observed by an optical microscope. There point bending tests on the impacted specimens were also performed. In addition, mechanical properties of unidirectional glass/epoxy and carbon/epoxy composite plates were determined at 20 and 90 °C temperature. Thermal residual stresses at 20, 90 and -50 °C temperatures were obtained by using ANSYS software and the effects of the residual stresses on matrix cracking damage before impact were analyzed. The results showed that impact behaviors of the laminated composites were affected by the different environmental conditions.

Keywords: Mechanical properties, laminated composite plates, low velocity impact test, thermal stress analysis, perforation energy, three point bending test

DARBELİ YÜKLEME ALTINDA KOMPOZİT MALZEMELERİN DAVRANIŞI

ÖZ

Bu çalışmada, tabakalı kompozitlerin darbe davranışlarını incelemek amacıyla, cam/epoksi, karbon/epoksi ve cam/karbon hibrit kompozit plakalar üzerine 20, 90 ve -50 °C sıcaklık koşullarında düşük hızda darbe testleri yapılmıştır. Düşük orta ve yüksek enerji seviyelerinde kompozitlerin darbe davranışları, maksimum kontak kuvveti, kalıcı deformasyon, maksimum kuvvete karşılık gelen enerji ve absorbe edilen enerji gibi darbe parametreleri açısından değerlendirilmiştir. Enerji profil diyagramları ve kuvvet deplasman eğrileri farklı numune tipi ve sıcaklıklar için çizilmiştir. Yedi ay deniz suyunda bekletilen numunelere de aynı darbe testleri yapılmıştır. İlk hasar, delinme ve hasar yayılma enerjileri her numune ve sıcaklık için elde edilmiştir. Hasarlı numuneler gözlemsel olarak incelenmiştir. Cam/epoksi kompozitlerde delaminasyon alanları yoğun ışık altında incelenmiştir. Hasarlı numunelerin orta kesitten fotoğrafları çekilmiştir. Delaminasyon yüzeyleri optik mikroskop altında incelenmiştir. Hasarlı numunelere üç nokta eğme testleri de yapılmıştır. Ayrıca, 20 ve 90 °C sıcaklıklarda tek yönlü cam/epoki ve carbon/epoksi kompozit plakaların mekanik özellikleri tespit edilmiştir. ANSYS programı vasıtasıyla 20, 90 ve -50 °C sıcaklıkta termal gerilmeler hesaplanmış ve bu gerilmelerin darbe uygulanmadan önceki matris kırılma hasarı üzerindeki etkileri analiz edilmiştir. Sonuçlar, tabakalı kompozitlerin darbe davranışının farklı ortam koşullarından etkilendiğini göstermiştir.

Anahtar Kelimeler: Mekanik özellikler, tabakalı kompozit plakalar, düşük hızda darbe testi, termal gerilme analizi, delinme enerjisi, üç nokta eğme deneyi

CONTENTS

Page

CHAPTER ONE
INTRODUCTION

Due to the advantages associated with their very large strength-to-weight and stiffness-to-weight ratios, composite materials are attractive for a wide range of applications. Increasingly, high performance engineering structures are being built with critical structural components made from composite materials. However, their behavior under impact loading is one of the major concerns (Tanaka & Kurokawa, 1996), since impacts do occur during manufacture, normal operations, maintenance and so on. Especially, unidirectional laminated plates are highly susceptible to the transverse impact loads resulting in significant damages such as matrix cracks, delaminations, and fiber fractures. Therefore, the impact problems of composites have become important. A dropped wrench, bird strike (Ma, Huang, & Chang, 1991) or runway debris can create localized delaminated areas owing to foreign object damage (FOD) (Takeda, 1985), by impacts that are frequently difficult to notice with the naked eye. Although this damage may seem innocuous in the stacking plates, it can result in premature catastrophic failure because of decreased strength caused by the impact loading. For example, when a laminate is subjected to an impact load, matrix cracks and interlamina delaminations may be generated simultaneously. For this reason extensive research has been carried out, on topics such as, foreign object damage (Reszczuk, 1973) damage tolerance (Challenger, 1986), impact loading and residual strength (Ishai & Shragi, 1990; Yang, Sim & Im, 1996), crack propagation direction in composites (Smith & Grove, 1989), and related impact damage (Malvern, Sun, & Liu, 1989). This is mainly the case for CFRP laminates used or of interest in aircraft and space structures, where the laminates may be subjected to air at −73 to 80°C (Young & Sung, 1986) or the space at −140 to 120°C (Advanced material committee, 1988).

In the literature, a lot of experimental, numerical, and analytical studies on the impact response of laminated composite structures in many aspects can be found. Among them, Sadasivam, & Mallick (2002), have studied on the low energy impact characteristics of four different E-glass fibers reinforced thermoplastic and

thermosetting matrix composites. Caprino, Lopresto, Scarponi & Briotti (1999), have carried out low velocity impact tests on carbon/epoxy laminates of different thicknesses. They have examined the force and absorbed energy at the onset of delamination, the maximum force and related energy, and penetration energy. Some experimental investigations have been carried out by Hosur, Abdullah & Jeelani, (2005) to determine the response of four different combinations of hybrid laminates subjected to low velocity impact loading. They have pointed out that there was considerable improvement in the load carrying capability of hybrid composites as compared to carbon/epoxy laminates with slight reduction in stiffness. Datta, Krishna & Rao (2004), have investigated the effects of variable impact energy and laminate thickness on the low velocity impact damage tolerance of GFRP composite laminates. Critical values of impact energy and laminate thickness were also defined. Baucom & Zikry (2005), have addressed an experimental study to understand the effects of reinforcement geometry on damage progress in woven composite panels under repeated impact loading. Fuoss, Straznicky & Poon (1998a, 1998b), have worked on the effects of key stacking sequence parameters on the impact damage resistance in composite laminates.

Wu & Chang (1989), have conducted a transient dynamic finite element analysis for studying the response of laminated composite plates subjected to transverse impact loading by a foreign object. They have calculated displacements, the transient stress and the strain distributions through the thickness of laminate during the impact event. A finite element analysis of fiber-reinforced composite plates subjected to low velocity impact has been also done by Tiberkak, Bachene, Rechak & Necib (2008). Cho & Zhao (2002), have investigated the effects of geometric and material parameters such as span to stiffness ratio, out-of-plane stiffness, stacking sequence on mechanical response of graphite epoxy composites under low velocity impact. Aslan, Karakuzu, & Okutan (2002, 2003), have done a numerical and experimental analysis to investigate the effects of the impactor velocity, thickness and in-plane dimensions of target and impactor mass on the response of laminated composite plates under low velocity impact. They have concluded that the peak force in an

impact event increases with the thickness of the composite as the contact time decreases.

Mitrevski, Thomson, Jones & Whittingham (2005, 2006), have investigated the effect of impactor shape on the impact response of composite laminates using a drop weight test rig. A very useful work regarding the effect of an initial pre-stress on the response of carbon–fiber/epoxy laminated plates subjected to low velocity impact has been carried out by Whittingham, Marshall, Mitrevski & Jones (2004). Prior to being impacted, the samples in their study were loaded either uniaxially or biaxially using a specially designed test rig. An energy profiling method, which has been used by some recently (Liu, 2004; Atas & Liu, 2008), seems to be useful to characterize some impact properties, e.g. penetration and perforation thresholds. Therefore, the damage process of individual laminates can be reconstructed from comparing the corresponding load–deflection curves, energy profile and images of damaged specimens. Aktas, Atas, Icten & Karakuzu (2008), investigated the impact response of unidirectional glass/epoxy laminates by considering energy profile diagrams and associated load–deflection curves. The results indicated that the penetration threshold for stacking sequence [0/90/+45/-45]s is found to be smaller than that of [0/90/0/90]s.

Poe, Portnova, Sankar & Jackson (1991), have stated that even low velocity impacts such as rock or hail impact can decrease tension and compression strength by as much as two-thirds. Lal (1982), has pointed out that transverse impacts can cause delamination, ply splits, fiber breakage, and to a less extent, fiber debonding and pull out. Short, Guild & Pavier (2002), have showed that low velocity impacts of fiber reinforced plastic composites cause a pattern of damage consisting in general of delamination, fiber breakage and matrix cracking. They explained that such damage is accidental and may go unnoticed; therefore, composites must be designed assuming impact damage exists. Sugun & Rao (2004), have used repeated drop tests with final delamination area maps to understand the impact damage tolerance of polymer composites. Their results showed that repeated drop weight impact tests

provide a very good understanding of the impact damage tolerance of polymer composites, and help to rank them on this basis.

Carbon fiber reinforced plastic composites have appeared as a major class of structural materials in a wide range of engineering fields. This is due to attractive mechanical properties such as high specific stiffness and high strength in addition to a relative high tolerance to environmental change. Unfortunately, they have very low energy absorption capacity when subjected to impact loading in transverse direction. This is mainly owing to the low strain to failure and low transverse shear strength of the carbon fiber and the brittle nature of the epoxy matrix. Since the early 1970s, researchers have been considering various methods for improving the low velocity impact response of carbon composites.

One of the ways to accomplish the improved impact resistance of composite materials is by hybridization. Hybrid composites consist of two or more types of reinforcements or matrices or both. By mixing different fibers, it is possible to combine the advantages of different fibers while simultaneously allaying their less desirable qualities. Normally, one of the fibers in a hybrid composite is a high modulus, high strength and high cost fiber such as graphite/carbon, and the second fiber usually is a low modulus fiber like Kevlar, E-glass or S-glass. Hybrid composites are attractive structural materials, because the composite properties can be customized to requirements. Other characteristics of hybrid composites are: cost effective utilization of different fiber materials, possible weight savings, reduced notch sensitivity, improved fracture toughness, longer fatigue life and improved impact resistance. Hybrid composites can be classified into two main categories: intermingled or intraply and interlaminated or interply (Naik, Ramasimha, Arya, Prabhu, & ShamaRao, 2001). Some researchers have made the studies on the impact properties of hybrid composites.

Wang, Jang, Panus, & Valaire (1991), have studied the fracture behavior of unidirectional laminated hybrid composites. They have studied single-matrix/double-fiber, double-matrix/single-fiber, and double-matrix/double-fiber hybrid composites

as well as their single-fiber/single-matrix control versions. The materials studied have been polyphenylene sulfide-graphite, polyphenylene sulfide-glass, epoxy-graphite. They have concluded that as the percentage of glass increases, the maximum load tolerated and impact energy absorbed by the material increases. The maximum load tolerated was the load corresponding to either a gross fiber failure at the back surface or an interlaminar crack across the composite sample. In addition, the intermixing of glass and graphite fiber plies helped decrease the sudden catastrophic failure mode. Jang, Chen, Wang, Lin, & Zee (1989), have studied the impact properties and energy absorbing capability of graphite composites hybridized with three types of plain weave fabric: polyethylene (PE), polyester (PET) and nylon, with epoxy resin. They have measured the impact load and the impact energy absorbed by the specimen upon penetration. They have observed that the hybrids containing PE fibers, which were of high strength and high ductility, were effective in both dissipating impact energy and resisting through penetration. They have also affirmed that for a particular material combination, stacking sequence is a major factor governing the overall energy absorbing capability of the hybrid structure. However, during the service life of the composite structure, low velocity impacts leading to other modes of failure such as delamination are also important considerations. Delamination and the other secondary modes of failure such as matrix cracking, debonding, etc. would lead to reduction in residual in-plane strength of impacted composites.

Novak & DeCrescente (1972), have observed that the addition of glass fibers to carbon/epoxy and boron/epoxy composites improves the impact strength by a factor of about three to five, which is higher than that predicted from the impact properties of the unmixed composites. Chamis, Hanson, & Serafini (1972), have studied glass/carbon hybrid composites and have observed that hybrid composites failed under impact by combined fracture modes: fiber breakage, fiber pullout and interply delamination. They also implied that as a result of this complex failure process, the impact resistance of hybrid composites may be synergistically increased over that predicted from the behavior of the separate constituents. Harris & Bunsell (1975), have conducted Charpy impact tests on unidirectional hybrid composite rod samples

containing glass reinforcements and carbon reinforcements. They have stated that the work of fracture by impact and the flexural modulus are both simple functions of composition corresponding to a mixture rule based on the properties of plain glass reinforced composites and carbon reinforced composites. In this study, the authors have not observed the advantages of hybrid effect.

Saka & Harding (1990), have carried out in-plane tensile impact studies on woven hybrid composites. They also used a simple laminate theory approach to predict the in-plane tensile impact behavior of woven hybrid composites. They observed that the tensile strength was higher at impact strain rate compared to that at quasi-static strain rate. Their experimental studies showed that the tensile strength of woven glass/carbon hybrid composites was more than that of only-carbon or only-glass composites. Kowsika & Mantena (1997), have studied the influence of hybridization on the characteristics of unidirectional glass/carbon epoxy composite beams. They have made studies using low velocity instrumented drop weight impact tests. They have experimentally determined that the strain to failure of glass/epoxy which is about 0.026 under static loading is found to increase to 0.044 under impact showing that glass fibers are highly sensitive to strain rate of loading. They have concluded that the peak contact force is the highest for the carbon outside hybrids when compared with the all-carbon, all-glass and glass outside hybrid composites.

Sonparote & Lakkad (1982), have used glass-carbon hybrids with various proportions of glass and carbon fiber volume contents and determined flexural, impact and interlaminar properties. Sreekala, George, Kumaran, & Thomas (2002) have used oil palm fibers with glass fibers in phenol formaldehyde with varying glass fiber loading and determined tensile strength, tensile modulus, impact and flexural strengths. They showed that these properties increased with increase in glass fiber loading. However, elongation at breakage and flexural modulus were found to decrease beyond 40% fiber loading. Kim, Sham, Sohn, & Hamada (2001) have treated glass fabric layers with different silane coupling agents and performed low-velocity impact and compression after impact tests. They concluded that there is a strong correlation between mode II interlaminar fracture toughness and the impact

damage performance of hybrid composites. Tjong, Xu, & Mai (2003), developed short glass fiber reinforced polypropylene hybrid composites toughened with styrene-ethylene-butylene-styrene (SEBS) elastomers to improve tensile, impact strengths as well as fracture toughness. Park & Jang (1998), have studied the effects of intraply hybridization on the mechanical performance of aramid/polyethylene fabric composites. They reported increased flexural strength, which was proportional to aramid fiber content and lower interlaminar shear strength as compared to pure polyethylene fiber composites. Thanomslip & Hogg (2003), have investigated penetration impact resistance of hybrid composites based on commingled yarn fabrics. The commingled yarn fabrics were composed of E-glass fibers and thermoplastic fibers blended together within the fiber bundles. They considered various thermoplastic fibers with different resin systems. They obtained significant increase in the total absorbed energy with hybrid composites as compared to plain glass composites. They concluded that plastic deformation in the thermoplastic fibers was the key factor in the improvement in energy absorption of the hybrid composites. Lee, Kang, & Park (1997), have investigated response of hybrid laminated composite plates subjected to low-velocity impact using shear deformation theory. They concluded that the fractional energy loss of two hybrid composite plates with same component ratio has different values according to the stacking sequence. A graphite-Kevlar-graphite plate has low-energy loss and a Kevlar-graphite-Kevlar plates much higher energy loss.

Tjong, Xu, Li, & Mai (2002), have studied Polyimide 6, 6 (PA6, 6) hybrid composites toughened with maleated styrene-ethylene-butylene-styrene (SEBS-g-MA) reinforced with 5%, 10%, 15%, 20% and 30% short glass fiber (SGF). They characterized impact fracture toughness using essential work of fracture concept under a speed of 3 m/s. They concluded that the hybrids exhibit much higher impact strength compared with PA6, 6 particularly those with low-SGF content. Cheon, Lim, & Lee (1999), have studied impact and interlaminar shear properties of glass fiber epoxy system hybridized with polyethylene fabric, polypropylene fabric, and not-silane treated glass fibers and Kevlar fibers. They changed the placement of the embedded materials with respect to the surface facing the impactor. They attained

80% higher impact energy absorption with 3.4% volume fraction of Kevlar-29 fiber and 40% increase with 5% volume fraction of not-silane treated glass fibers as compared to that of pure glass epoxy composite. Jang & Lee (1998), have studied two kinds of functionally graded materials by changing the spatial distribution of glass fiber (GF) and carbon fiber (CF) in polyphenylene sulphide (PPS) matrix. They carried out flexural and instrumented impact tests and showed that the flexural strength and flexural moduli increased in proportion to the relative content of CF to GF whereas the total absorbed energy decreased with increment of CF relative volume fraction. Morii et al., (1995), have investigated the impact property and damage tolerance of matrix hybrid composite laminates with different laminate constitution. The matrix hybrid composite laminates consisted of the laminae with a conventional epoxy resin and the laminae with a flexible epoxy resin modified from conventional resin. They concluded that the energy absorption increased exponentially with the increasing fraction of flexible resin if the flexible resin was placed at the impact face. Naik, Ramasimha, Arya, Prabhu & ShamaRao (2001), investigated impact behavior and post impact compressive characteristics of glass-carbon hybrid composites with alternate stacking sequences. They concluded that hybrid composites are less notch sensitive as compared to only carbon or only glass composites. Also, carbon-outside/glass-inside clustered hybrid configuration gave lower notch sensitivity compared to the other hybrid configurations.

Morais, Monteiro, & d'Almeida (2005), have studied on the effect of the laminate thickness upon the resistance of carbon, glass and aramid fabric composites to repeated low energy impacts. They have obtained the results for the different fiber reinforced composites and results were associated with the characteristics of the used fibers and fabrics. Caprino, Lopresto, Scarponi, & Briotti (1999), have performed low-velocity impact tests on carbon-fabric/epoxy laminates with different thicknesses. Finally, they have calculated the energy at delamination initiation by an analytical model, assuming that the total energy was shared in two parts, one of which was stored in flexure and the other in the material volume close to the contact zone.

Onal & Adanur (2002), have examined the tensile and flexural properties of glass-carbon fiber reinforced stitched hybrid composites after low-velocity impact. They have also investigated the effect of stacking sequence and fabric ply angle with composite axis on the mechanical performance of impacted hybrid composites. It can be seen from this study that tensile failure mechanism of damaged plies was affected by the interaction of reinforcement property, hybrid order and ply angle.

Gustin, Joneson, Mahinfalah, & Stone (2005), have investigated different combinations of carbon/Kevlar fiber and carbon/hybrid fiber at room temperature and at different impact energies. They showed that the addition of one layer of Kevlar and hybrid to the impact side of the facesheet improved the maximum absorbed energy and average maximum impact force.

Sevkat, Liaw, Delale, & Raju (2009), have studied the progressive damage behaviors of hybrid woven composite panels impacted by drop-weights at four different velocities by using a combined experimental and 3-D dynamic nonlinear finite element approach. The composite panels were damaged using a pressure-assisted Instron-Dynatup 8520 instrumented drop-weight impact tester. During these low-velocity impact tests, the time-histories of impact-induced dynamic strains and impact forces were recorded. 3-D dynamic nonlinear finite element (FE) software, LS-DYNA, incorporated with a proposed user-defined damage-induced nonlinear orthotropic model, was then used to simulate the experimental results of drop-weight tests. Good agreement between experimental and FE results has been achieved when comparing dynamic force, strain histories and damage patterns from experimental measurements and FE simulations.

The composites materials used as primarily load bearing components in marine and aerospace structures are often subjected to thermal loading due to the environment in addition to significant dynamic loads due to impact by foreign objects. The stressing conditions and the environments that a composite is subjected play a key role in determining its impact failure process. Therefore, low and high heat resistance of composites has to be given serious consideration. However, the

fracture behavior and mechanism of the laminate composites at low and high temperature levels are complicated when compared with those of the composite at room temperature. (Street, Russell, & Bonsang, 1988; Rojstaczer, Cohen, & Marom, 1985; Jang, Lieu, Chang, & Hwang, 1987)

The moisture, temperature, and/or humidity effect on the response of composite materials under various types of loadings is a very important field of study. Most of the modern day structures or body parts in aircrafts and automobiles are made of composite materials. These components have to work under different environmental conditions. Their ability to withstand the load may vary in different environmental conditions. .Hence, it is important for the researchers to establish a relationship between different conditions and their effects on the composites, especially under dynamic loading conditions like impact. However, a few studies have paid attention on the effect of extreme temperature and moisture conditions on the impact response of polymer matrix composites.

Levin (1986) have reported a decrease in delamination area with increase in temperature in the range between 40 and 70 °C for a carbon-fiber composite laminate subjected to high energy impact. In a similar high velocity impact study on cross ply laminates of polyethylene fiber/epoxy matrix system conducted by Zimmerman & Adams (1987), it was found that the damage initiation energy doubled when the temperature was increased from 50 to 100 °C. In contrast, laminates containing plain-weave fabrics showed very little influence of temperature on the total impact energy required for complete penetration of the specimen. Dutta (1994), analyzed the energy absorption of graphite/epoxy plates under low velocity impact using a Split Hopkinson pressure bar, and found a small dependence on temperature. Bibi, Leicy, Hogg, & Kemp (1994), have studied the impact performance of a number of thermoplastic and thermosetting matrix carbon fiber composites at room temperature, 70 and 120 °C.

Erickson, Alan, & Kenneth (2005), have investigated effect of temperature on the low-velocity impact behavior of composite sandwich panels constructed from glass-

fiber-reinforced facesheets surrounding both foam-filled and nonfilled honeycomb cores are impacted using a drop-weight impactor at three energy levels and three temperatures. The effects of core material, temperature, and impact velocity on the absorbed energy, peak impact force, and damage mechanisms were studied. The foam-filled samples were subsequently subjected to four-point bend tests to investigate the effect of impact velocity and temperature on the damage tolerance and residual strength of the composites. It was found that the temperature can have a significant effect on the energy absorbed and maximum force encountered during impact, although the effect of the impact temperature on the residual bending stiffness and strength of the composites was mixed.

Amin, Mohammad, Reza, & Brian (2007), have presented the results of a research on impacted sandwich composites with Kevlar/hybrid and carbon facesheets subjected to different temperatures. Testing was performed to determine bending and core shear stresses, maximum energy absorption, and ‘‘absorbing energy and moment parameter’’ (AEMP), ‘‘performance parameter’’ (PP), and compression strength after impact (CSAI). Specimens were tested at temperature range of 50 °C to 120 °C and were subjected to low velocity impact energies of 15 J, 25 J, and 45 J. Amin, Reza, Mohammad, & Reza (2006), have also performed an experimental study on Kevlar/fiberglass composite laminates subjected to impact loading at variable temperatures. The effect of temperature on maximum energy, elastic energy, maximum deflection, maximum impact force, ductility, and compression after impact was studied at several low velocity impact energy levels. The results obtained from both of the studies indicated impact performance of these composites was affected over the range of temperature considered. Testing at ambient temperature is not fully sufficient and therefore additional testing must be performed for full understanding of composite laminate properties.

Hee, Seok, Kyu, & Young (2001), studied the effect of temperature variations (-30 to 120 °C) on damage to orthotropic CFRP laminates at non-penetrating impact velocities (up to 100 m/s). They observed a linear relationship between the impact energy and the delaminated area, as well as an increase in the damage area as the

temperature decreases. Puente, Zaera, & Navarro (2002), have extended this study down to -150 °C. Both of them focused their work on high velocity perforating impacts (from 100 to 500 m/s), far away from the threshold impact energy. Moreover, when perforation occurs, the effect of the impact is highly localized around the contact area, leading to a smaller extension of the delamination. Go´mez, Zaera, Barbero, & Navarro (2005), have examined the response of carbon fibre-reinforced epoxy matrix (CFRP) laminates at low impact velocity and in low temperature conditions. They concluded that the embrittlement of the polymer matrix, together with the interlaminar thermal stresses generated in the laminate at low temperatures contributed to the generation and propagation of damage when subjected to impact loads. Thermally induced effects were seen to be more severe in the case of tape laminates than the woven fabric laminates.

Samuel, Patrick, Guoqiang, Su, & Michael (2007) have investigated impact and post impact response of glass fiber reinforced unidirectional and cross-ply laminated composite beams at low temperatures. Low velocity impact tests were conducted on the prepared specimens using an instrumented drop-tower impact machine at frozen temperatures 0 °C, -10 °C, and -20 °C. Temperatures at 20 °C and 10 °C were also used for comparisons. CAI tests were conducted using a hydraulic-servo MTS machine to determine the residual load carrying capacity of the impact damaged specimens. Damage observation was conducted to help in the understanding of the damage mechanism. The results showed that temperature has a significant effect on the low velocity impact responses of laminated composites. More impact damage is induced in specimens impacted at lower temperatures than those at higher temperatures. Also, cross ply laminates present a higher impact resistance than unidirectional laminates within the whole temperature range investigated.

Khalid (2006), examined the effect of fiber volume fraction and testing temperature on the impact energy of the woven roving aramid and glass/epoxy composites. The Charpy impact tests were conducted for a temperature range of 40 to -40 °C in intervals of 10 °C. Fiber volume fractions of 0.45, 0.55 and 0.65 were used. Results showed that a slight increase on the impact energy of steel and composite specimens with temperature increase for the range of 40 to -10 C. In

addition, it was found that the aramid/epoxy support higher impact energy than the glass/epoxy at all the tested temperatures.

Karasek, Strait, & Amateau (1995) have evaluated the influence of temperature and moisture on the impact resistance of epoxy/graphite fiber composites. They found that only at elevated temperatures did moisture have a significant effect on damage initiation energy and that the energy required to initiate damage was found to decrease with temperature. Also, these results indicated that moisture-induced degradation can significantly reduce the impact resistance of glass fiber reinforced epoxy composites. Parvatareddy, Wilson, & Dillard (1996), studied impact damage resistance and tolerance of two high performance polymeric systems after exposure to environmental aging. Specimens aged in nitrogen for 18 months had equivalent damage to those aged in air for only 2 months. For cross-ply laminates, the post-impact tensile strength values fell significantly (by maximum 70–75% of original composite strength) depending on ageing time, environment and impact velocity. Sala (2000), have found that barely visible impact damage, BVID, due to the impact of 1 J/mm (for 2.2-mm laminate thickness) increased the moisture saturation level from 4.8% to 6% for aramid fiber-reinforced laminates and enhanced the absorption rate. In the case of carbon fiber composite, there was no effect of BVID on moisture absorption curves.

Hirai, Hamada, & Kim (1998) have performed series of experiments on different silane treated glass fabric woven composites at temperatures ranging from -65 to 100 °C. They concluded that the overall impact response is dominated by reduced matrix stiffness and strength at elevated temperatures. The poor mechanical properties, in turn, reduce impact damage resistance and damage tolerance of the laminate in terms of incipient impact energy, threshold impact energy and threshold damage width. Imielin´ska & Guillaumat (2004) have studied the effect of water immersion aging on low-velocity impact behavior of woven aramid-glass fiber/epoxy composites. They reported that water immersion ageing affected microstructural integrity causing internal defects and the impact damage area was slightly less extensive in wet samples, which is suggested to be the result of propagation of interfacial damage

present in the wet samples prior to impact, which absorbed impact energy and inhibited delamination formation.

Mahesh et al., (2007), investigated low-velocity impact response of carbon/epoxy laminates subjected to cold-dry and cold-moist conditioning. Samples were subjected to different moisture conditioning before subjecting to impact loading which included cold-dry and cold-moist for a period of 3 and 6 months. Impact parameters like peak load, absorbed energy, time to peak load and energy at peak load were evaluated and compared. Ensuing damage was measured on the impact surface as well as the back surface. For the samples subjected to cold-dry conditioning, the 3 month conditioned samples showed an improved response for all the energy levels as the peak load values recorded were higher than the room temperature samples. However, the deteriorating effect of cold conditioning was evident after 6 months with samples withstanding lower peak load and increased damage size, although the load carrying capacity was higher at low energy level (15 J) for the samples. Samples subjected to cold–moist conditioning became plasticized, thus exhibiting more ductility and could withstand higher peak loads.

In this study, low velocity impact tests on the glass/epoxy, carbon/epoxy and glass/carbon hybrid laminated composite plates at 20, 90 and -50 °C temperatures were performed to investigate impact behaviors of the laminates. Impact responses of the composite specimens were characterized in terms of impact parameters such as permanent deflection, maximum contact force, maximum contact time, energy to maximum contact force, and total energy absorption at low, intermediate, and high impact energy levels. Energy profile diagrams and force versus deflection curves were plotted for each temperature and specimen type. Impact tests on the saturated specimens kept in seawater for 7 months were also conducted at the same impact energy levels as that of dry specimens. The initial damage perforation and propagation energies were obtained for each temperature and specimen type. The impacted specimens were observed by visual inspection. A high-intensity light was used to identify the projected delamination areas in the impacted glass/epoxy composite laminates. The photographs of the cross-sections of the impacted

specimens were taken. Delaminated surfaces were observed by an optical microscope. There point bending tests on the impacted specimens were also performed. In addition, mechanical properties of unidirectional glass/epoxy and carbon/epoxy composite plates were determined at 20 and 90 °C temperature. Thermal residual stresses at 20, 90 and -50 °C temperatures were obtained by using ANSYS software and the effects of the residual stresses on matrix cracking damage before impact were analyzed.

CHAPTER TWO
IMPACT TEST SYSTEMS

2.1 Introduction

To simulate actual impact by a foreign object, a number of impact test apparatuses have been suggested: Gas gun apparatus, drop weight tester, cantilevered impactor, and pendulum-type tester, as shown in Figure 2.1. The initial kinetic energy of the projectile is an important parameter to be considered, but several other factors also affect the response of the structure. A large mass with higher velocity may not cause the same amount of damage as a smaller mass with higher velocity, even if the kinetic energies are exactly the same. In one case, the impact might be localized in a small region surrounding the point of impact. Therefore, the selection of the appropriate test procedure must be made very carefully to ensure that test conditions are similar to the impact conditions to be experienced by the actual structure. Test systems classified by three main sections; low velocity, high velocity and hyper velocity (Abrate, 1998). Carrying out the hyper velocity test method is very difficult due to simulating the velocity, approximately 600 m/s and over, and test conditions. In this chapter, the low and high velocity test systems will be shown.

2.2 High Velocity Impact Test Systems

The most commonly test systems for high and ballistic velocities are gas gun test system and split Hopkinson bar test system. These test systems will be maintained below.

2.2.1 Gas Gun Test System

Gas gun test system is generally used for large structures and for high velocity ranging from 60 m/s to 240 m/s. The main features of a gas gun test system are shown in Figure 2.1.a. Generally, this test system has mainly four components as a pressure regulator, a tank, a solenoid valve and a speed sensing device. The cleared

gas by a gas filter travel to pressure regulator. The pressure regulator with two high and low pressure gauge and a low pressure valve. The high and low pressure gauges read the pressure inside the tank and the supplied pressure, respectively. The low-pressure valve regulates the output pressure of the tank. The pressure inside the tank is released by opening a solenoid valve. After that, projectile travels through the gun barrel and passes a speed-sensing device. This device is calculated the velocity of projectile just prior to impact. Sometimes a high speed camera may be used instead of speed sensing device to obtain the velocity of the projectile. When the gas has reached a pre-determined value the solenoid valve will be open and the accelerated impactor will be down the barrel to strike a specimen (Abrate, 1998; Amid, 2001).

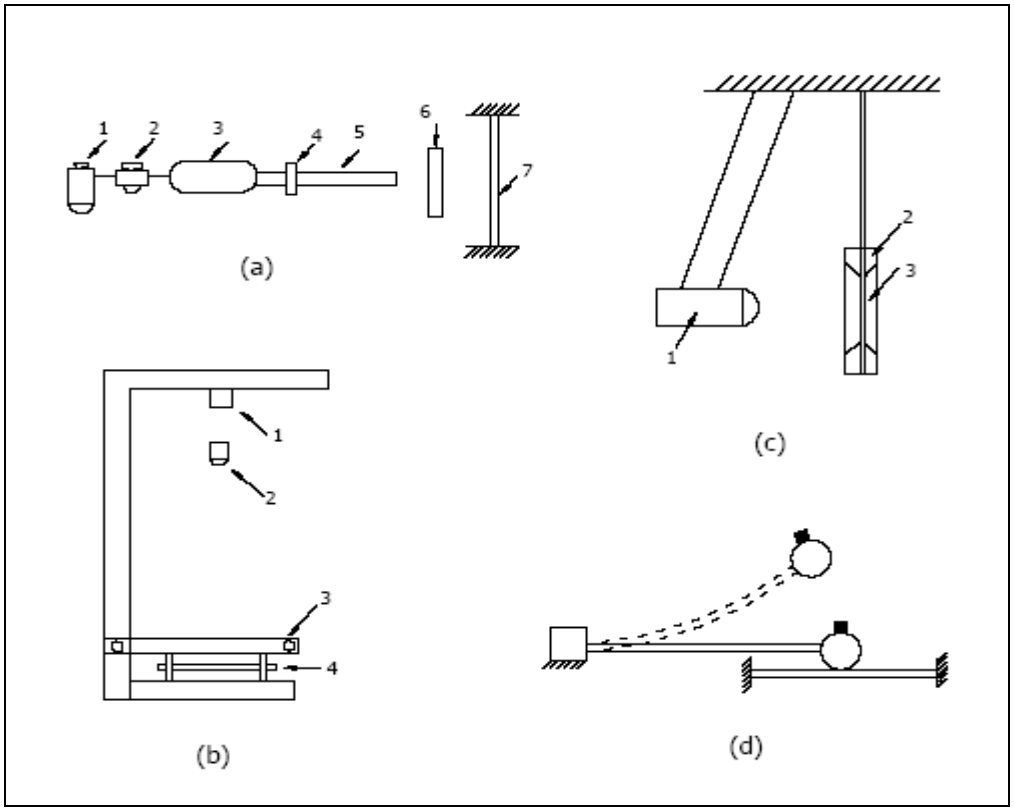

Figure 2.1 a) Gas gun apparatus: (1) air filter, (2) pressure regulator, (3) air tank, (4) valve, (5) tube, (6) speed sensing device, (7) specimen; b) Drop weight tester: (1) magnet, (2) impactor, (3) holder, (4) specimen; c) Pendulum-type tester: (1) impactor, (2) specimen holder, (3) specimen; d) cantilevered impactor

2.2.2 Split Hopkinson Bar Test System

The split Hopkinson bar test system is a high velocity test system which is developed to simulate the transverse impacts on composite laminated plates. This test system is mainly composed of an air gun, an input bar, base plate for support condition and data acquisition system. In this test system; an impactor, accelerated by the air gun, hits the center of the input bar.

Generally, the end of the input bar is hemispherical and has a diameter of 12.7 mm. The velocity of the impactor before the impact was measured using the phototransistor. The signals from the strain gauges on the input bar were stored in a data recorder. The load acting on the specimen, the impactor velocity and the specimen displacement are obtained by using the recorded data which are stored from strain gauge (Houde, 1990).

2.3 Low Velocity Impact Test Systems

The most common test systems for low velocity impact tests are Charpy and Izod test systems, dart or pendulum test method, cantilevered impact test method, and drop weight impact test method.

2.3.1 Charpy and Izod Test Systems

The earliest test systems used for low velocity impact testing is Charpy and Izod test systems. Both systems were originally designed for the testing of metallic materials. For the Charpy test method; a beam is rested freely against two anvils and struck in the center by a pendulum. Charpy specimens may be machined with *U* and *V* notches in the centre of the beam opposite the direction of strike, as shown in Figure 2.2.a. Charpy test method may be suitable for relative ranking of composite. However, it is unsuitable for glass/epoxy since this material is not sensitive to notches in either laminate direction (Amid, 2001; Reid & Zhou, 2000; Rydin, 1996).

The Izod test method is still commonly used for polymers. The Izod test method is similar to the Charpy test method except that the notch is near the fixed end of the specimen while the impactor strikes the free end of the specimen as shown in Figure 2.2.b. Potential energy is converted to kinetic strike energy during descent of the impactor. The energy absorbed by the specimen is measured by the height of the swinging pendulum. In either test, and with any material, the impact energy may be overestimated because energy is stored elastically in the specimen prior to failure. Impact energy can be expressed for a plastic or a composite as $U=E/b(d-c)$. Where U is the impact energy, E is the energy registered in the test, for a specimen of width b, and height d, containing a notch of depth c (Amid, 2001; Ellis, 1996; Reid & Zhou, 2000).

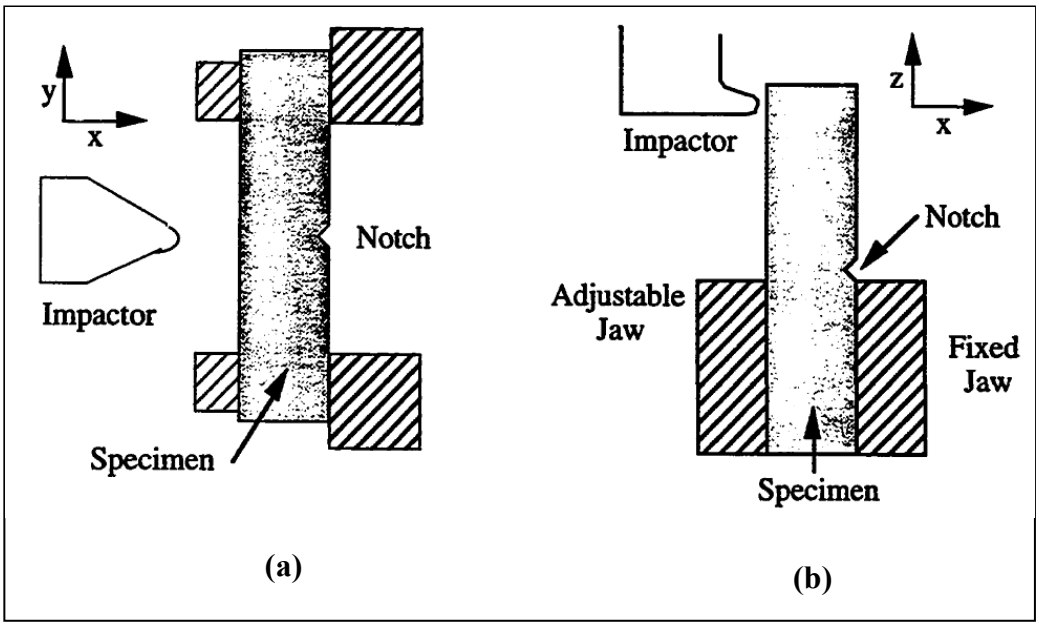

Figure 2.2 a) Charpy pendulum and b) Izod pendulum test system

2.3.2 Dart or Pendulum Test Systems

Falling dart test is a popular method, which is obtaining the impact energy. This test method was originally developed for rigid plastics. The test sample for falling dart test is 60 mm in diameter or 60x60 mm square and a range in 1-4 mm thickness.

Sample is clamped on a hollow steel cylinder with an inside diameter of 40 mm. The steel striker has a semi-circular head and is allowed to fall from height of up to 2 m onto the specimen. The maximum velocity in this test method is 6.3 m/s. An advance dart impact test has an accelerometer in the impactor tup for recording the load, target deflection and absorbed energy (Reid & Zhou, 2000; Rydin, 1996).

Pendulum-type test systems are also used to create low-velocity impacts. This test method consists of a steel impactor equipped with force transducers. The advantage of method is capable with measuring both impact and rebound velocity. The handicap of this test method; the acceleration of the tup at time that impact velocity was measured was not zero, in fact the acceleration was constant during the whole drop (Abrate, 1998; Herup, 1996). The test system is shown schematically in Figure 2.1.c.

2.3.3 Cantilevered Impact Test System

Literature review show the cantilever impact test system is not a commonly used test method. In this test system, impactor for which a 1-in. diameter steel ball is mounted at the end of a flexible beam which is pulled back and then released to be the cause of impact on the sample (Figure 2.1.d).

2.3.4 Drop Weight Impact Test System

In recent years, the drop-weight test system has become the preferred technique for impact testing of composites because a greater range of testing parameters is possible. Drop weight test system is composed of three main components which are a dropping crosshead, two steel guide columns for movement of dropping crosshead, and a specimen supported fixture to provide boundary condition. Supported fixture is attached the T-grooved base plate by movement in T-channel for safety. A dropping crosshead also consists of adjustable weight, a rigid impactor which has generally 12.7 mm hemispherical nose, and a load cell mounted between the dropping crosshead and the rigid impactor. Generally, the impactor was released from a

chosen height and dropped freely on the specimen. To change the impact energy, the crosshead was increased or decreased. Crosshead can be filled by additional weight for a request energy level. However, for a highest impact velocity the crosshead was raised to the highest point and springs can be used. When the specimen can not absorbed all of the energy, which is the impactor has, impactor strikes on the specimen more than one. At this time, a control system including brakes, namely called anti rebounding system, may be used to stop multiple hits (Dang, 2000; Herup, 1996). Schematic illustration of drop-weight test system is given in Figure 2.3.

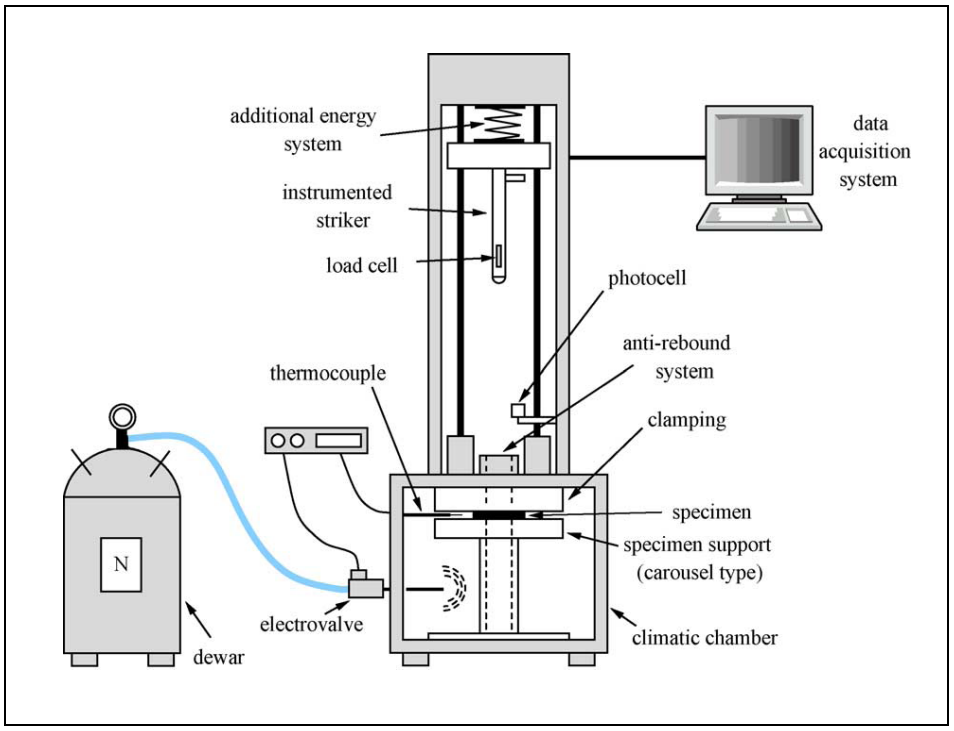

Figure 2.3 Drop-weight test system

CHAPTER THREE
LOW-VELOCITY IMPACT DAMAGE

3.1 Introduction

Composite materials are being increasingly used in different engineering fields due to their inherently high specific mechanical properties such as corrosion resistance, light weight, high strength and stiffness, etc. Due to completely different material specifications between metals and composites, the impact behavior of structures made by these materials differs inherently. Metals show visible damage caused by impact mainly on the surface of structures, while damage is hidden inside composite structure especially when subjected to low velocity impact. This invisible form may cause serious decrease in material strength which can be created during production, repair, maintenance, and small particle crashes to the composite body. Therefore, the effects of foreign object impacts on composite structures must be understood, and proper measures should be taken in the design process to account for these expected events. Concerns about the effect of impacts on the performance of composite structures have been a factor in limiting the use of composite materials.

In this section, general overview about low velocity impact damage has discussed. The morphology, development and the parameters that effects damage has been given with delamination prediction and experimental methods has explained.

3.2 Morphology of Low Velocity Impact Damage

For impacts that do not result in complete penetration of the target, experiments indicate that damage consists of delaminations, matrix cracking, and fiber failures. Delaminations, that is, the debonding between adjacent laminas, are of most concern since they significantly reduce the strength of the laminate. Experimental studies consistently report that delaminations occur only at interfaces between plies with different fiber orientations. If two adjacent plies have the same fiber orientation, no delamination will be introduced at the interface between them. For a laminate

impacted on its top surface, at interfaces between plies with different fiber orientation, the delaminated area has an oblong or “peanut” shape with its major axis oriented in the direction of the fibers in the lower ply at that interface. This is illustrated schematically in Figure 3.1. It must be noted that delamination shapes often are quite irregular and that their orientation becomes rather difficult to ascertain.

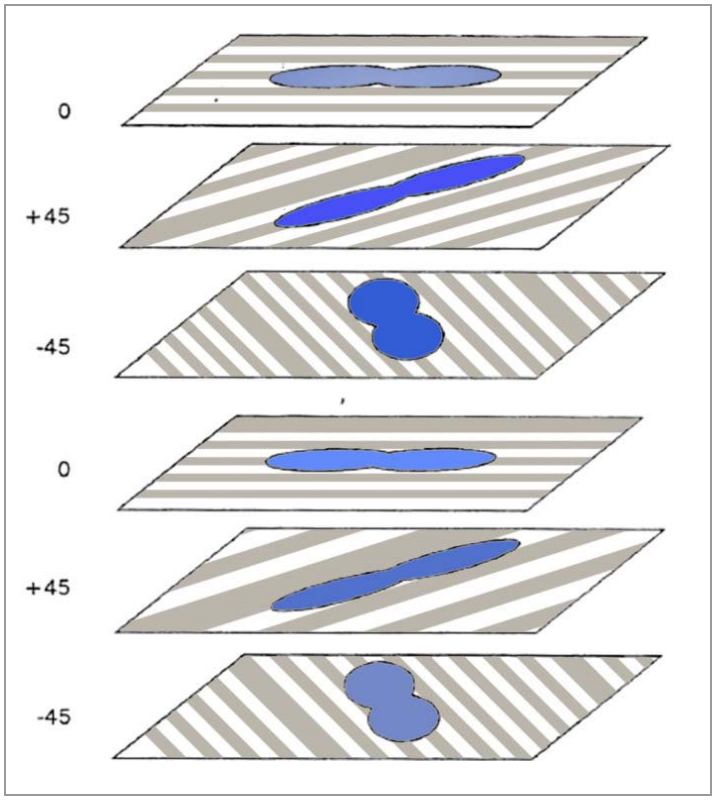

Figure 3.1 Orientation of delamination

Several investigations revealed that, delaminations occur when the contact force reaches at a threshold value. This value could not be predefined including all laminates or a specified orientation. The threshold value can only be obtained by experiments. However, producing completely identical specimens is not possible, so that, the threshold level of the initial contact force can be differ from one to another. The experimental studies indicate that delamination starts with the first discontinuity in the contact force history that indicates the threshold contact force value. (Lindsay & Wilkins, 1991) The delaminated area usually is plotted against the initial kinetic

energy of the impactor, and after a small threshold value is reached, the size of the delaminations increases linearly with the kinetic energy.

After impact, there are many matrix cracks arranged in a complicated pattern that would be very difficult to predict, but it is not necessary to do so since matrix cracks do not significantly contribute to the reduction in residual properties of the laminate. However, the damage process is initiated by matrix cracks which then induce delaminations at ply interfaces. Two types of matrix cracks are observed: tensile cracks and shear cracks (Figure 3.2). Tensile cracks are introduced when inplane normal stresses exceed the transverse tensile strength of the ply. Shear cracks are at an angle from the midsurface, which indicates that transverse shear stresses play a significant role in their formation. For thick laminated plates, because of the high and localized contact stresses, matrix cracks are first produced in the first layer which is impacted by the impactor. In this case, damage progresses like a pine tree pattern from the top to down (Figure 3.3.a). For thin laminated plates, matrix cracks can be introduced in the lowest layer due to the bending stresses in the back side of the laminate (Figure 3.3.b). At this case, damage again starts with a pattern of matrix cracks and delaminations (Abrate, 1998).

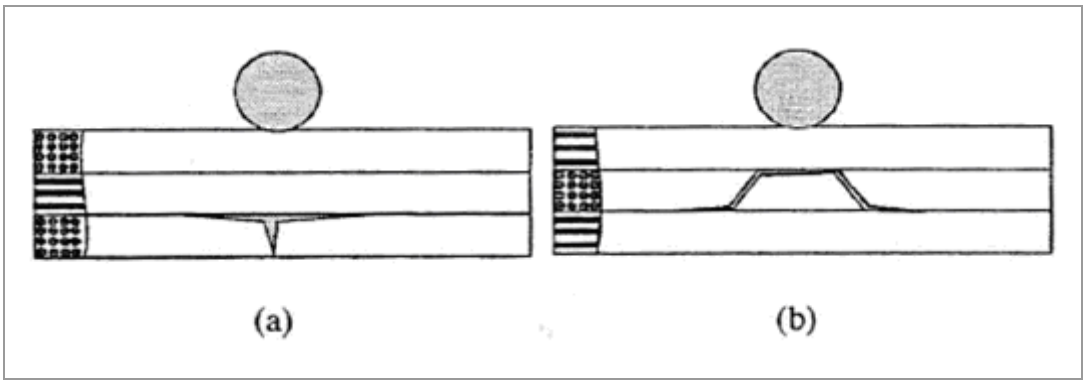

Figure 3.2 Two types of matrix cracks: a) tensile crack, b) shear crack

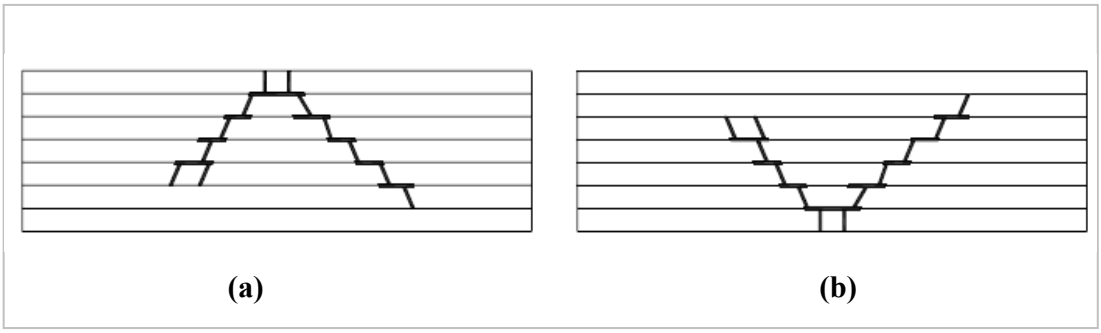

Figure 3.3 Pine tree (a) and reversed pine tree (b) damage patterns

3.2.1 Damage Development and Qualitative Models for Predicting Delamination Patterns

Two simple models have been put forward to explain why delaminations appear when laminates are subjected to localized loads. Both approaches are based on the fact that the laminate is made up of several orthotropic layers. Each layer tends to deform in a particular way, and transverse normal and shear stresses applied at the interfaces constrain the layup to behave as one plane. When these interlaminar stresses become too large under concentrated contact loads, delaminations are introduced.

Liu (1988) studied the delamination of two-layer plates and proposed a "bending stiffness mismatch" model to predict the orientation, size and shape of the delaminations based on the premise that delaminations occur because the sub-laminates above and below a given interface have different bending rigidities. Because of the anisotropy and of the different fiber orientations, this difference or "mismatch" in bending rigidities is different in different directions. In the experiments conducted to validate the model, the length and width of the specimens were kept the same, they were held in the same holder, and were subjected to the same impact. This way, the effect of difference in fiber orientation in the two plies on delamination at the interface could be isolated from other factors that could affect damage size. It is postulated that delaminations occur because of differences in bending rigidities between the two plies. Mismatch coefficients are defined as

$$M = \frac{[D_{ij}(\theta_b) - D_{ij}(\theta_t)]}{[D_{ij}(0^o) - D_{ij}(90^o)]} \quad (1)$$

where the D_{ij} are the components of the bending rigidity matrix D relating moment resultants to plate curvatures. Each ply is considered separately, so D_{ij} (Θ_b) is the rigidity of the bottom layer acting alone, and the subscript t refers to the top layer. While a mismatch coefficient can be defined for each bending coefficient D_{ij}, usually only D_{11} is considered. The denominator is simply introduced to nondimensionalize M; for two-layer plates, M=1 when the angle difference is 90°.

Another simple way to explain why two layers with different fiber orientations should delaminate when subjected to concentrated transverse loads was presented by Lesser & Filippov (1991). The transverse displacements of a simply supported rectangular plate consisting of a single composite layer with fibers oriented in the 0° direction subjected to a concentrated force applied in the center can be calculated using the Navier solution. The same problem was solved again for a fiber orientation of 90°. If two layers are stacked on top of each other but not bonded together, the two layers would separate under load because they deform differently. The difference between the displacements of the two layers has the same shape as the delaminations at the interface between the same two layers if they were boned together. The idea behind this simple explanation is that when the two layers are bonded together, interlaminar stresses develop on the interface in order to force these layers to deform as a single plate. High interlaminar stresses are expected to cause delaminations.

3.3 Parameters Affecting Impact Damage

The extensive experimental work performed to date produced an understanding of which parameters affect the initiation and growth of impact damage. Material properties affect the overall stiffness of the structure and the contact stiffness and therefore will have a significant effect on the dynamic response of the structure. The

thickness of the laminate, the size of the panel, and the boundary conditions are all factors that influence the impact dynamics, since they control the stiffness of the target. The characteristics of the projectile - including its density, elastic properties, shape, initial velocity, and incidence angle - are another set of parameters to be considered. The effects of layup, stitching, preload, and environmental conditions are important factors that have received various degrees of attention (Abrate, 1998).

3.3.1 Material Properties

The elastic properties of the material (E_1, E_2, ν_{12}, G_{12}), along with the lamination scheme, define the overall rigidities of the plate which greatly influence the contact force history. As discussed earlier, the ratio E_1/E_2 has a major effect on the bending stiffness mismatch coefficient between plies with different fiber orientations. The transverse modulus E_2 has a major effect on the contact stiffness. Lowering the contact stiffness also lowers the contact forces and increases the contact area, which in turn significantly affects the stress distribution under the impactor. Anisotropy in elastic properties and coefficients of thermal expansion affect impact resistance because of the residual thermal stresses developed during the curing process.

The threshold kinetic energy is strongly influenced by the properties of the matrix and is essentially independent of the properties of the fibers, the layup, and whether woven or unwoven layers are used. Damage is initiated by matrix cracking; when a matrix crack reaches an interface between layers with different fiber orientations, delamination is initiated. Because the elastic modulus of the reinforcing fibers is usually much higher than that of the matrix, these fibers appear to be essentially rigid. Therefore, the type of fibers being used does not seem to affect the onset of matrix cracking and delaminations. For higher levels of impact energy, the properties of fibers and the stacking sequence become important.

3.3.2 Target Stiffness

Target stiffness depends on material properties, as already mentioned, but also on the thickness of the laminate, the layup, its size, and the boundary conditions. The stiffness of the thickness has a significant effect on the magnitude of the maximum contact force which, of course, will affect the extent of the damage induced.

3.3.3 Projectile Characteristics

While a lot of studies consider the effect of several parameters during impacts generated by a single impactor, the size and shape of the impactor, the material it is made of, and its angle of incidence relative to the surface of the specimen are all factors that will have a strong influence on the impact response of the specimen.

3.3.4 Layup and Stitching

The importance of the stacking sequence on the impact resistance of laminates was first demonstrated by Ross & Sierakowski (1973). In a unidirectional laminate, since the reinforcing fibers are all oriented in the same direction, no delamination occurs. For two plates with the same thickness but with different stacking sequences, the one with the higher difference of angle between two adjacent plies will experience higher delamination areas. Increasing the thickness of each layer will also lead to increased delaminations. Increasing the difference between the longitudinal and transverse moduli of the material leads to higher bending stiffness mismatching and therefore increased delamination. However, damage initiation is matrix- and interface-dependent and therefore has little or no dependence on the stacking sequence. The peak load reached during impact, or the energy at peak load, is strongly dependent on the stacking sequence.

Stitching is used to introduce through-the-thickness reinforcement but in a different way than with weaving or braiding. The laminated structure is preserved, and stitching can be performed on either a prepreg or a preform. Stitching density

and pattern and properties of the thread can be varied to improve delamination resistance. Stitching of laminates prior to curing limits the size of delamination when the composite is subjected to out-of-plane loading and improves its resistance to transverse fracture when subjected to inplane loading. Dry preform stitching improves the compression-after-impact strength for two reasons. First, during impact, stitching arrests delaminations and therefore limits the damage size. Second, during compression-after-impact (CAI) tests, stitching prevents the growth of delaminations. However, some drawbacks are also present. Fiber damage can be introduced by needle penetration during stitching, by waviness of the fibers, and by introduction of resin-rich pockets, which cause stress concentrations and can reduce the strength of the laminate. Therefore, the extra manufacturing step of stitching the laminate to improve delamination resistance must be done carefully to minimize the reductions in inplane properties.

3.3.5 Preload

Schoeppner (1993) conducted a series of experiments to determine the effect of a tensile preload on the damage resistance of graphite-epoxy laminates using a dropweight tester. The stiffening effect of the pre-tension is shown to decrease the time required to reach the maximum impact load and to increase the indentation depth. The maximum load was insensitive to the preload. It must be noted that in these experiments, the mass of the impactor was 13.95 kg and the kinetic energy of the impactor was 80 J. These impacts resulted in partial or complete penetration, which may explain the results concerning the independence of mass load on pre-tension whereas earlier studies of laminates with initial stresses showed a strong dependence. Phillips, Park, & Lee (1990) conducted impact experiments on ceramic matrix composites under preload and showed that applied tensile loads drastically reduce the impact energy required to produce total fracture of the specimen.

3.3.6 Environmental Conditions

Changes in temperature and moisture content are known to affect both stiffness and strength of composites. It is logical to expect that impact resistance will also be affected by environmental factors.

3.4 Damage in Thick Laminates

When thick laminates are subjected to low-velocity impacts, bending deformations can generally be neglected and the laminates can be considered as semi-infinite bodies. The maximum impact force determined from an impact dynamic analysis is assumed to be distributed on the surface according to Hertz theory of contact.

3.5 Damage in Thin laminates

Often one is interested in determining the overall size of the damage created by a given impact, since damage size affects the residual properties of the structure. Damage is introduced only after the impact force reaches a minimum level. Therefore, it is also desirable to be able to predict this threshold impact force level. There are two simple methods for performing those tasks (Abrate, 1998).

The first approach, proposed by Dobyns (1980) and Dobyns & Porter (1981), is aimed at predicting the overall damage size. It is based on the premise that delaminations, which are the critical component of impact damage, grow because of high transverse shear stresses in the vicinity of the impactor. The idea is to determine the distribution of the transverse shear force resultant around the point of impact and to use an appropriate failure criterion to estimate the size of damaged zone.

The second approach deals with the prediction of the threshold value of the contact force that corresponds to damage initiation. When the damage area is plotted versus the maximum impact force, there is a clear sudden increase in damage size

once the load reaches a critical value P_c. Below this value; the damage area is small due to Hertzian surface damage. P_c corresponds to the onset of delaminations.

3.6 Damage Initiation

Once an accurate determination of the stress distribution is available, an appropriate failure criterion must be used to determine the location of the first matrix crack (Abrate, 1998). One approach is to determine the maximum tensile stress transverse to the fibers for each ply. Failure is predicted using a maximum stress criterion. That is, tensile matrix failure occurs when this maximum stress exceeds the tensile strength in the transverse direction. Hashin's failure criterion was used by several authors to predict the appearance of matrix crack:

$$\frac{1}{Y_t^2}\left(\sigma_{yy}+\sigma_{yy}\right)^2+\frac{1}{S^2}\left(\sigma_{yz}{}^2-\sigma_{yy}\sigma_{zz}\right)+\frac{1}{S^2}\left(\sigma_{xy}{}^2+\sigma^2{}_{xz}\right)=e^2{}_M \qquad (10.1)$$

Where Y_t is the transverse normal strength in tension and S is the transverse shear strength. The z-axis is normal to the laminate, and the x- and y-axes are local coordinates parallel and normal to the fiber direction in the layer under consideration. Failure occurs when e_m becomes larger than or equal to one. Since the transverse normal stress is usually small, σ_{zz} can be neglected in (10.1) For the purely two-dimensional problem of a beam subjected to a cylindrical impactor, σ_{xz} is also zero and the criterion can be simplified further:

$$\left(\frac{\overline{\sigma}_{yy}}{Y}\right)^2+\left(\frac{\overline{\sigma}_{yz}}{S_i}\right)^2=e^2{}_M \qquad (10.2)$$

where Y and S_i are the in-situ transverse normal and shear strengths.

3.7 Experimental Methods for Damage Assessment

Many techniques have been developed to determine the extent of impact-induced damage in composite structures.

3.7.1 Nondestructive Techniques

Methods capable of detecting the presence of eventual impact damage over the whole structure are needed. It is necessary to determine if damage is present, where it is located, and its extent. With translucent material systems such as glass-epoxy or Kevlar-epoxy composites, impact damage can be observed using strong backlighting. The size and shape of delaminations and the presence of matrix cracks can be detected by visual observation.

Other material systems such as graphite-epoxy are opaque, and thus this visual inspection approach cannot be used. Whole-field nondestructive methods such as ultrasonic imaging or radiography are used to visualize internal damage over large areas. C-scans and traditional x-rays provide a projected image of the damage zone and are useful in delineating the extent of the damage, but many of the features of the damage area are lost. It is important to understand how delaminations are distributed through the thickness, their size and orientation, and how they might be connected through intraply cracks. This knowledge provides a basis for developing a model for damage development during impact. Improved ultrasonic inspection techniques capable of resolving the distribution and size of delaminations through the thickness of the specimen have been developed.

3.7.1 Destructive Techniques

Detailed maps of impact damage can be obtained by sectioning several strips of material at different locations and orientations throughout the impacted zone. After careful preparation, microscopic examinations of each section are used to construct

detailed maps of delaminations at each interface and of matrix cracks in each ply. The use of micrographs in documenting impact damage is reported in many studies. Typically, slices are cut with a diamond lapidary saw using a water spray to minimize local heating, and then mounted in epoxy resin and ground on successively finer abrasive silicon carbide paper

With the often-used deply technique (Levin, 1986), a gold chloride solution with an isopropyl carrier is used to infiltrate the damaged area. If the surface damage is not sufficient for the solution to penetrate, 1 mm holes can be drilled through the laminate. After drying, a precipitation covers the fracture surfaces. The matrix is pyrolysed in an oven at about 420 C, and afterwards the laminate can be separated into individual laminas. Delaminations and matrix cracks can be observed under an optical microscope.

CHAPTER FOUR
PRODUCTION OF THE LAMINATED COMPOSITE PLATES AND MECHANICAL TEST PROCEDURE

4.1 Production of the Laminated Composite Plates for Impact Tests

The composite plates produced for impact tests are classified into three categories: Glass/epoxy composite plates, carbon epoxy composite plates and glass/carbon hybrid composite plates. Fiber reinforcement materials were selected as unidirectional E-glass fabric having weight of 509 g/m^2, unidirectional and woven carbon fabric having weight of 330 g/m^2. For matrix materials, epoxy CY225 and hardener HY225 are mixed. These composite plates having different stacking sequences were manufactured by using a hand lay-up method at Izorel Firm.

This method consisted of laying down the fabric layer by layer and pouring the epoxy over the fabric and then consecutively spreading the epoxy over the surface with a squeegee. Then another layer of fabric is placed on top of the previous layer and the process is repeated until the desired number of layers is obtained.

After applying this method, these composite plates were cured by using a hot lamination press at 120 °C for 2 hours under a pressure of 0.15 MPa. Then, they were cooled to room temperature at the same pressure.

The specimens of 100×150 mm^2 were prepared for impact tests by cutting from the produced composite laminates in size of 1×1 m^2. All specimens were cleaned from dust. Their orientation angles, nomenclatures, impact test temperatures and impact energy values were tagged on each of the specimens. The specimens types can classified into three different groups. First group consist of glass/epoxy composite plates in stacking sequences $[0/0/90]_s$, $0/90/45]_s$, $[90/0/0]_s$, $[90/0/0/90]_s$, $[90/0/45/45]_s$ and $[90/0/45/-45]_s$. The nomenclatures of the specimens are C1, C2, C3, G1, G2 and G3, respectively. Thicknesses and densities of the composite laminates are given in Table 4.1.

Carbon/epoxy laminated composite plates with lay ups of $[90/0/0/90]_s$ and $[90/0/45/45]_s$ constitute second group. Nomenclatures of the specimens are K1 and K2, respectively. The specimen types and their properties are given in Table 4.2.

Finally, the third group consists of cam/carbon glass hybrid composites. They are shown in Table 4.3. For K3, K4 and K5 hybrid composite laminates, carbon woven fabric consisting of twill weave was used as reinforcement material on upper and lower layers while using unidirectional reinforced glass fibers on six inner layers. H4, H5 and H6 specimens have unidirectional carbon and glass fiber reinforcement materials. K6 and K7 laminates were in symmetric and antisymmetric stacking sequences, respectively to compare impact responds of the laminates in terms of symmetric and antisymmetric stacking sequences. Finally, woven hybrid composites with lay ups $[GW/GW/CW/CW]_s$ and $[CW/CW/GW/GW]_s$, were produced to compare them in terms of impact behavior and resistance. The nomenclatures of the laminates are W1 and W2, respectively. In the laminates, the weights of woven carbon fiber and woven glass fibers used as reinforcing materials are 200 and 270 g/m^2, respectively.

Carbon fabric used as reinforcing material for hybrid and carbon/epoxy composite plates has weight of 330 g/m^2. While the weights of E- Glass fabrics used as reinforcing material are 509 g/m^2 for H3, H4, H5, K3, K4 and K5 hybrid laminates and G1, G2, G3 glass/epoxy laminates, 250 g/m^2 for K6 and K7 hybrid laminates. Therefore, thicknesses of K6 and K7 hybrid laminates are lower than the other specimen types. Herein, the volume fractions of specimens have the close values, except for K6 and K7 laminates.

Table 4.1 Glass/Epoxy Laminated Composites with six and eight layers

Layup	Nomenclature	Thickness (mm)	Density (g/cm^3)
$[0/0/90]_s$	C1	1,33	1,797
$[0/90/45]_s$	C2	1,34	1,773
$[90/0/0]_s$	C3	1,32	1,778
$[90/0/0/90]_s$	G1	2,81	1,907
$[90/0/45/45]_s$	G2	2,80	1,882
$[90/0/45/-45]_s$	G3	2,83	1,904

Table 4.2 Carbon/Epoxy Laminated Composites with eight layers

Layup	Nomenclature	Thickness (mm)	Density (g/cm^3)
$[90/0/0/90]_s$	K1	2,35	1,526
$[90/0/45/45]_s$	K2	2,39	1,576

Table 4.3 Glass/Carbon epoxy laminated hybrid composites with eight layers

Layup	Nomenclature	Thickness (mm)	Density (g/cm^3)
$[C_{90}/G_0/G_0/G_{90}]_s$	H4	2,61	1,870
$[C_{90}/G_0/G_{45}/G_{45}]_s$	H5	2,76	1,778
$[C_{90}/G_0/G_{45}/G_{-45}]_s$	H6	2,81	1,804
$[CW/\ G_0/\ G_{90}/G_{90}]_s$	K3	2,84	1,804
$[CW\ /\ G_0/\ G_{45}/\ G_{-45}]_s$	K4	2,90	1,805
$[CW\ /G_0/G_{45}/G_{45}]_s$	K5	2,90	1,772
$[G_{90}/G_0/C_0/C_{90}]_s$	K6	1,82	1,682
$[C_{90}/C_0/G_{90}/G_0]_{as}$	K7	1,95	1,613
$[GW/GW/CW/CW]_s$	W1	1,51	1,738
$[CW/CW/GW/GW]_s$	W2	1,52	1,727

G: Layer with glass fiber reinforcement material

C: Layer with carbon fiber reinforcement material

CW: Layer with carbon woven fabric consisting of twill weave

GW: Layer with glass woven fabric consisting of twill weave

Impact tests on the prepared specimens at temperatures of 20, 50, 90 and -50 °C were performed by using FRACTOVIS PLUS instrumented impact test machine. Before carrying out impact tests, some of G1, G2, G3, H4, H5, H6, K1, K2, K3, K4 and K5 samples were aged in glass cabin for 7 months under sea water immersion condition at 20°C temperature, as seen in Figure 4.1. The specimens were taken out of the cabin after 7 months and impact tests were performed at temperatures of 20 and -50 °C under the same energy levels with dry specimens.

Figure 4.1 The specimens were kept in sea water in glass cabin for 210 days.

The number of impact test specimens for each temperature and specimen type is given in Table 4.4, 4.5 and 4.6.

Table 4.4. The number of impact test specimens with six layers

Layup	Nomenclature	Test temperature: 20°C	Test temperature: 50 °C	Test temperature: 90 °C
		The Number of Specimens	The Number of Specimens	The Number of Specimens
$[0/0/90]_s$	C1	20	20	20
$[0/90/45]_s$	C2	20	20	20
$[90/0/0]_s$	C3	20	20	20

Table 4.5. The number of impact test specimens with eight layers

Layup	Nomenclature	Test temperature: 20°C	Test temperature: 90 °C	Test temperature: -50 °C
		The Number of Specimens	The Number of Specimens	The Number of Specimens
$[90/0/0/90]_s$	G1	20	24	24
$[90/0/45/45]_s$	G2	20	24	24
$[90/0/45/-45]_s$	G3	20	24	24
$[90/0/0/90]_s$	K1	14	14	14
$[90/0/45/45]_s$	K2	14	16	16
$[C_{90}/G_0/G_0/G_{90}]_s$	H4	14	14	14
$[C_{90}/G_0/G_{45}/G_{45}]_s$	H5	14	14	14
$[C_{90}/G_0/G_{45}/G_{-45}]_s$	H6	14	16	16
$[CW/\ G_0/\ G_{90}/G_{90}]_s$	K3	14	14	14
$[CW\ /\ G_0/\ G_{45}/\ G_{-45}]_s$	K4	14	14	14
$[CW\ /G_0/G_{45}/G_{45}]_s$	K5	14	14	14
$[G_{90}/G_0/C_0/C_{90}]_s$	K6	14	14	14
$[C_{90}/C_0/G_{90}/G_0]_{as}$	K7	14	14	14
$[GW/GW/CW/CW]_s$	W1	18	18	18
$[CW/CW/GW/GW]_s$	W2	18	18	18

Table 4.6 The number of the specimens kept in sea water for 7 months

		Test temperature: 20°C	Test temperature: -50 °C
Layup	**Nomenclature**	**The Number of Specimens**	**The Number of Specimens**
$[90/0/0/90]_s$	TS G1	9	9
$[90/0/45/45]_s$	TS G2	9	9
$[90/0/45/-45]_s$	TS G3	9	9
$[90/0/0/90]_s$	TS K1	9	9
$[90/0/45/45]_s$	TS K2	9	9
$[C_{90}/G_0/G_0/G_{90}]_s$	TS H4	9	9
$[C_{90}/G_0/G_{45}/G_{45}]_s$	TS H5	9	9
$[C_{90}/G_0/G_{45}/G_{-45}]_s$	TS H6	9	9
$[CW/\ G_0/\ G_{90}/G_{90}]_s$	TS K3	9	9
$[CW\ /\ G_0/\ G_{45}/\ G_{-45}]_s$	TS K4	9	9
$[CW\ /G_0/G_{45}/G_{45}]_s$	TS K5	9	9

4.2 Determination of Mechanical Properties at Room Temperature

Mechanical properties of a unidirectional glass/epoxy and carbon/epoxy composite plate at room temperature were determined to calculate thermal stresses occurring in the impact test specimens with during cooling from curing temperature. For this purpose, test specimens were prepared by cutting from the composite plate according to the ASTM standards. All the mechanical tests were performed by using INSTRON tensile test machine.

The coordinate system used to describe the properties is shown in Figure 4.2. The 1 direction is along the fibers, 2 direction is normal to the fibers in the laminate plane and 3 direction is through the laminate thickness.

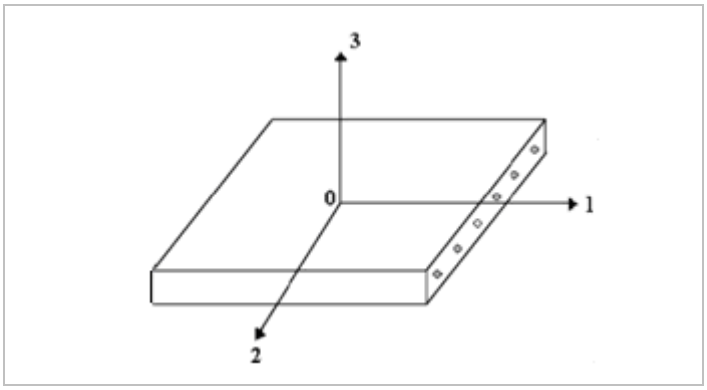

Figure 4.2 The coordinate system used for the composite laminates

Test samples were prepared according to the ASTM standards. All the mechanical tests were performed by using INSTRON tensile test machine. The load was applied to the samples at a constant cross-head speed of 1 mm/min. This test machine has a thermostatic chamber in which the temperature of the specimens can be adjusted. Each test was repeated with three specimens for the determination of each mechanical property and the mean values of test results were taken.

Longitudinal Young modulus E_1, poison's ratio υ_{12}, longitudinal tensile strengths X_t, transverse Young modulus E_2 and transverse tensile strengths Y_t were measured by using longitudinal and transverse $[0_8]$ unidirectional composite specimens according to the ASTM D3039-76 standard. The specimens were loaded up to the failure loads in the axial direction. A biaxial video extensometer was used to measure strains at 90 °C. At room temperature, strains were measured by means of strain gages stuck on the specimens in fiber and normal to fiber directions. Young moduli, E_1 and E_2 were calculated from the initial slope of the stress-strain curves. The tensile strengths of the unidirectional composite plates, X_t and Y_t, were determined by dividing the failure load to the cross-sectional area of the longitudinal and transverse specimens, respectively.

IITRI compression fixture was used to measure the compressive strength of the unidirectional glass/epoxy and carbon/epoxy laminated composites. The compression test specimens with 140 mm length were prepared according to ASTM D3410 standard. The width was taken as 6.4 and 12.7 mm for the longitudinal and transverse specimens, respectively. After the specimens were set into compression fixture by fastening screws in wedge clamps, the compressive loads were applied up to the occurrence of failure at a constant cross-head speed of 1 mm/min. The longitudinal and transverse compressive strengths, X_c and Y_c, are obtained by dividing the failure load to the cross-sectional area of the specimens.

The in-plane shear modulus and strength were measured by using Arcan test fixture as shown in Figure 4.3. For the tests, specimens with two 90° notches were

cut from [0_8] unidirectional glass/epoxy and carbon/epoxy laminated composites. Tensile force was applied to Arcan test fixture up to failure, so that a shear force transmitted through a section between two edge notches produces a nearly uniform shear stress along the section. The in-plane shear strength S_{12} was calculated by Equation (4.1).

$$S_{12} = \frac{P_{\max}}{wt} \tag{4.1}$$

Where P_{max} is the failure load, w is the width of the specimen at notch location and t is specimen thickness. Shear modulus G_{12} was measured by using two strain gage located at the center of the notched section at 45° and -45° to the loading direction. While tensile load was applied to the Arcan apparatus, force and stain values were read from the monitor and indicator, respectively. Shear strain γ_{12} is equal to the sum of the absolute values of normal strains, ε_{45} and ε_{-45}. Shear stress τ_{12} was obtained by using Eq. (4.1). The shear modulus was calculated using Equation (4.2).

$$G_{12} = \frac{\tau_{12}}{\gamma_{12}} \tag{4.2}$$

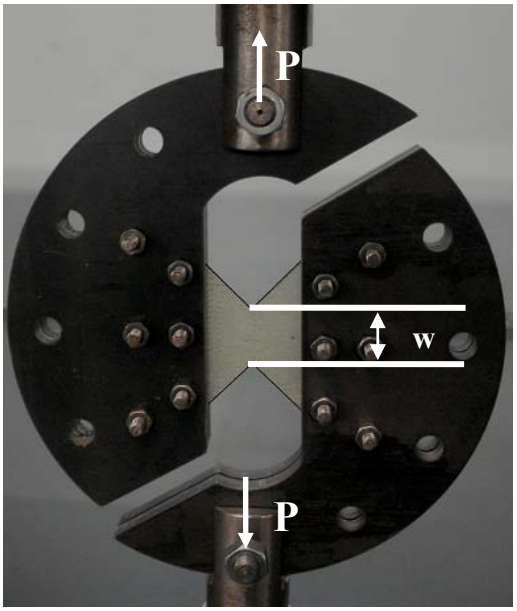

Figure 4.3 ARCAN test fixture

To determine the interlaminar shear strength, S_i, the double-notch shear test was performed as described in ASTM D3846-79. Specimens having dimensions of a 79.5 mm length, 12.7 mm width and 2.6 mm thickness were prepared from unidirectional reinforced composites. Two parallel notches were machined, one on each face of the specimen, 6.4 mm apart and with a depth equal to half the specimen thickness. While the axial tensile load was applied to the specimen, shear failure occurred along the midplane of the specimen between the notches. The interlaminar shear strength was determined using Equation (4.3).

$$S_i = \frac{P_{\max}}{wl} \tag{4.3}$$

where, P_{max} is the failure load, l is the distance between notches, and w the width of the specimen.

To determine the out-plane shear moduli G_{13} and G_{23}, specimens with 15 mm width, 50 mm length and 10 mm thickness were manufactured by using Standard Test Method for Short-Beam Strength as described in ASTM D2344/D2344M. The strain-gage was glued along the natural axis of longitudinal lateral surface of the specimen at angle of 45° with transverse direction as shown in Figures 4.4.a and 4.4.b (In plane 1-3 for G_{13}, in plane 2-3 for G_{23}). The specimen was placed on three-point bending test apparatus; while static forces were applied, strains were measured from indicator. Maximum shear stresses in natural axis were calculated as given in Equation (4.4). Shear strains are taken two times as normal strain (reading value) as given in Equation (4.5). G_{13} and G_{23} can be calculated by using Equation (4.6).

$$\tau_{13} = \frac{3P}{4A} \tag{4.4}$$

A: Cross-sectional area (width×thickness) [mm^2]

P: Static force [N]

$$\gamma_{13} = 2\varepsilon \tag{4.5}$$

$$G_{13} = \frac{\tau_{13}}{\gamma_{13}} \qquad \text{[MPa]} \qquad (4.6)$$

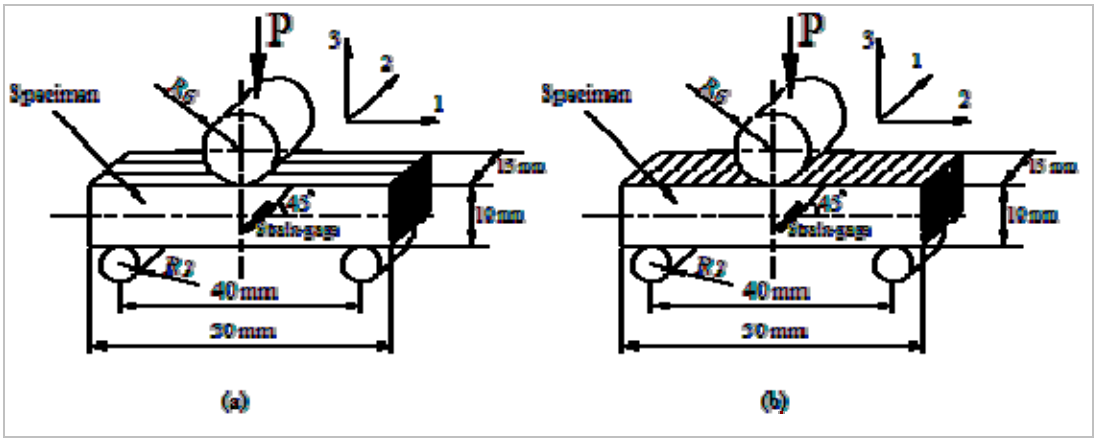

Figure 4.4 Schematic view of three-point bending test for G_{13} and G_{23}

The unidirectional laminated composites were placed into the thermal chamber in impact test machine. Then, thermal expansion coefficients of the composite materials were measured by reading strains in the fiber directions (ε_1) and strains in the transverse directions (ε_2) in indicator while increasing the temperature from 20 to -50 °C

Apart from the mechanical tests, by performing weight and volume measurements, fiber volume fractions and the densities of unidirectional glass/epoxy and carbon/epoxy composite plates were determined. All the results obtained from the mechanical tests are given in Table 4.7-4.9.

Table 4.7 Mechanical properties of Glass/Epoxy Composite Plate

Mechanical properties of Glass/Epoxy Composite Plate	**Magnitudes**
Fiber volume fraction (V_f)	59.2 %
Density, ρ (g/cm^3)	1.981
Longitudinal modulus, E_1 (GPa)	47.9
Transverse modulus, E_2 (GPa)	20.3
In-plane shear modulus, G_{12} (GPa)	4.9
Poisson's ratio (ν_{12})	0.25
Longitudinal tensile strength, X_t (MPa)	979.2
Transverse tensile strength, Y_t (MPa)	65.0
Longitudinal compressive strength, X_c (MPa)	473.4
Transverse compressive strength, Y_c (MPa)	171.6
Longitudinal thermal expansion coefficient α_1 [1/ºC×10^{-6}]	3.32
Transverse thermal expansion coefficient α_2 [1/ºC×10^{-6}]	17.40

Table 4.8 Mechanical properties of Carbon/Epoxy Composite Plate

Mechanical properties of Carbon/Epoxy Composite Plate	**Magnitudes**
Fiber volume fraction (V_f)	61.3 %
Density, ρ (g/cm^3)	1.71
Longitudinal modulus, E_1 (GPa)	150.9
Transverse modulus, E_2 (GPa)	11.25
In-plane shear modulus, G_{12} (GPa)	5.34
Poisson's ratio (ν_{12})	0.29
Longitudinal tensile strength, X_t (MPa)	1858.3
Transverse tensile strength, Y_t (MPa)	25.45
Longitudinal compressive strength, X_c (MPa)	576.8
Transverse compressive strength, Y_c (MPa)	107.3
Longitudinal thermal expansion coefficient α_1 [1/ºC×10^{-6}]	-3.31
Transverse thermal expansion coefficient α_2 [1/ºC×10^{-6}]	11.67

Table 4.9 Shear modulus and strength of glass/epoxy and carbon/epoxy composites

Mechanical Properties	**Glass/Epoxy Composite**	**Carbon/Epoxy Composite**
In-plane shear modulus (G_{12}) [GPa]	4.3	5.3
Transverse shear modulus (G_{13}) [GPa]	4.2	5.2
Inter laminar Shear Strength (S_{13}) [MPa]	32.3	22.9
In-plane shear strength (S_{12}) [MPa]	69.8	48.5

4.3 Determination of Mechanical Properties at High Temperature

Mechanical properties of carbon/epoxy and glass/Epoxy Laminated Composite plates were found at high temperature of 90 °C by carrying out the same tests with that under room temperature. Standard specimens were prepared in fiber and normal to fiber directions. The tests were carried out in INSTRON test machine founded at Pamukkale University (Figure 4.5). Test results are given in Table 4.10 and 4.11, along with the results of tests performed at room temperature.

Figure 4.5 INSTRON test machine

Table 4.10 Mechanical properties of glass/epoxy composite plate at 90 °C

Mechanical Properties of Glass/Epoxy Composite Plate	**Room Temperature**	**90 °C Temperature**
Longitudinal modulus, E_1 (GPa)	47.9	36.5
Transverse modulus, E_2 (GPa)	20.3	9.57
Longitudinal tensile strength, X_t (MPa)	979.2	893.4
Transverse tensile strength, Y_t (MPa)	65.0	37.6
Inter laminar Shear Strength [MPa]	32.3	15.7

Table 4.11 Mechanical properties of carbon/epoxy composite plate at 90 °C

Mechanical Properties of Carbon/Epoxy Composite Plate	**Room Temperature**	**90 °C Temperature**
Longitudinal modulus, E_1 (GPa)	150.9	119.6
Transverse modulus, E_2 (GPa)	11.25	9.2
Longitudinal tensile strength, X_t (MPa)	1858.3	1323.4
Transverse tensile strength, Y_t (MPa)	25.45	25.7
Inter laminar Shear Strength S_{13} [MPa]	22.9	14.2

The mechanical test results show that when the temperature is increased from 20 °C to 90 °C, mechanical properties of the unidirectional glass/epoxy and carbon/epoxy composite plates are significantly reduced.

In impact phenomenon, longitudinal and transverse moduli have significant effects on indentation and deflection. While longitudinal and transverse tensile strengths specify impact damage resistance of lower layers in composite plates, longitudinal and transverse compressive strengths specify that of upper layers. Interlaminar shear strength plays an important role in delamination and debonding resistance. Also, thermal residual stresses occurring during and after manufacturing may influence impact resistance of the plates.

CHAPTER FIVE
THERMAL RESIDUAL STRESS ANALYSIS OF THE LAMİNATED PLATES

5.1 Introduction

In unidirectional glass/epoxy reinforced composite plates, the thermal expansion coefficient in the direction of fibers α_1 is normally much smaller than that in the transverse direction α_2. In addition, longitudinal modulus E_1 is much greater than transverse modulus, E_2. As the specimens are cooled from cure temperature, each layer tends to contract in the transverse direction much more than in the fiber direction. However, this transverse contraction is constrained by the adjacent layer, and this produces in-plane thermal residual stresses in the laminate. These stresses may be great enough to cause interfacial debonding in the composite and nano-cracks within the matrix during cool-down (Gomez, Zaera, Barbero, & Navarro, 2005). Moreover, the thermal residual stresses may influence the impact behavior and impact induced damage modes of unidirectional glass/epoxy reinforced composite plates. Therefore, it is significant to determine the thermal residual stresses occurring in the laminates at impact test temperatures of 20, 90 and -50 °C.

Thermal stress analyses of all the composite laminates which were produced for impact tests were performed by using ANSYS software. To this end, finite element models of the impact test specimens having the different thicknesses and stacking sequences were formed in ANSYS software, as shown in Figure 5.1. SOLID46 element given in Figure 5.2 was selected for meshing. SOLID46 is a layered version of the 8-node structural solid (SOLID45) designed to model layered thick shells or solids. The element has three degrees of freedom at each node: translations in the nodal x, y, and z directions.

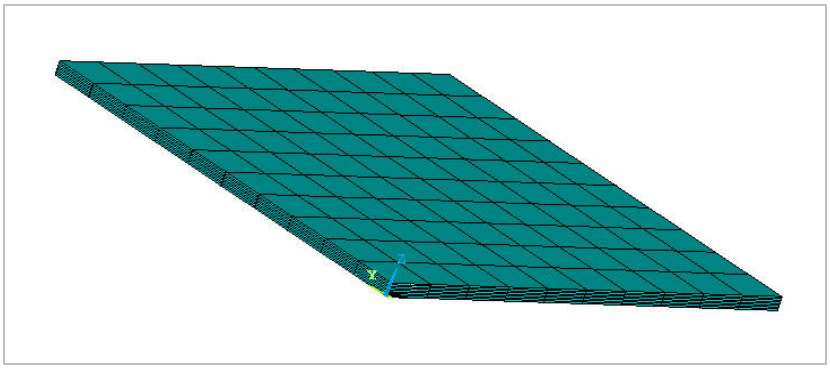

Figure 5.1 Finite element models of square specimens

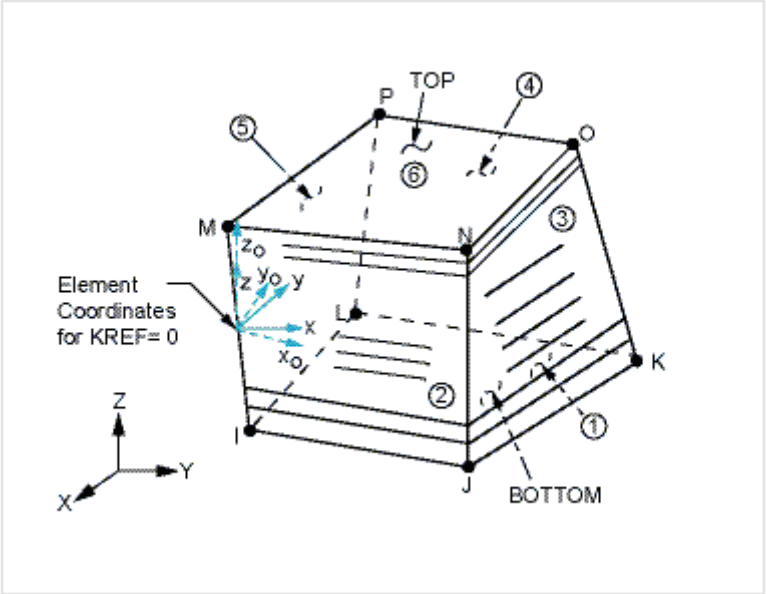

Figure 5.2 SOLID46 element

During modeling, the elements are considered to consist of 6 and 8 layers each of which is oriented with respect to the mentioned fiber angles. Mechanical properties of the plates were entered into the program by using properties of $[0°]_8$ oriented glass/epoxy composite plate given in Table 4.7-4.9. Variation of the mechanical properties with temperature was not included into the model to simply the computation. Curing temperature 120 °C at which the laminate is stress-free was taken as initial temperature. Considering impact test conditions of composite plates, final temperatures were applied onto the model as 20, 90, -50 °C. Boundary conditions were not applied to the edges of the model since the composite plates were not subjected to in-plane loading and constrains during and after fabrication. In solution processing, classical plate theory given in Section 5.2 was used.

5.2 Classical Lamination Theory

Classical lamination theory consists of a collection of mechanics of materials type of stress and deformation hypotheses. By use of this theory, we can consistently proceed directly from the basic building block, the lamina, to the end result, a structure laminate. The whole process is one of finding effective and reasonably accurate simplifying assumptions that enable us to reduce our attention from a complicated three-dimensional elasticity problem to a solvable two-dimensional mechanics of deformable body problem. (Jones, 1999)

5.2.1 Lamina Stress-Strain Behavior

The stress-strain relations in principal material coordinates for a lamina of an orthotropic material under plane stress are

$$\begin{bmatrix} \sigma_1 \\ \sigma_2 \\ \sigma_{12} \end{bmatrix} = \begin{bmatrix} Q_{11} & Q_{12} & 0 \\ Q_{12} & Q_{22} & 0 \\ 0 & 0 & Q_{66} \end{bmatrix} \begin{bmatrix} \varepsilon_1 \\ \varepsilon_2 \\ \gamma_{12} \end{bmatrix} \tag{5.1}$$

In any other coordinate system in the plane of the lamina, the stresses are

$$\begin{bmatrix} \sigma_x \\ \sigma_y \\ \sigma_{xy} \end{bmatrix} = \begin{bmatrix} \overline{Q_{11}} & \overline{Q_{12}} & \overline{Q_{16}} \\ \overline{Q_{12}} & \overline{Q_{22}} & \overline{Q_{26}} \\ \overline{Q_{16}} & \overline{Q_{26}} & \overline{Q_{66}} \end{bmatrix} \begin{bmatrix} \varepsilon_x \\ \varepsilon_y \\ \gamma_{xy} \end{bmatrix} \tag{5.2}$$

Both the Equations (5.1) and (5.2) can be thought of as stress-strain relations for the k^{th} layer of a multilayered laminate. Thus, Equation (5.2) can be written as

$$\{\sigma\}_k = \left[\overline{Q}\right]_k . \{\varepsilon\}_k \tag{5.3}$$

By substitution of strain variation through the thicknesses in the stress-strain relations, the stress in the k[th] layer can be expresses in terms of the laminate middle surface strains and curvatures as

$$\begin{bmatrix}\sigma_x\\ \sigma_y\\ \sigma_{xy}\end{bmatrix}=\begin{bmatrix}\overline{Q_{11}} & \overline{Q_{12}} & \overline{Q_{16}}\\ \overline{Q_{12}} & \overline{Q_{22}} & \overline{Q_{26}}\\ \overline{Q_{16}} & \overline{Q_{26}} & \overline{Q_{66}}\end{bmatrix}\left[\begin{bmatrix}\varepsilon_x^0\\ \varepsilon_y^0\\ \gamma_{xy}^0\end{bmatrix}+z\begin{bmatrix}K_x\\ K_y\\ K_{xy}\end{bmatrix}\right] \tag{5.4}$$

5.2.2 Resultant Laminate Forces and Moments

The resultant forces and moments acting on a laminate are obtained by integration of the stresses in each layer or lamina through the laminate thickness, for example,

$$N_x=\int_{-t/2}^{t/2}\sigma_x dz \qquad\qquad M_z=\int_{-t/2}^{t/2}\sigma_x z dz \tag{5.5}$$

When the lamina stress-strain relations, Equation (5.4), substituted, the forces and moments become

$$\begin{bmatrix}N_x\\ N_y\\ N_{xy}\end{bmatrix}=\sum_{\mathrm{k=1}}^{\mathrm{N}}\begin{bmatrix}\overline{Q_{11}} & \overline{Q_{12}} & \overline{Q_{16}}\\ \overline{Q_{12}} & \overline{Q_{22}} & \overline{Q_{26}}\\ \overline{Q_{16}} & \overline{Q_{26}} & \overline{Q_{66}}\end{bmatrix}_k=\begin{bmatrix}\int_{z_{k-1}}^{z_k}\begin{bmatrix}\varepsilon_x^0\\ \varepsilon_y^0\\ \gamma_{xy}^0\end{bmatrix}dz+\int_{z_{k-1}}^{z_k}\begin{bmatrix}K_x\\ K_y\\ K_{xy}\end{bmatrix}z dz\end{bmatrix} \tag{5.6}$$

$$\begin{bmatrix}M_x\\ M_y\\ M_{xy}\end{bmatrix}=\sum_{\mathrm{k=1}}^{\mathrm{N}}\begin{bmatrix}\overline{Q_{11}} & \overline{Q_{12}} & \overline{Q_{16}}\\ \overline{Q_{12}} & \overline{Q_{22}} & \overline{Q_{26}}\\ \overline{Q_{16}} & \overline{Q_{26}} & \overline{Q_{66}}\end{bmatrix}_k=\begin{bmatrix}\int_{z_{k-1}}^{z_k}\begin{bmatrix}\varepsilon_x^0\\ \varepsilon_y^0\\ \gamma_{xy}^0\end{bmatrix}z dz+\int_{z_{k-1}}^{z_k}\begin{bmatrix}K_x\\ K_y\\ K_{xy}\end{bmatrix}z^2 dz\end{bmatrix} \tag{5.7}$$

As known, $\varepsilon_x^o, \varepsilon_y^0, \gamma_{xy}^0, \kappa_x, \kappa_y$, and κ_{xy} are not functions of z, but are middle-surface values so they can be removed from within the summation sings. Thus, it can be written as:

$$\begin{bmatrix} N_x \\ N_y \\ N_{xy} \end{bmatrix} = \begin{bmatrix} A_{11} & A_{12} & A_{16} \\ A_{12} & A_{22} & A_{26} \\ A_{16} & A_{26} & A_{66} \end{bmatrix} \begin{bmatrix} \varepsilon_x^0 \\ \varepsilon_y^0 \\ \gamma_{xy}^0 \end{bmatrix} + \begin{bmatrix} B_{11} & B_{12} & B_{16} \\ B_{12} & B_{22} & B_{26} \\ B_{16} & B_{26} & B_{66} \end{bmatrix} \begin{bmatrix} K_x \\ K_y \\ K_{xy} \end{bmatrix} \tag{5.8}$$

$$\begin{bmatrix} M_x \\ M_y \\ M_{xy} \end{bmatrix} = \begin{bmatrix} B_{11} & B_{12} & B_{16} \\ B_{12} & B_{22} & B_{26} \\ B_{16} & B_{26} & B_{66} \end{bmatrix} \begin{bmatrix} \varepsilon_x^0 \\ \varepsilon_y^0 \\ \gamma_{xy}^0 \end{bmatrix} + \begin{bmatrix} D_{11} & D_{12} & D_{16} \\ D_{12} & D_{22} & D_{26} \\ D_{16} & D_{26} & D_{66} \end{bmatrix} \begin{bmatrix} K_x \\ K_y \\ K_{xy} \end{bmatrix} \tag{5.9}$$

where

$$B_{ij} = \frac{1}{2}\sum_{k=1}^{N} (\overline{Q_{ij}})_k (z_k^2 - z_{k-1}^2) \tag{5.10}$$

$$A_{ij} = \sum_{k=1}^{N} (\overline{Q_{ij}})_k (z_k - z_{k-1}) \tag{5.11}$$

$$D_{ij} = \frac{1}{3}\sum_{k=1}^{N} (\overline{Q_{ij}})_k (z_k^3 - z_{k-1}^3) \tag{5.12}$$

5.2.3 Thermal and Mechanical Stress Analysis

Mechanical stress analysis does not suffice for analysis of laminates that have been cured at temperatures different from the design operating temperature. In such cases, thermal stresses arise and must be accounted for. The there-dimentional thermoelastic anisotropic strain-stress relation is:

$$\sigma_j = C_{ij}(\varepsilon_j - \alpha_j \Delta T) \qquad i, j = 1,2,...,6 \tag{5.13}$$

For plane stress on an orthotropic lamina in principal material coordinates,

$$\begin{bmatrix} \sigma_1 \\ \sigma_2 \\ \sigma_{12} \end{bmatrix} = \begin{bmatrix} Q_{11} & Q_{12} & 0 \\ Q_{12} & Q_{22} & 0 \\ 0 & 0 & Q_{66} \end{bmatrix} \begin{bmatrix} \varepsilon_1 - \alpha_1 \Delta T \\ \varepsilon_2 - \alpha_2 \Delta T \\ \gamma_{12} \end{bmatrix} \tag{5.14}$$

The stresses in laminate coordinates for the k[th] layer are obtained by transformation of coordinates

$$\begin{bmatrix} \sigma_x \\ \sigma_y \\ \sigma_{xy} \end{bmatrix}_k = \begin{bmatrix} \overline{Q_{11}} & \overline{Q_{12}} & \overline{Q_{16}} \\ \overline{Q_{12}} & \overline{Q_{22}} & \overline{Q_{26}} \\ \overline{Q_{16}} & \overline{Q_{26}} & \overline{Q_{66}} \end{bmatrix} \begin{bmatrix} \varepsilon_x - \alpha_x \Delta T \\ \varepsilon_y - \alpha_y \Delta T \\ \gamma_{xy} - \alpha_{xy} \Delta T \end{bmatrix}_k \tag{5.15}$$

When the linear variation of strain through the thickness is substituted in Equation (5.15) and the resulting expressions for the layer stresses are integrated through the thickness, the force resultants are

$$\begin{bmatrix} N_x \\ N_y \\ N_{xy} \end{bmatrix} = \begin{bmatrix} A_{11} & A_{12} & A_{16} \\ A_{12} & A_{22} & A_{26} \\ A_{16} & A_{26} & A_{66} \end{bmatrix} \begin{bmatrix} \varepsilon_x^0 \\ \varepsilon_y^0 \\ \gamma_{xy}^0 \end{bmatrix} + \begin{bmatrix} B_{11} & B_{12} & B_{16} \\ B_{12} & B_{22} & B_{26} \\ B_{16} & B_{26} & B_{66} \end{bmatrix} \begin{bmatrix} K_x \\ K_y \\ K_{xy} \end{bmatrix} - \begin{bmatrix} N_x^T \\ N_y^T \\ N_{xy}^T \end{bmatrix} \tag{5.16}$$

The thermal forces are:

$$\begin{bmatrix} N_x^T \\ N_y^T \\ N_{xy}^T \end{bmatrix} = \int \begin{bmatrix} \overline{Q_{11}} & \overline{Q_{12}} & \overline{Q_{16}} \\ \overline{Q_{12}} & \overline{Q_{22}} & \overline{Q_{26}} \\ \overline{Q_{16}} & \overline{Q_{26}} & \overline{Q_{66}} \end{bmatrix}_k \begin{bmatrix} \alpha_x \\ \alpha_y \\ \alpha_{xy} \end{bmatrix}_k \Delta T dz \tag{5.17}$$

In a similar manner, the moment resultants are obtained by integrating the moment of the stresses through the thickness:

$$\begin{bmatrix} M_x \\ M_y \\ M_{xy} \end{bmatrix} = \begin{bmatrix} B_{11} & B_{12} & B_{16} \\ B_{12} & B_{22} & B_{26} \\ B_{16} & B_{26} & B_{66} \end{bmatrix} \begin{bmatrix} \varepsilon_x^0 \\ \varepsilon_y^0 \\ \gamma_{xy}^0 \end{bmatrix} + \begin{bmatrix} D_{11} & D_{12} & D_{16} \\ D_{12} & D_{22} & D_{26} \\ D_{16} & D_{26} & D_{66} \end{bmatrix} \begin{bmatrix} K_x \\ K_y \\ K_{xy} \end{bmatrix} - \begin{bmatrix} M_x^T \\ M_y^T \\ M_{xy}^T \end{bmatrix} \tag{5.18}$$

The thermal moments are

$$\begin{bmatrix} M_x^T \\ M_y^T \\ M_{xy}^T \end{bmatrix} = \int \begin{bmatrix} \overline{Q_{11}} & \overline{Q_{12}} & \overline{Q_{16}} \\ \overline{Q_{12}} & \overline{Q_{22}} & \overline{Q_{26}} \\ \overline{Q_{16}} & \overline{Q_{26}} & \overline{Q_{66}} \end{bmatrix}_k \begin{bmatrix} \alpha_x \\ \alpha_y \\ \alpha_{xy} \end{bmatrix}_k \Delta T z dz \tag{5.19}$$

The force and moment resultants can be rearranged to read

$$\begin{bmatrix} \overline{N_x} \\ \overline{N_y} \\ \overline{N_{xy}} \end{bmatrix} \begin{bmatrix} N_x + N_x^T \\ N_y + N_y^T \\ N_{xy} + N_{xy}^T \end{bmatrix} = \begin{bmatrix} A_{11} & A_{12} & A_{16} \\ A_{12} & A_{22} & A_{26} \\ A_{16} & A_{26} & A_{66} \end{bmatrix} \begin{bmatrix} \varepsilon_x^0 \\ \varepsilon_y^0 \\ \gamma_{xy}^0 \end{bmatrix} + \begin{bmatrix} B_{11} & B_{12} & B_{16} \\ B_{12} & B_{22} & B_{26} \\ B_{16} & B_{26} & B_{66} \end{bmatrix} \begin{bmatrix} K_x \\ K_y \\ K_{xy} \end{bmatrix} \tag{5.20}$$

$$\begin{bmatrix} \overline{M_x} \\ \overline{M_y} \\ \overline{M_{xy}} \end{bmatrix} = \begin{bmatrix} M_x + M_x^T \\ M_y + M_y^T \\ M_{xy} + M_{xy}^T \end{bmatrix} = \begin{bmatrix} B_{11} & B_{12} & B_{16} \\ B_{12} & B_{22} & B_{26} \\ B_{16} & B_{26} & B_{66} \end{bmatrix} \begin{bmatrix} \varepsilon_x^0 \\ \varepsilon_y^0 \\ \gamma_{xy}^0 \end{bmatrix} + \begin{bmatrix} D_{11} & D_{12} & D_{16} \\ D_{12} & D_{22} & D_{26} \\ D_{16} & D_{26} & D_{66} \end{bmatrix} \begin{bmatrix} K_x \\ K_y \\ K_{xy} \end{bmatrix} \tag{5.21}$$

In the form of Equations (5.20) and (5.21), the thermal portion of thermal and mechanical stress problems can be treated as equivalent mechanical loads defined by N^T and M^T in Equations (5.17) and (5.19), respectively, in addition to the mechanical loads, N and M.

5.3. Results of Thermal Stress Analysis

5.3.1 Thermal Stress Analysis of Glass/Epoxy Laminated Composites with Six Layers

Square specimens of 100×100 mm^2 having 1.8 mm thickness were modeled in ANSYS software. SOLID46 element was selected for meshing. The elements are considered to consist of 6 layers each of which has 0,3 mm thickness and oriented with respect to mentioned fiber angles. Mechanical properties of the plates were entered into the program by using properties of the unidirectional glass/epoxy

composites given in Table 4.7. Initial temperature at which curing starts was taken as 120 °C. Considering impact test conditions of composite plates, final temperatures were applied onto the model as 20, 50, 90 °C. Boundary conditions were not applied to the edges of the model since the composite plates were not subjected to in-plane loading and constrains during and after fabrication. After the finite element models of the composite plates were completed, thermal stress analyses were performed.

Due to temperature difference and since the laminates have different thermal expansion coefficient in fiber and normal to fiber directions, thermal stresses occur in each ply. Distributions of σ_x and σ_y residual thermal stresses through the thickness are given in Figure 5.3. It is seen from the graphs that thermal stress distributions are dependent on fiber orientations and layer sequences. Because layer sequences of the composite plates are symmetric, stress distribution for each layer is constant throughout the thickness. If adjacent layers have the same orientations, the stress distributions are the same within the layers. For instance, the composite plate with lay-up $[0/0/90]_s$ has the same stress distributions for 1-2 and 5-6 layers.

When variations of the residual stresses versus temperatures of 20, 50 and 90 °C are investigated, it can be noticed that σ_x and σ_y thermal residual stresses decrease with increasing temperature since ambient (final) temperature is getting closer to the curing (initial) temperature. The thermal residual stresses at 50 and 90 °C are approximately 26% and % 66 lower, respectively, for all orientations in comparison with that at 20 °C. In addition, interlaminar shear stresses, which occur between adjacent layers with different orientations and satisfy static equilibrium of thermal residual stresses decrease with increasing final temperature. Therefore, contribution of temperature to impact induced delamination and damage areas are expected to decrease in the composite plates when plates are impacted at high temperatures. Matrix cracking damage parameters obtained for the laminates, which will be explained in the next section, are given in Table 5.1

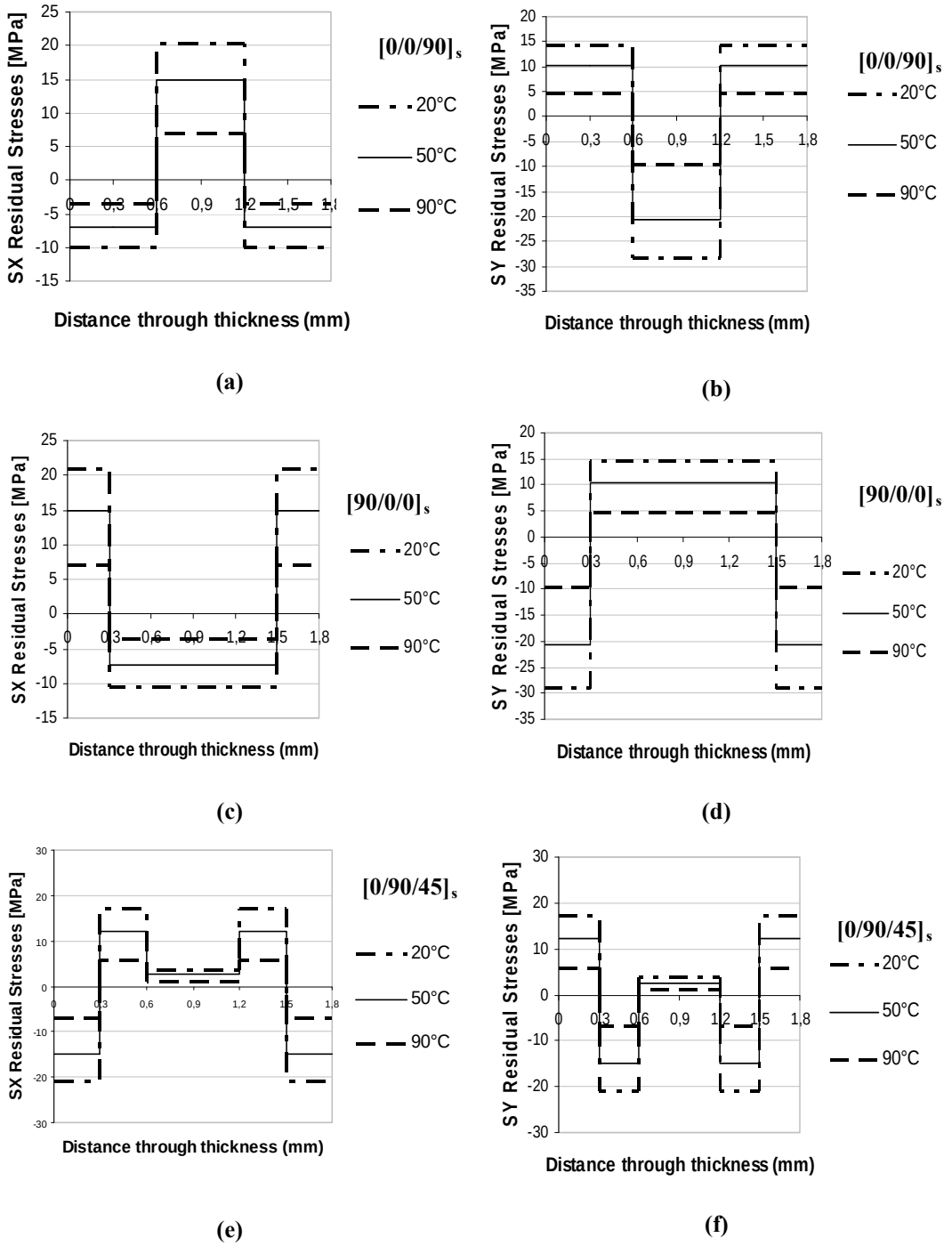

Figure 5.3 Distributions of σ_x and σ_y residual thermal stresses through thickness

Table 5.1 Matrix Cracking Damage Parameter due to thermal residual stresses

Lay up	**Matrix Cracking Factor, e_m^2**			
Temperature	**90 °C**	**50 °C**	**20 °C**	**-50 °C**
$[0/0/90]_s$	0.015	0.053	0.104	0.289
$[90/0/0]_s$	0.015	0.053	0.104	0.289
$[0/90/45]_s$	0.0085	0.034	0.068	0.185

5.3.2 Thermal Stress Analysis of the Laminated Composites with Eight Layers

Maximum and minimum stress components were obtained from the results of thermal stress analyses. Stress components of σ_1 and σ_2 are compressive and tensile stresses occurring in fiber and transverse directions, respectively. The results show that σ_1 and σ_2 have the same value in all the plies expect for G2 laminate with a lay-up $[90/0/45/45]_s$. In addition, stress components of $\sigma_3, \tau_{12}, \tau_{13}$ and τ_{23} have negligible values. Thermal residual stresses occurring at 20, 90 and -50 °C temperatures are given for all the laminates in Table 5.2.

Table 5.2 Thermal residual stresses occurring at 20, 90 and -50 °C temperatures

Layer	Stress Component [MPa]	Nomenclature and Temperature (°C)								
		G1 90	G1 20	G1 -50	G2 90	G2 20	G2 -50	G3 90	G3 20	G3 -50
1	σ_2	5.24	17.47	29.71	4.75	15.82	26.89	5.24	17.47	29.71
	σ_1	-5.24	-17.47	-29.71	-6.78	-22.61	-38.44	-5.24	-17.47	-29.71
2	σ_2	5.24	17.47	29.71	4.75	15.82	26.89	5.24	17.47	29.71
	σ_1	-5.24	-17.47	-29.71	-6.78	-22.61	-38.44	-5.24	-17.47	-29.71
3	σ_2	5.24	17.47	29.71	2.40	5.01	13.61	5.24	17.47	29.71
	σ_1	-5.24	-17.47	-29.71	-0.37	-1.22	-2.07	-5.24	-17.47	-29.71
4	σ_2	5.24	17.47	29.71	2.40	5.01	13.61	5.24	17.47	29.71
	σ_1	-5.24	-17.47	-29.71	-0.37	-1.22	-2.07	-5.24	-17.47	-29.71
5	σ_2	5.24	17.47	29.71	2.40	5.01	13.61	5.24	17.47	29.71
	σ_1	-5.24	-17.47	-29.71	-0.37	-1.22	-2.07	-5.24	-17.47	-29.71
6	σ_2	5.24	17.47	29.71	2.40	5.01	13.61	5.24	17.47	29.71
	σ_1	-5.24	-17.47	-29.71	-0.37	-1.22	-2.07	-5.24	-17.47	-29.71
7	σ_2	5.24	17.47	29.71	4.75	15.82	26.89	5.24	17.47	29.71
	σ_1	-5.24	-17.47	-29.71	-6.78	-22.61	-38.44	-5.24	-17.47	-29.71
8	σ_2	5.24	17.47	29.71	4.75	15.82	26.89	5.24	17.47	29.71
	σ_1	-5.24	-17.47	-29.71	-6.78	-22.61	-38.44	-5.24	-17.47	-29.71

When variations of the residual stresses versus temperatures of 90, 20 and -50 °C are investigated, it is noticed that σ_1 and σ_2 thermal residual stresses decrease with increasing temperature since ambient (final) temperature is getting closer to the

curing (initial) temperature. Some of these values could be high enough to have influence on the onset of damage during impact. Therefore, the effect was analyzed using damage parameters proposed by Hou, Petrinic, Ruiz, & Hallet (2000) based on the Chang–Chang failure criteria (Chang & Chang, 1987). These criteria consist of four damage parameters given in Equation (5.22), (5.23), (5.24) and (5.25).

Fiber Failure:

$$e_f^2 = \left(\frac{\sigma_1}{X_T}\right)^2 + \left(\frac{\tau_{12} + \tau_{23}}{S_f}\right)^2 \geq 1 \tag{5.22}$$

Transverse matrix cracking ($\sigma_2 > 0$):

$$e_m^2 = \left(\frac{\sigma_2}{Y_T}\right)^2 + \left(\frac{\tau_{12}}{S_{12}}\right)^2 + \left(\frac{\tau_{23}}{S_{m23}}\right)^2 \geq 1 \tag{5.23}$$

Matrix crushing ($\sigma_2 \leq 0$):

$$e_d^2 = \frac{1}{4}\left(\frac{\sigma_2}{S_{12}}\right)^2 + \frac{Y_C \sigma_2}{4S_{12}^2} - \frac{\sigma_2}{Y_C} + \left(\frac{\tau_{12}}{S_{12}}\right)^2 \geq 1 \tag{5.24}$$

Delamination:

$$e_l^2 = \left(\frac{\sigma_3}{Z_T}\right)^2 + \left(\frac{\tau_{13}}{S_{13}}\right)^2 + \left(\frac{\tau_{23}}{S_{l23}}\right)^2 \geq 1 \tag{5.25}$$

Each failure type take places when the associated damage parameter equals 1. Where S_f is shear strength involving fiber failure, S_{m23} is shear strength for matrix cracking in the transverse and through-thickness plane, S_{l23} is shear strength for delamination in the transverse and through-thickness plane and Z_T tensile strength in the through-thickness direction. The mechanical tests required for determining these properties were not performed because their contributions to damage parameters are negligible. For example, since stress components of τ_{12}, and τ_{23} in Equation (5.22) are close to zero, value of $\left(\frac{\tau_{12} + \tau_{23}}{S_f}\right)^2$ is negligible and fiber failure factor, e_f^2 can be

taken equal to $\left(\frac{\sigma_1}{X_t}\right)^2$. Therefore, determination of S_f was not required. While the value of each damage parameter was calculated, only X_T, Y_T and Y_C were used since stress components of $\sigma_3, \tau_{12}, \tau_{13}$ and τ_{23} are close to zero. In addition, as σ_2 have positive values, transverse matrix cracking parameter was used for calculation of matrix failure criteria. The results obtained from the analysis reveal that while values of delamination and fiber failure parameters are negligible, transverse matrix cracking damage parameters have high values especially before impact at -50 °C temperature. Therefore, only values of the matrix cracking parameter e_m^2 were presented in Table 5.3. The magnitude of this parameter is the same for each ply of G1 and G3 laminates while that is different for each ply of G2 laminate. It is seen from the table that the type of the damage parameter e_m^2 approaches critical value while the temperature is decreasing from 90 to -50 °C. For example, the magnitude of this parameter for G1 and G3 laminates at 90 °C is 0.005 but, at -50 °C it rises to around 0.168.

Table 5.3 Matrix Cracking Damage Parameter due to thermal residual stresses

Matrix Cracking Factor	**Nomenclature and Temperature (°C)**								
	G1 90	**G1 20**	**G1 -50**	**G2 90**	**G2 20**	**G2 -50**	**G3 90**	**G3 20**	**G3 -50**
e_m^2	0.005	0.058	0.168	0.009	0.097	0.281	0.005	0.058	0.168

Matrix cracks caused by impact on composite laminates do not significant contribute to the reduction in residual properties of the laminate. However, the damage process is initiated by matrix cracks which then induce delaminations at ply interfaces (Abrate, 1998). Therefore, when impacted at low temperature, greater damage extension is expected to be taken place in the composite laminates because of higher values of the matrix cracking parameter e_m^2. In addition, the high value has influence on impact parameters such as initial, perforation and dissipation energy. To investigate the effects, impact tests on the composite laminates were carried out at 20, 90 and -50 °C.

Table 5.4 σ_2 Thermal residual stresses occurring in matrix direction at each ply of samples at -50 °C

Specimen Type	G1	G2	G3	H4	H5	H6
1. Layer	29.7	26.8	29.7	2.44	-1.045	0.37
	29.7	26.8	29.7	2.44	-1.045	0.37
2. Layer	29.7	26.8	29.7	52.91	52.91	54.38
	29.7	26.8	29.7	52.91	52.91	54.38
3. Layer	29.7	13.6	29.7	52.91	35.59	44.95
	29.7	13.6	29.7	52.91	35.59	44.95
4. Layer	29.7	13.6	29.7	37.61	35.59	44.95
	29.7	13.6	29.7	37.61	35.59	44.95
5. Layer	29.7	13.6	29.7	37.61	35.59	44.95
	29.7	13.6	29.7	37.61	35.59	44.95
6. Layer	29.7	13.6	29.7	52.91	35.59	44.95
	29.7	13.6	29.7	52.91	35.59	44.95
7. Layer	29.7	26.8	29.7	52.91	52.91	54.38
	29.7	26.8	29.7	52.91	52.91	54.38
8. Layer	29.7	26.8	29.7	2.44	-1.045	0.37
	29.7	26.8	29.7	2.44	-1.045	0.37

Specimen Type	K3	K4	K5	K6	K7	K1	K2
1. Layer	-31.27	-31.28	-31.56	37.61	23.33	25.63	23.25
	-31.27	-31.28	-31.56	37.61	21.42	25.63	23.25
2. Layer	65.38	63.33	63.01	52.91	23.13	25.63	23.25
	65.38	63.33	63.01	52.91	20.22	25.63	23.25
3. Layer	65.38	64.48	58.98	52.91	66.28	25.63	19.66
	65.38	64.48	58.98	52.91	63.33	25.63	19.66
4. Layer	65.38	64.48	58.98	2.44	62.72	25.63	19.66
	65.38	64.48	58.98	2.44	57.74	25.63	19.66
5. Layer	65.38	64.48	58.98	2.44	15.7	25.63	19.66
	65.38	64.48	58.98	2.44	13.8	25.63	19.66
6. Layer	65.38	64.48	58.98	52.91	11.49	25.63	19.66
	65.38	64.48	58.98	52.91	8.58	25.63	19.66
7. Layer	65.38	63.33	63.01	52.91	54.48	25.63	23.25
	65.38	63.33	63.01	52.91	51.53	25.63	23.25
8. Layer	-31.27	-31.28	-31.56	37.61	42.81	25.63	23.25
	-31.27	-31.28	-31.56	37.61	37.83	25.63	23.25

Maximum stresses occurring at each ply of the impact test samples at -50 °C temperature are given in Table 5.4. It is seen from the table that the tensile thermal residual stresses are high enough to induce matrix cracks. Therefore, delamination and matrix cracks at -50 °C temperature begin at lower impact energies than that at room temperature. Compressive stresses in fiber direction occur, which have same values with tensile stresses occurring in matrix direction. Since more tensile fiber cracks take place in specimens subjected to high impact energy, compressive thermal stresses may decrease the effects of tensile stresses occurring in fiber direction under

impact loading. Results of thermal stress analysis reveal that the decrease ranges from 2% to 5% approximately, dependent on specimen type

The matrix cracking parameters of the laminates at -50 °C are given in Table 5.5. It is shown from the table that the value of matrix cracking parameters for K3, K7 and K1 exceeds critical value, 1. Therefore, it is possible that matrix cracks could begin for the laminates before impact tests are performed. The values of this parameter for glass/carbon hybrid (H4, H5, H6, K3, K4, K5, K6, K7 laminates) and carbon/epoxy composites (K1, K2 laminates) are higher in comparison with glass/epoxy composite plates (G1, G2 and G3 laminates). This is because carbon fibers are expanded during cooling, while glass fibers are contracted. For this reason, higher tensile residual stresses in matrix direction take places in glass/carbon hybrid and carbon/epoxy composites.

Tablo 5.5 Matrix Cracking Damage Parameter, e_m^2 due to thermal residual stresses at -50 °C

Specimen Type	**G1**	**G2**	**G3**	**H4**	**H5**	**H6**
Matrix Cracking Damage Parameter, e_m^2	0.208	0.169	0.208	0.662	0.662	0.699

Specimen Type	**K3**	**K4**	**K5**	**K6**	**K7**	**K1**	**K2**
Matrix Cracking Damage Parameter, e_m^2	1.011	0.984	0.939	0.662	1.039	1.014	0.834

CHAPTER SIX
IMPACT TESTS

6.1 Impact Test Machine

In this study, a FRACTOVIS PLUS impact test machine is used to investigate the impact behavior of the laminated composite plates. Test instrument consists of three main parts as following:

6.1.1 Upper part of the instrument

Automatic impactor recovery/releasing system is used to moves the impactor at the correct height and to release it for impact test on the specimen. *Additional energy system* is used to increase the speed of the impactor up to 24 m/s (with falling mass 2 kg) or 7 m/s (with falling mass 70 kg). The test instrument has capable the 1800 J maximum potential energy with the additional mass. The *impactor holder* joints mechanically the impactor to the recovery/releasing system. Moreover, it can contains one or more weights used to increase the impact mass. Up to 70 kg mass can be put into the impactor holder. Photograph of upper part of the Fractovis Plus impact test machine is given in Figure 6.1.

The *impactor* is used to strike the specimen surface when the impact test is carried out. It provide full details of the impact event from initial contact to final breaking of the specimen by recording the force/time curve of the entire impact event through a data acquisition system (DAS) connected to a PC. *Data acquisition system*, which the instrumented impactor is connected, can be take 16000 data during the impact event (Figure 6.2.c)

An *anti-rebounding system* is included in the test instrument to stops the impactor after impact to avoid the repeated impact on the specimen. The residual *energy absorbers* are used to damp the impactor residual energy after impact.

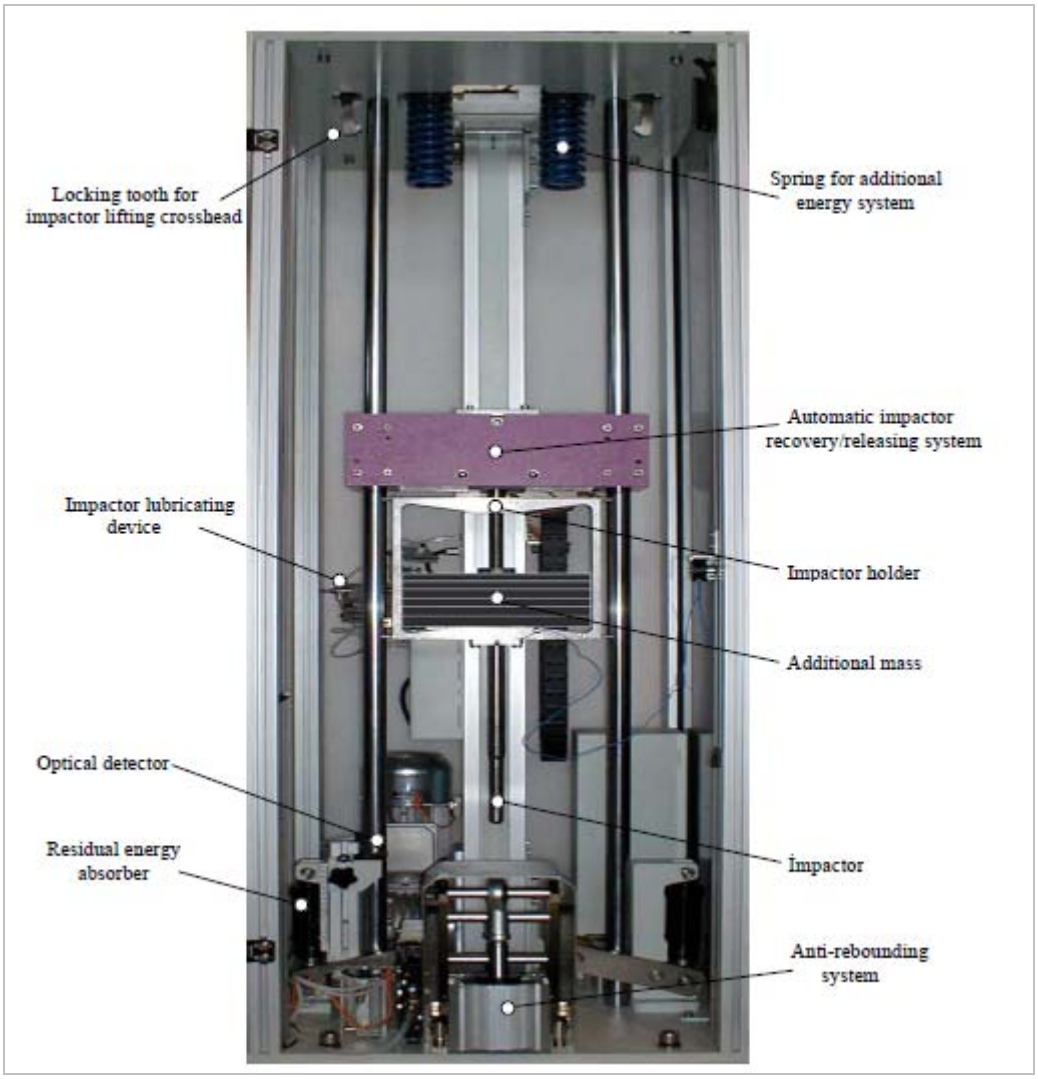

Figure 6.1 Photograph of upper part of the Fractovis Plus impact test machine (Aktas, 2007)

An *impactor lubricating device* used to lubricate the head of the impactor before the test. It consists of a pneumatic cylinder equipped with a sprinkler (a device that sprays oil) on its end and a small oil tank. When the test cycle starts the cylinder automatically moves forward until the sprinkler is positioned under the impactor head, at this point the sprinkler squirts the lubricating oil on the impactor head and the cylinder returns to the rest position.

The impact and rebound velocity optical detector is used to measure the velocity of the impactor just *before* the impact and to activate the impactor anti-rebound system in case of impactor rebound. It consists of a photocell fixed with a bracket to the structure and a flag fixed to the impactor holder. When the impactor holder is

released for test, the flag pass through the photocell interrupting the light-ray two times consecutively.

The *additional optical detector* measures the velocity of the impactor just *after* the impact and it is used to calculate the energy lost for the impact. It consists of a second photocell fixed below the first one through which pass the flag.

Figure 6.2 a) Fractovis Plus Low velocity impact tester and its equipments, b) impactor nose (1), piezoelectric impactor nose (2), c) Data Acquisition System (DAS), d) the specimen clamp mechanism , and e) the springs.

6.1.2 Lower part of the instrument

The FRACTOVIS PLUS impact test machine is equipped with an *environmental chamber* for specimens conditioning at temperatures range from -100°C to 150°C (Figure 6.2.d). The environmental chamber is cooled through the expansion of liquid nitrogen taken from an external tank. The nitrogen flows inside the chamber through pipes endowed with capillary holes. The chamber is heated by means of heating resistances. The uniformity of the temperature is assured through an electric fan which circulates air and nitrogen inside the chamber. The temperature set is automatically controlled by a temperature regulator. This device receives the signal from a temperature probe located inside the chamber and, depending on whether the requirement is for cold or hot, it enables a solenoid valve to open the nitrogen inlet or the electric heating resistance. Environmental chamber is equipped with *automatic clamping device*. It clamps the specimen on the support before the impact.

6.1.3 Data Calculation by Software

The developed VisualIMPACT software for Fractovis Plus impact test machine gives us the time versus load, velocity, deflection and energy histories. The impact force value at each time step, *F(t)*, are recorded by data acquisition system (DAS). The specimen deflection is calculated in main points. Deflection derives from a double integration of force curve as

$$\delta_i = \iint_i \frac{F(t) - g.M_{total}}{M_{total}} dt^2 \qquad (6.1)$$

where δ_i is deflection of the specimen up to point *i*, *F(t)* is force acquired by data acquisition system, *g* is gravity acceleration and M_{total} is total impact mass.

The absorbed energy up to point *i* is calculated as the area described under force-deflection F(δ) curve,

$$E_i = \int_i F(\delta).d\delta \tag{6.2}$$

The velocity up to point *i*, derives from a single integration of force-time curve,

$$v_i = \int_i \frac{F(t) - g.M_{total}}{M_{total}} .dt \tag{6.3}$$

When the impact force value at each time step, *F(t)*, are recorded by data acquisition system, the load-deflection, load-time, velocity-time, impact energy-time curves can be obtained with help of Equations (6.1), (6.2) and (6.3).

6.2 Impact Test Procedure

Low impact tests were carried out on all specimens at 20, 90 and -50 °C temperatures by means of FRACTOVIS PLUS Drop Weight Test Machine. This machine is capable of impacting samples at energies of up to 755 J utilizing a spring-assist. For this study, all samples were impacted with a 5.22 kg drop weight. Since the drop weight was not changed, the different impact energies were achieved by adjusting the drop height. A pneumatic clamping fixture, with a 76.2mm diameter opening, secured each sample during impact. The samples were impacted with a 12.7 mm diameter striker with hemispherical tip, constructed out of high strength steel. The machine has a climatic chamber for impact test under low (up to -70 °C) and high (up to 150 °C) temperature conditions. The temperature of the specimens is monitored by a thermocouple. A temperature controller at low temperatures regulates the opening of an electro valve, which allowed a controlled volume of liquid nitrogen to enter the chamber (Figure 6.3). Once the desired temperature was reached in the chamber, the system keep it about 20 min to ensure that specimens and inner atmosphere remained at the test temperature. After that, impact tests were started to be performed.

Figure 6.3 View of climatic chamber at -50 °C

6.3 Impact test results

6.3.1 Impact Test Results of Glass/Epoxy Laminated Composites with Layers

After subjecting the C1, C2 and C3 specimens to 20, 50 and 90 °C temperature conditions in the climatic chamber, three specimens from each type were tested at impact energies ranging from 4 J to 22 J and the average of the three was taken to determine the absorbed energy, the peak load, deflection at peak load and damage areas. Contact force versus deflection and energy profile diagrams were plotted for each type and temperature in order to compare and understand stacking sequence and temperature effects on impact behavior of glass/epoxy composite laminates in an impact event. In addition, variations of damage areas were investigated through impact energy levels ranging from 4 J to 22 J under the temperatures.

6.3.1.1 Contact Force -Deflection Curves

Load–deflection (F–d) curves under various impact energies provide an understanding of impact response and impact-induced damage mechanisms of

composite laminates. Load–deflection (F–d) curve at energy levels ranging from 4 J to 22 J at 20 C for $[0/0/90]_s$ orientation is illustrated in Figure 6.4.

The curves collectively have a mountain-like shape and can be classified into two basic types; closed curve and open curve through impact process. Curves at energy levels ranging from 4J to 14 J are closed type and the entire descending section consists of rebounding, since both the load and deflection decrease. As the impact energy increases from 16 J to 22 J the F–d curves become open and do not contain any rebounding part. The curve at about 16 J corresponds to the initiation of perforation while that at about 20 J to the complete perforation. Similar results were also obtained for other orientations and temperatures. For comparison, since the energy profile diagrams are more explanatory, the other force-deflection curves are not given here.

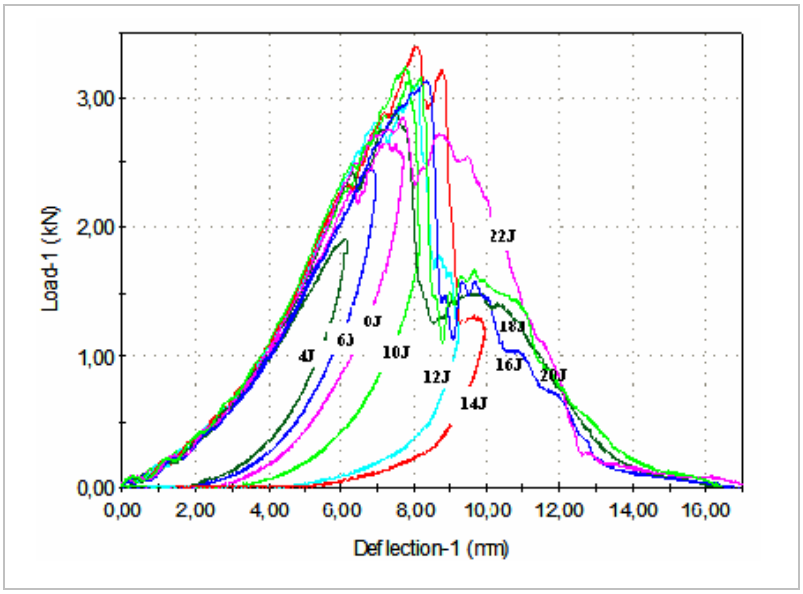

Figure 6.4 Load–deflection (F–d) curve at energy levels ranging from 4 J to 22 J at 20 C for $[0/0/90]_s$ orientation, C1 laminate.

6.3.1.2 Energy Profile Diagrams

Impact energy (E_i) and absorbed energy (E_a) are two important parameters to evaluate impact response and resistance of composite structures. The impact energy is defined as the total amount of energy introduced to a composite specimen. The

absorbed energy (E_a) is defined as the entirely of energy absorbed by the specimen at the end of an impact event. The diagram showing relationship between E_i and E_a is called as ‘‘energy profile”. By comparing the corresponding load–deflection curves, energy profile diagram (EPD) and images of damaged specimens, it enables to reconstruct the damage process of individual laminates. By using energy profiling method, it becomes achievable to characterize some impact properties such as pure elastic limit, penetration and perforation thresholds. The shape of an energy profile diagram, in general, may be influenced by a number of factors associated with both the impactor and target. Among those, the constituent materials, geometry of fibers, thickness and stacking sequence of target, and shape of the impactor can be given as examples. A general schematic illustration of energy profile diagram is given in Figure 6.5. As shown in the figure, a diagonal line, which is called the equal-energy line, is added to the diagram in order to representing the equality between impact and absorbed energies. It consists of three regions; AB, BC and CD. Here, AB represents a region in which specimens remain non-penetrated. As expected, the extent of damage in specimens is dependent on the impact energy, i.e. overall damage area increases by increase of impact energy. In this region, the curve is below the equal energy line, implying that there is excessive impact energy (the difference between the curve and the equal energy line). The excessive energy is retained in the impactor and used to rebound the impactor from the specimen at the end of an impact event (Liu, 2004). Region BC is termed as the penetration range where the whole impact energy is likely absorbed by specimens. And, region CD stands for specimens perforated. In addition, point B and C represent the penetration and perforation thresholds, respectively. The penetration threshold can be defined as the point where the absorbed energy equals the impact energy for the first time. Namely, at penetration threshold, the impactor sticks into specimens and does not rebound any more. The perforation threshold is defined as the absorbed energy when the tip of the impactor reaches the back surface of the specimen. (Aktas, Atas, Icten, & Karakuzu, 2008)

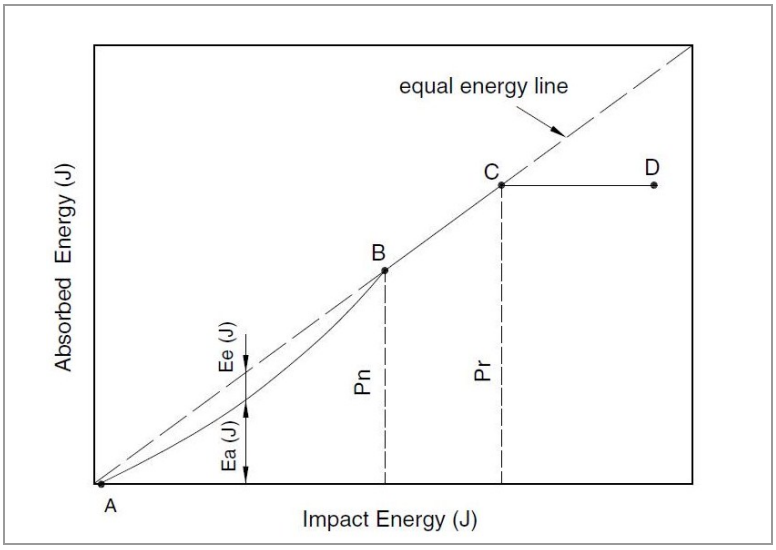

Figure 6.5 Energy profile Diagram

Ideally, penetration should take place when the hemispherical nose completely buries into the specimen in case the specimen is thick enough. However, it should also be noted that it is hard to observe such a penetration when the specimen is much thinner than the radius of the impactor nose. The impactor nose had a hemispherical shape with a radius of 6.35 mm while average thicknesses of the composite specimens used in this study are ranging from about 1.5 to 2 mm. Accordingly, the specimen should be very close to perforation when penetration took place and there is not a definite point to be considered as penetration threshold in this study. Therefore, the difference between perforation and penetration threshold energies was taken no notice for all this study.

Energy profile diagrams of glass/epoxy laminated composite plates with lay-up $[0/0/90]_s$, $[90/0/0]_s$, $[0/90/45]_s$ are drawn as shown in Figure 6.6 for all temperatures. The curves indicate that up to the impact energy of 10 J, absorbed energy increases with increasing temperature. However, at impact energies ranging from 12 to 22 J, variation of absorbed energy is different for all orientations. For example, with increasing temperature, while absorbed energy decreases for $[0/90/45]_s$, it increases for $[90/0/0]_s$. This indicates that not only variation with temperature in material properties of composite laminates but also stacking sequences influence the absorbed energy under the same impact energy. Also, another important result is that at room

temperature and low energy levels, the highest absorbed energy is obtained in composite plate with lay-up $[0/0/90]_s$, as shown in Figure 6.6.a.

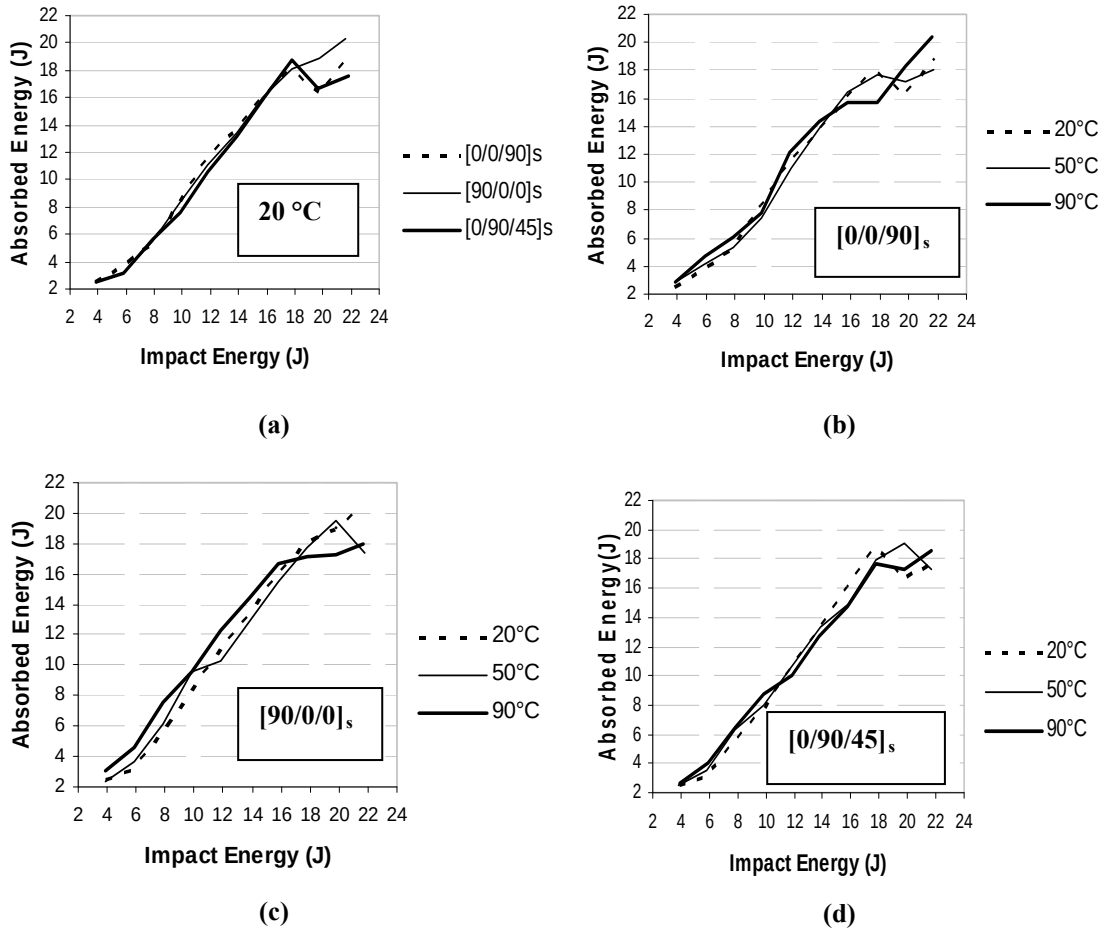

Figure 6.6 Energy profile diagrams of glass/epoxy laminated composite plates with lay-up $[0/0/90]_s$, $[90/0/0]_s$,

6.3.1.3 Visual Examination

External damages occurring in glass/epoxy laminated composites under impact loading were observed by visual inspection of the specimens. Generally, the impacted surface of the specimen shows a concave indentation caused by the impactor. The curvature of the indentation zone coincides with that of the impactor tip. In addition, Indentation grows as the impact energy increases. In all the laminates and test temperature conditions, fiber fracture and matrix cracks transverse to the fibers were seen in the indentation crater at high impact energies (from 12 J up to 22

J). On the back surface of the specimen, it was observed that, matrix cracking, fiber fracture and fiber pull-out concentrated on a large zone centered around the impact point. In addition, a kind of delamination (debonding), resulting from the local deformation of the fibers rather than the difference between the rigidities of two bottom plies at point of impact was also observed. For lower impact energies (less than 12 J), the main damage mode was detected as delamination and matrix cracks rather than fiber fracture.

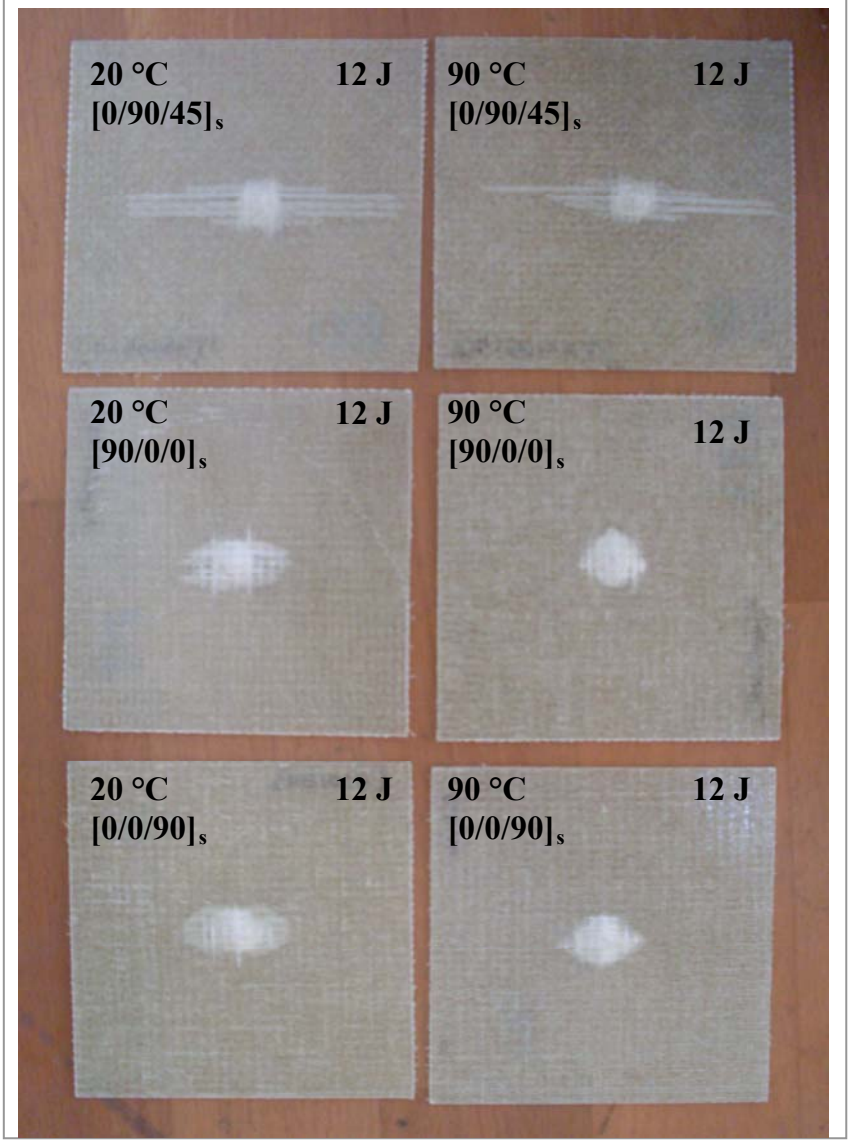

Figure 6.7 Delaminations occurring on back surface of the specimens subjected to impact energy of 12 J at temperatures of 20 and 90 °C

Figure 6.7 shows the delaminations occurring on the back surface of the specimens subjected to impact energy of 12 J. at temperatures of 20 and 90 °C. Specimens with lay-up $[0/90/45]_s$ have higher delamination areas in comparison with $[0/0/90]_s$ and $[90/0/0]_s$. In addition, it is clearly observed that damage area decreases with increasing temperature.

6.3.1.4 Measurement of Delamination Areas

In order to measure delamination areas in different kinds of composite materials, several techniques, such as high-intensity light, penetrant-enhenced X-ray radiography, an ultrasonic imaging system and edge replication are used (Liu,1988). In this investigation, a high-intensity light was used to identify the projected delamination areas in the impacted glass/epoxy composite laminates. By this method, delamination area versus impact energy curves were obtained for each type of composite laminates and temperature for impact energy levels from 4 J to 22 J as shown in Figures 6.8-10.

From the curves, it is observed that, up to 12 J, as impact energy increases, delamination area increases for all orientations. On the other hand, after 12 J, irregular variations in the curves are noticed. The irregularity in stacking sequences $[0/0/90]_s$ and $[90/0/0]_s$ seem to be more than $[0/45/90]_s$ due to more mismatching effects which play significant role in delamination damage. Besides, as the variation of the delamination area with temperature is considered for the same orientation and impact energy, it is seen that delamination area decreases with increasing temperature. At high temperatures, since epoxy matrix showed more ductile behavior, elastic properties and strength of composite laminates, especially, in transverse direction, decreased; impactor tip caused damage on a smaller area. Furthermore, as indicated earlier, thermal residual stresses and thermal-induced interlaminar shear stresses at high temperatures are lower. This trend also contributes to the reduction in the delamination area.

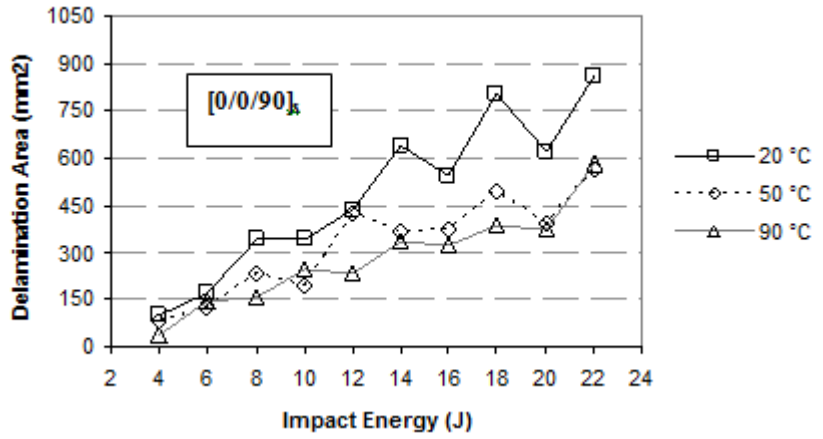

Figure 6.8 Delamination area versus impact energy curves for $[0/0/90]_s$ orientation

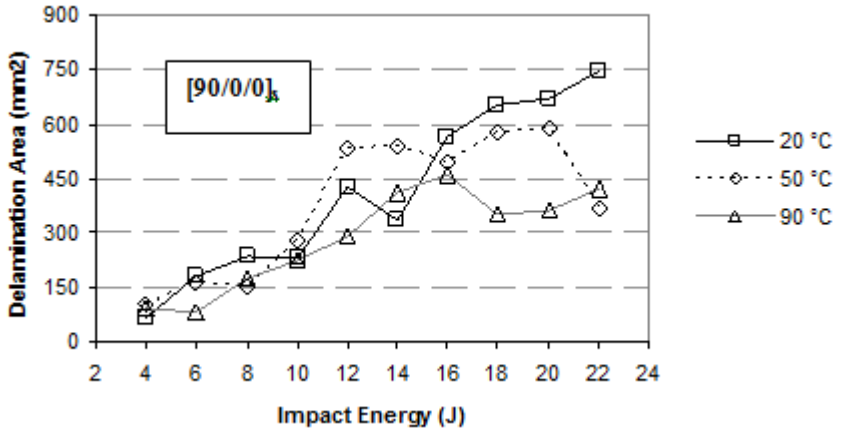

Figure 6.9 Delamination area versus impact energy curves for $[90/0/0]_s$ orientation

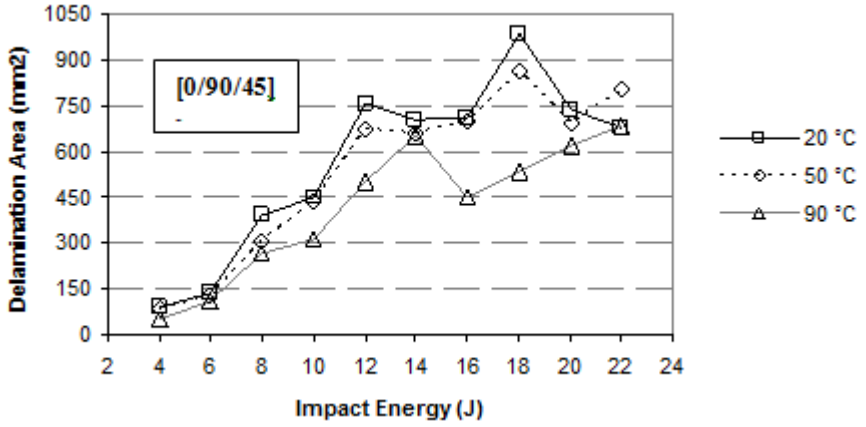

Figure 6.10 Delamination area versus impact energy curves for $[0/90/45]_s$ orientation

6.3.2 Impact Test Results of Dry Laminates with eight layers

G1, G2, G3, H4, H5, H6, K3, K4, and K5 samples were subjected to various impact energies increasing from 5 J to 55 J in intervals of 5 J until complete perforation take place at 20 90 and -50 °C temperatures. Also, impact tests on K1, K2, K6 and K7 laminates at the mentioned temperatures are performed under energy levels ranging from 5 J up to 35 J, since absorbed energy is not increased after impact energy of 35 J. Each test was repeated three times for each specimen type and temperature since the close results were obtained.

6.3.2.1 Effects of Impact Energy Level

In order to investigate the energy level effects on the impact behavior of the composite plates, five impact energies from 10 J to 50 J are selected for G1 composite plate. Figure 5.12.a-e is given for an example of the contact force-deflection contact force-time, energy-time, velocity-time, deflection-time curves, respectively.

Figure 6.11.a shows F–d curves of G1 specimens. The curves collectively have a mountain- like shape. Individually, however, there are two basic curve types; closed curve and open curve. The curves for impact energies from 10 to 40 J represent closed type while the curve at 50 J impact energy, open type. The curve at 50 J implies initiation of perforation.

At low impact energies of 10 and 20 J, F–d curve is of a closed type and the entire descending section consists of rebounding, because both the load and deflection decrease. In these cases impact load does not result in a serious damage to specimens apart from minor matrix cracks. The fiber fracture due to bending and fiber debonding start to take place at impact energy of 30 J. Such a damage mechanism reduces the stiffness of specimens and is reflected on the F–d curve as a plateau around the peak force, as the impact energy continues to increase, the F–d curves become open, instead of closed one. They do not contain any rebounding part.

Figure 6.11.b shows five contact force–time (F–t) curves of G1 specimens with a lay-up $[90/0/0/90]_s$ at impact energies ranging from 10 to 50 J. When the impact energy is low, such as, 10 and 20 J, the F-t curves are of parabolic shapes, and the maximum contact force increases with the increase of impact energy. For the higher impact energies resulting in significant damages inside specimens, the contact force is of approximately a constant peak value for all cases around 6.5 kN for G1 laminate, as seen in Figure 6.11.b. Like F–d curves, the sudden drop in contact force for 30 J and higher impact energies, implying a momentary loss of contact between impactor and specimen due to a serious bending fracture of fibers at the bottom (non-impacted) side of the specimen.

Variation of the absorbed energy, calculated from associated contact force–deflection curves, with real time is given in Figure 6.11.c. The amount of energy transferred from the impactor to composite specimens at the end of impact events, i.e. absorbed energy, increases with the impact energy since a higher impact energy results in a more severe damage to a composite specimen. As seen from the figure, each curve increases (during loading) with time, reaches a maximum value and then decreases (during unloading), and finally remains horizontal, i.e. reaches a constant value. This constant value gives the total energy absorbed permanently by composite specimens at the end of an impact event. The maximum value of each curve represents for the associated impact energies. The difference between them is termed as excessive energy. The excessive energy is retained in the impactor and used to rebound the impactor from the non-perforated specimens. As shown in the figure, there is no excessive energy at impact energy of 50 J, owing to the occurrence of perforation case.

Variation of the velocity with real time for varied impact energies is given in Figure 6.11.d. As expected, each curve is of the highest value at the beginning of impact event, i.e. at the instant that time is zero. For non-perforated G1 specimens, the velocity decreases versus time and becomes zero around the time that maximum deflection is reached. Then, for impact energies ranging from 10 to 40 J, the curves

have negative values, implying rebounding of the impactor. However, for perforated G1 specimens at impact energy of 50 J, velocity curves versus time have no negative sections, implying no rebounding.

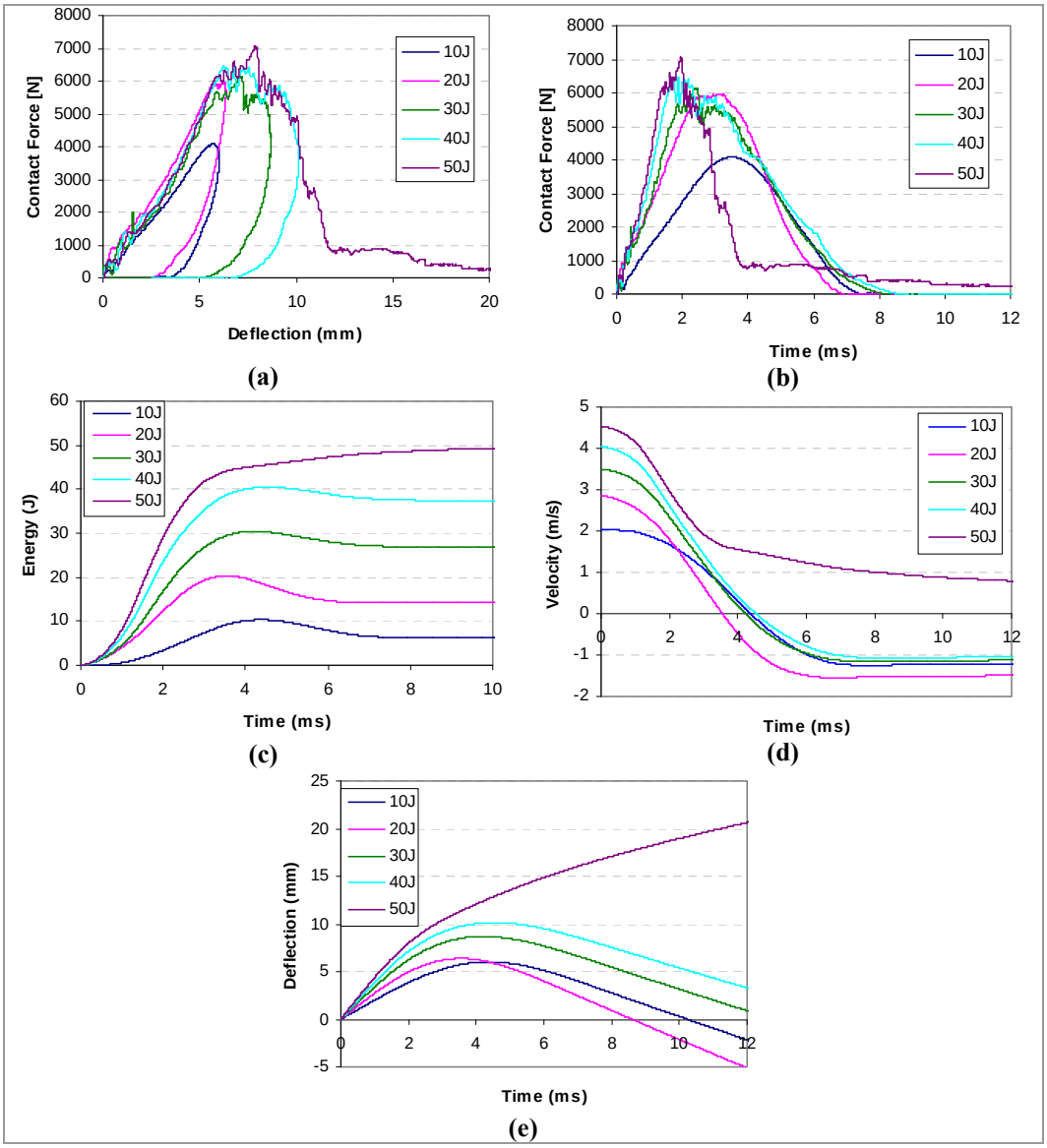

Figure 6.11 The specific curves at various impact energies for the G1 laminate

Figure 6.11.e shows the deflection–time (d–t) curves of G1 specimens. From the comparison of F–t curves and d–t curves, it is observed that it takes more to reach maximum deflection compared to contact force. That is, the impactor continues to move downward to some extent after maximum load is reached. That time delay increases with the increase of impact energy. On the other hand, for non-perforated specimens, it takes longer for impactor to return back to its initial position, the

position that right before impact event took place, as impact energy increases from 10 J to 40J. It implies more amounts of damaged fibers due to increased impact energies.

6.3.2.2 Effects of Stacking Sequences and Temperature on Impact behaviors

Energy profile diagrams and contact force-deflection curves were plotted for each specimen type and temperature to compare impact responds and resistances of the specimens. For comparisons of rebounding cases, contact force-deflection curves were obtained at impact energies of 30 J for G1, G2, G3, H4, H5, H6, K3, K4, and K5 specimens and 15 J for K1, K2, K6 and K7 specimens. Contact force-deflection curves in perforation cases of the specimens were obtained for 55 and 35 J, respectively.

The initiation, perforation and propagation energy values of the specimens were determined by using contact force-deflection and energy-deflection curves at high impact energies inducing perforation case. Herein, Perforation energy i.e. total energy absorbed by specimen in case of perforation is considered by the sum of two regions; the initiation energy before maximum contact load and the cumulative propagation energy after maximum contact load. However, for the composite laminates, especially glass/epoxy composites used in this study, the composite failure process was initiated earlier than the maximum load point, as shown in Figure 6.12. Therefore, the energy to yield point was used as the initiation energy, where the contact force versus deflection curve starts to change slope.

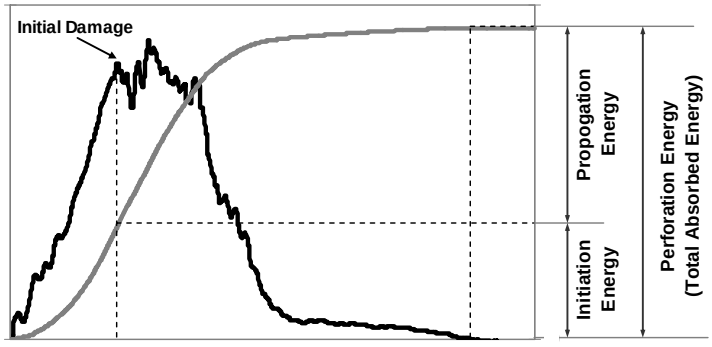

Figure 6.12 Contact force-deflection and energy-deflection curves in case of perforation

The mentioned specific energy values were obtained for each type of specimens and temperature, as shown in Table 6.1-2. It is seen from the tables that with decreasing temperature from 90 °C to -50 °C, perforation energy increases and initial energy decreases. The reason for higher perforation energy at lower temperature is that damage area is greater and impact energy dissipates on larger area. Also, reduction of the initial energy with decreasing temperature is due to high in-plane thermal stresses at low temperature and therefore, delamination is generated easily since the energy required to cause damage reduces as the temperature decreases. When effects of orientations on the specific energies are investigated, it is seen that the initiation energy of G2 laminate are greater than that of G1 and G3 laminates. This is since angle difference between adjacent layers for the orientation is lower in comparison with the others and delamination does not take place between adjacent layers having the same orientation angle. Perforation energy of G2 laminate is lower than other orientations. This is owing to occurrence of more matrix cracks in laminates with a lay up $[90/0/45/45]_s$. It is concluded that cross-ply laminated composites are advantageous in terms of perforation energy threshold. The results also can be obtained from force-deflection curves at high impact energies.

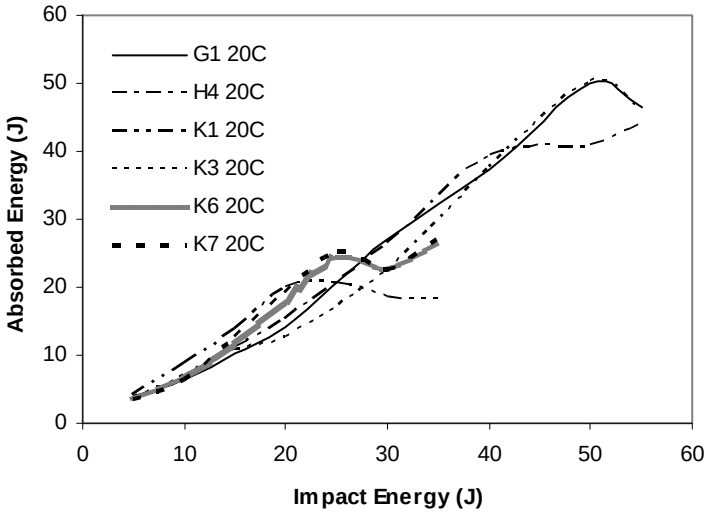

Figure 6.13 Energy profile diagrams of cross-ply laminated composites

Energy profile diagrams of cross-ply laminated composites are given in Figure 6.13. It is seen that impact resistance of glass/epoxy laminates is higher about two times than that of carbon/epoxy laminates for the same orientations. The perforation thresholds of hybrid composites consisting of glass and carbon fibers

have the values between that of glass/epoxy laminates and carbon/epoxy laminates expect for K3 laminate. K3, K4 and K5 specimens supplies higher impact resistance when compared to the other configurations, because of carbon woven fabric used on upper and lower layers.

To facilitate the comparisons of impact characteristics of laminates, the initiation, perforation and propagation energies are given in Table 6.1-2. When effects of orientations on characteristic energies are investigated, initiation energies of laminates with lay-up $[90/0/45/45]_s$ (G2, H5, K2, K5 laminates) are higher than their other orientations. This is because angle difference between adjacent layers for the orientation is lower in comparison with the others and delamination does not take place between adjacent layers having the same orientation angle.

When the absorbed energies in case of perforation are investigated, perforation energies of laminates with lay-up $[90/0/45/45]_s$ is lower than the other orientations. This is owing to occurrence of more matrix cracks in laminates with a lay up $[90/0/45/45]_s$. Therefore, it can be concluded that cross-ply laminated composites are advantageous in terms of perforation energy threshold. When change of characteristic energy with temperature is examined, different results are obtained according to reinforcement material used. For G1, G2, G3 glass/epoxy and H4, H5, H6 glass/carbon hybrid laminates, propagation energy decreases with increasing temperature. At high impact energies, temperature variations do not affect damage areas in K1 and K2 carbon/epoxy laminates so much as glass/epoxy and glass/carbon hybrid composites. This is since shear-out failure mode takes place much more and the energy dissipates on a smaller zone in comparison with glass/epoxy laminates. Therefore, absorbed energy at high energy, i.e., perforation energy in carbon/epoxy laminates increases with increasing temperature.

When the effect of temperature variations on the initial energy of the composite specimens is considered, initial energies increases for all types of specimens while temperature increases from -50 to 90 °C. As mentioned earlier, the reason of this

trend is probably that thermal residual stresses which contribute to matrix cracks decreases with the increased temperature.

When antisymmetric stacking sequence, K7 laminate, is compared with symmetric stacking sequence, K6 laminate, K7 specimen does not provide any advantages in terms of characteristic energies, but a smaller delamination area is present on back side of K7 laminate as compared to K6 laminate at the same impact energy (Figure 6.25-26).

Table 6.1 Characteristic energies for each specimen type at 20, -50 and 90 °C temperatures

Specimen Type and Temperature	Initiation Energy (J)	Total Absorbed Energy (J)	Propagation Energy (J)
G1 20C	16.30	46.46	30.16
G2 20C	27.62	44.80	17.18
G3 20C	18.55	44.50	25.95
H4 20C	14.40	44.01	29.61
H5 20C	19.48	37.07	17.59
H6 20C	15.61	35.74	20.13
K1 20C	4.36	18.18	13.82
K2 20C	6.64	19.96	13.32
K3 20C	21.59	50.37	28.78
K4 20C	22.07	49.93	27.86
K5 20C	28.09	49.34	21.25
K6 20C	14.17	26.52	12.35
K7 20C	12.97	27.03	14.06
G1 90C	20.07	44.10	24.03
G2 90C	24.30	42.38	18.08
G3 90C	20.69	39.32	18.63
H4 90C	21.85	47.31	25.46
H5 90C	26.23	36.13	9.90
H6 90C	18.12	35.92	17.80
K1 90C	8.38	23.04	14.66
K2 90C	10.11	21.01	10.90
K3 90C	30.32	57.74	27.42
K4 90C	29.33	45.36	16.03
K5 90C	34.32	46.45	12.13
K6 90C	15.37	34.39	19.02
K7 90C	20.06	32.96	12.90

Table 6.2 Characteristic energies for each specimen type at -50 °C temperature

Specimen Type and Temperature	Initiation Energy (J)	Total Absorbed Energy (J)	Propagation Energy (J)
G1 -50C	15.18	53.86	38.68
G2 -50C	21.34	50.32	28.98
G3 -50C	17.43	54.05	36.62
H4 -50C	13.75	47.12	33.37
H5 -50C	19.97	40.41	20.44
H6 -50C	13.58	42.54	28.96
K1 -50C	4.11	17.05	12.94
K2 -50C	6.14	18.15	12.01
K3 -50C	22.33	53.84	31.51
K4 -50C	20.15	52.73	32.58
K5 -50C	18.57	51.48	32.91
K6 -50C	9.75	25.28	15.53
K7 -50C	8.93	22.19	13.26

6.3.2.3 Contact Force-Deflection Curves

Contact force–deflection (F–d) curves under various impact energies are the signature of a composite material's response to impact loading. The contact force can be defined as the compressive load exerted on impactor by specimens. Contact force-deflection curves were obtained by using the contact force-real time history. Characteristic of load–deflection curves includes some useful tips in assessing damage process of composite structures. Load–deflection curves of the specimens at intermediate and high impact energies: 30 J and 55 J for G1, G2, G3, H4, H5, H6, K3, K4, and K5 laminates; 15 J and 35 J for K1, K2, K6 and K7 laminates are given in Figures 6.14-17. The curves collectively have a mountain-like shape. Individually, however, there are two basic types, closed curve and open curve. Closed curves given in Figures 6.14-15 represent the partial rebounding of the impactor from the specimen at intermediate impact energies of 15 and 30 J. If load–deflection curve is an open curve, the impactor penetrates into the specimen or even perforates the specimen. Open curves in Figures 6.16-17 specify perforation case of the specimens at high impact energies of 35 and 55 J. The curves consist of an ascending section of loading and a descending section combining loading and unloading. The ascending section represents the bending stiffness history of the composite material under impact loading. The slope of load-deflection curve in ascending section is associated with the stiffness. Therefore, the bending stiffness of

the laminates can be compared by means of the curve. As shown in Figure 6.14.a, the slope of the load-deflection curve of G3 laminate at impact energy of 30 J is higher in comparison with that of G1 and G2 laminates. Therefore, G3 laminate has the highest bending stiffness. However, maximum contact force has the highest value in G2 laminate in spite of its lower bending stiffness than G3 laminate. This is because mismatching effects which start delamination are lower and the initial energy required to cause the damage are greater in G2 laminate. When variation of contact force-deflection curve with temperature is investigated for G1 laminate, it is seen from Figure 6.14.b that both maximum contact force and the slope of the curve are higher at -50 °C, compared to 90 and 20 °C. Also, permanent indentation depth decreases while the temperature is decreasing from 90 °C to -50 °C. For instance, permanent indentation occurring in G1 laminate at impact energy of 30 J is 2.8 mm at -50 °C while 6.8 mm at 90 °C. This is since glass/epoxy laminated composites resist impact load in a brittle manner at low temperature. The close results were also obtained for G2 and G3 laminates.

The oscillations in the curves increase with decreasing temperature, as shown in the figures. In addition, for intermediate impact energies, permanent and maximum deflections of the laminates decrease with decreasing temperature from 90 to -50 °C, expect for the K1 and K2 laminates. More oscillations take place in carbon/epoxy laminates (K1 and K2 samples) because of its more brittle structure in comparison with glass/epoxy (the G1, G2 and G3 laminates) and glass/carbon hybrid composites (the H4, H5, H6, K3, K4 and K5 laminates)

As shown in Figures 6.17.e and g, K3 and K6 laminates present high impact resistance at 90 °C temperature, since the partial rebounding takes place while complete perforation occurs in other specimens.

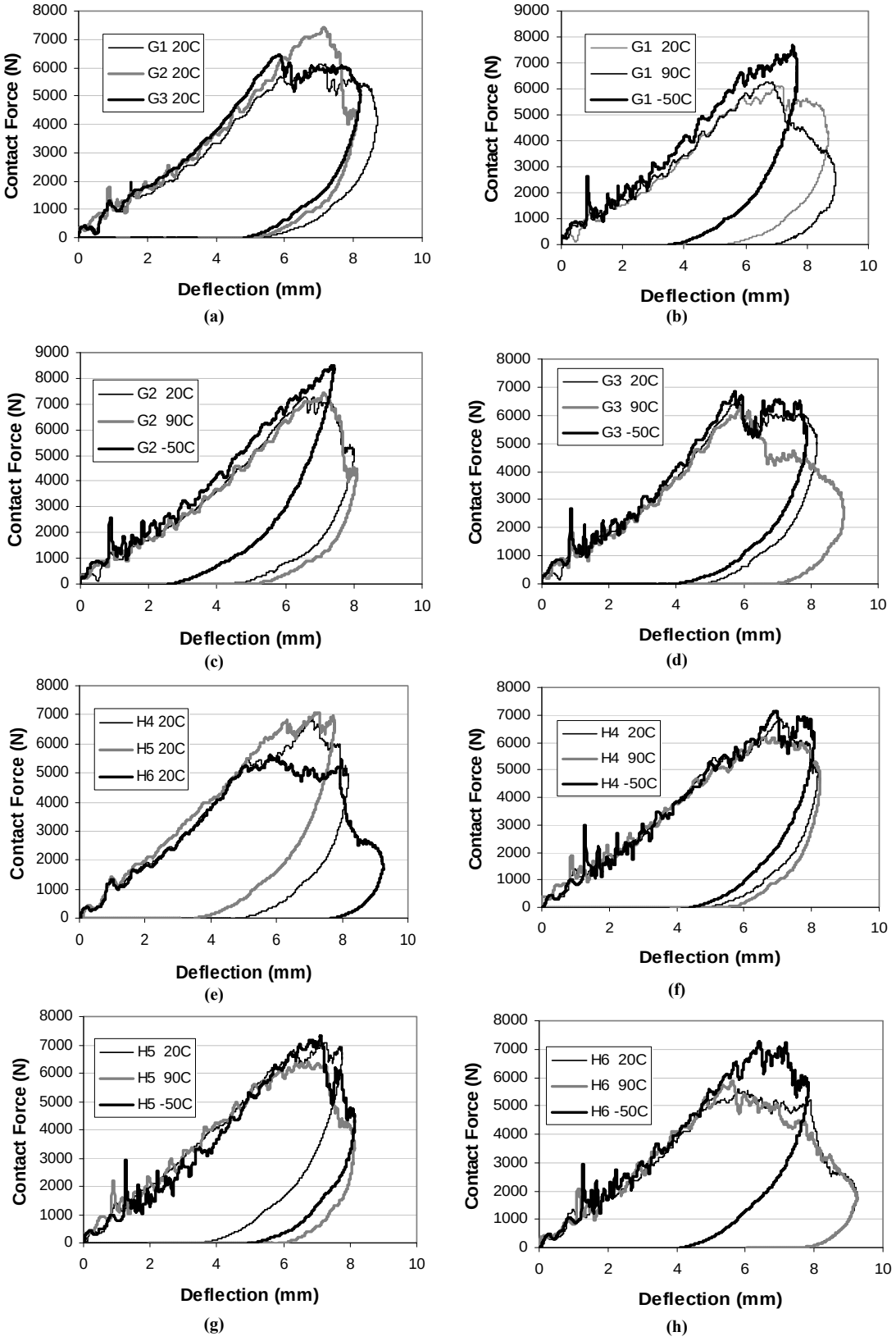

Figure 6.14 Contact force-deflection curves for 15 and 30 J impact energies

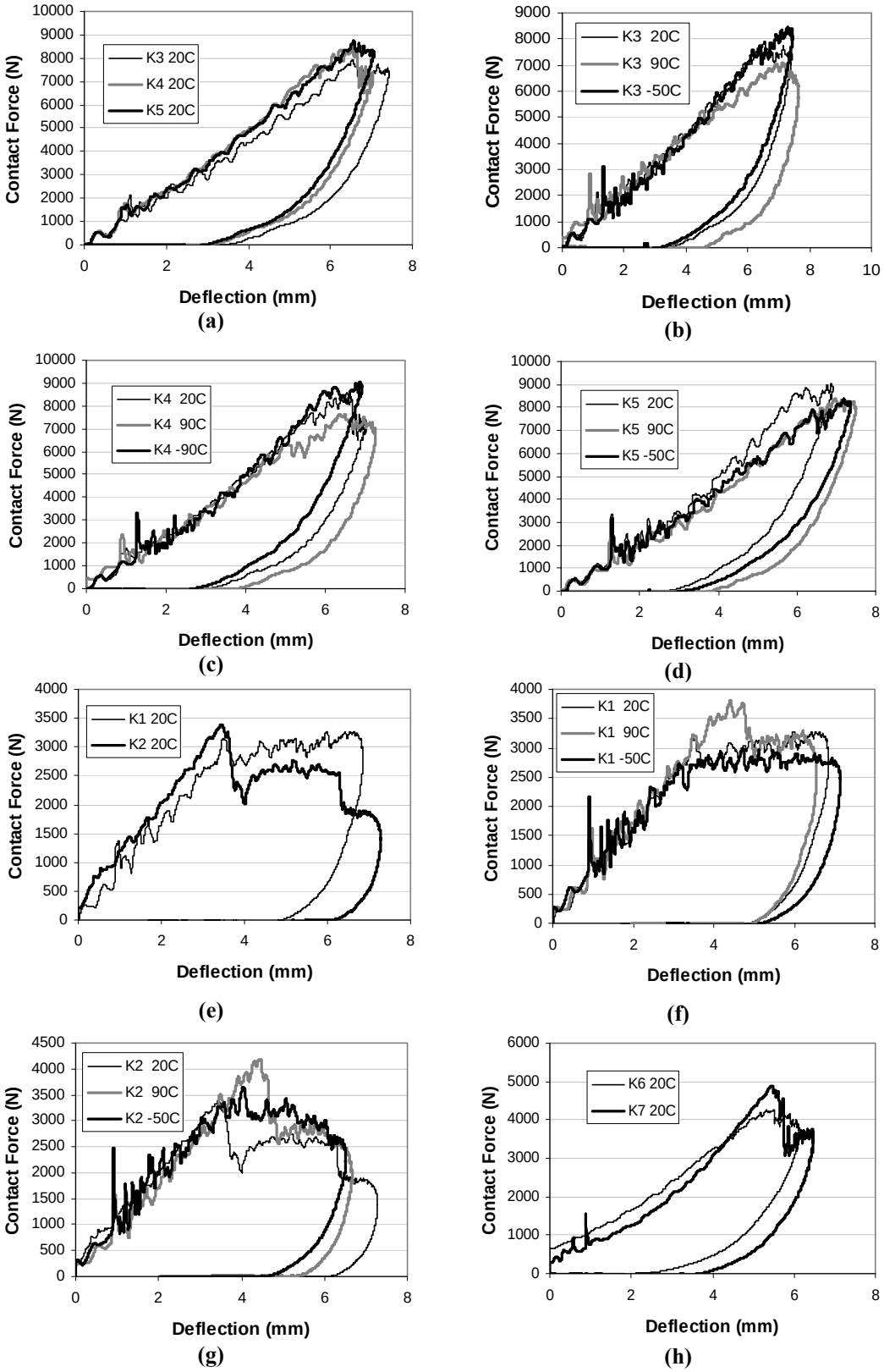

Figure 6.15 Contact force-deflection curves at impact energies of 15 and 30 J

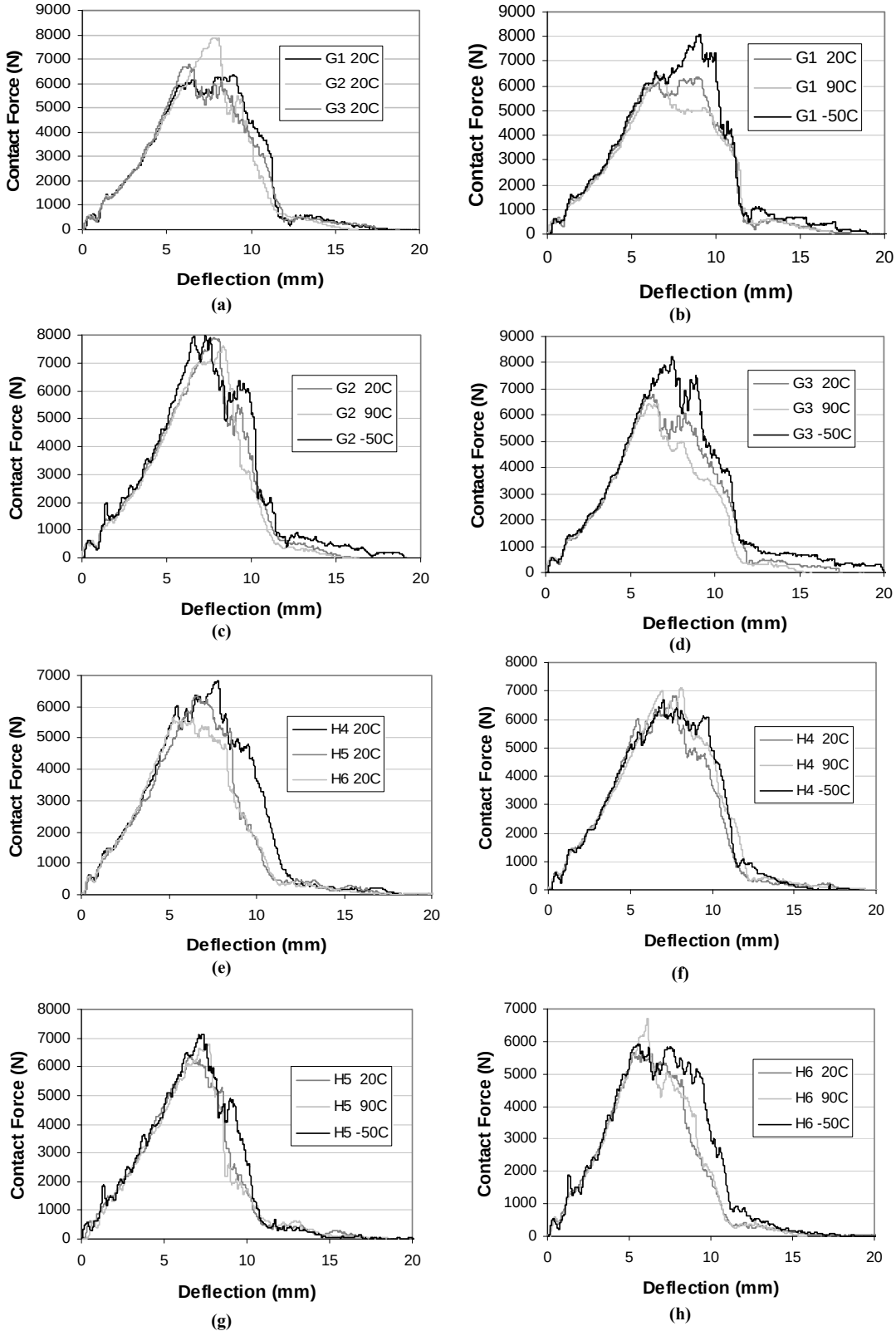

Figure 6.16 Contact force-deflection curves for 35 and 55 J impact energies

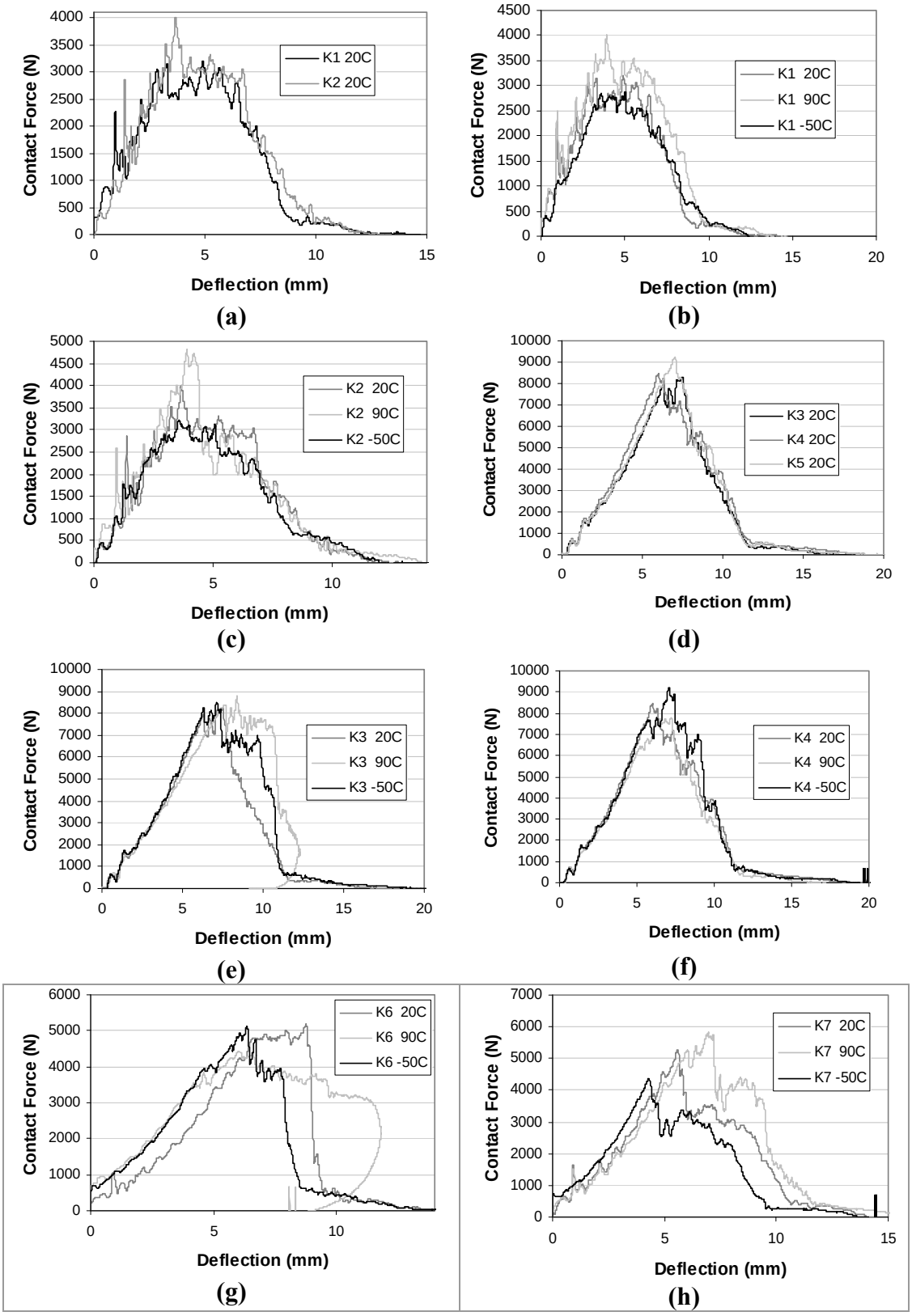

Figure 6.17 Contact force-deflection curves for 35 and 55 J impact energies

6.3.2.4 The Specific Curves at the Impact Energy of 15 J

Impact behaviors of the composite specimens with lay up $[90/0/090]_s$ having highest perforation threshold were compared at impact energy of 15 J by using the contact force-deflection contact force-time, energy-time, velocity-time and deflection-time curves, respectively.

While the slope of contact force-deflection represents the contact stiffness, the enclosed area under the curves gives the absorbed energy. A drop after an initial peak, indicating the change of the composite from the intact to a damaged state, was followed by the peak force when the maximum deflection was reached. If contact force-deflection curve given in Figure 6.18.a is investigated, it is seen that K3 specimen has the highest stiffness and maximum contact force since its required energy for initial damage is the highest value and it has the highest bending rigidity in comparison with the other configurations. Therefore, using woven fabric carbon fiber at the outside layers in glass/carbon hybrid composite plates provides high impact resistance. Maximum contact force in G1 and H4 specimens is about 5 kN while it is 5.2 kN for K3 specimens. Although K1 carbon/epoxy composite has higher bending stiffness, its maximum contact force is about 3 kN. This is because carbon/epoxy composite has brittle construction and its initial energy is about 5 J while 16, 14 and 21 J for G1, H4 and K3 laminates, respectively. At 15 J impact energy, complete rebounding take places in G1, H4 and K3 specimens while partial rebounding for K1 laminate. As shown in Figure 6.18.b, contact duration in K1 specimen is higher as compared to other configurations because of the occurrence of matrix cracks and delamination in K1 specimen. Also, absorbed energy and maximum deflection in K1 specimen is highest in comparison with G1, H4 and K3 laminates (Figure 6.18.c and e). Rebounding velocity after the tip of the impactor drop onto the plate is smallest for K1 laminate because of its higher permanent deflection when compared to G1, H4 and K3 specimens (Figure 6.18.d).

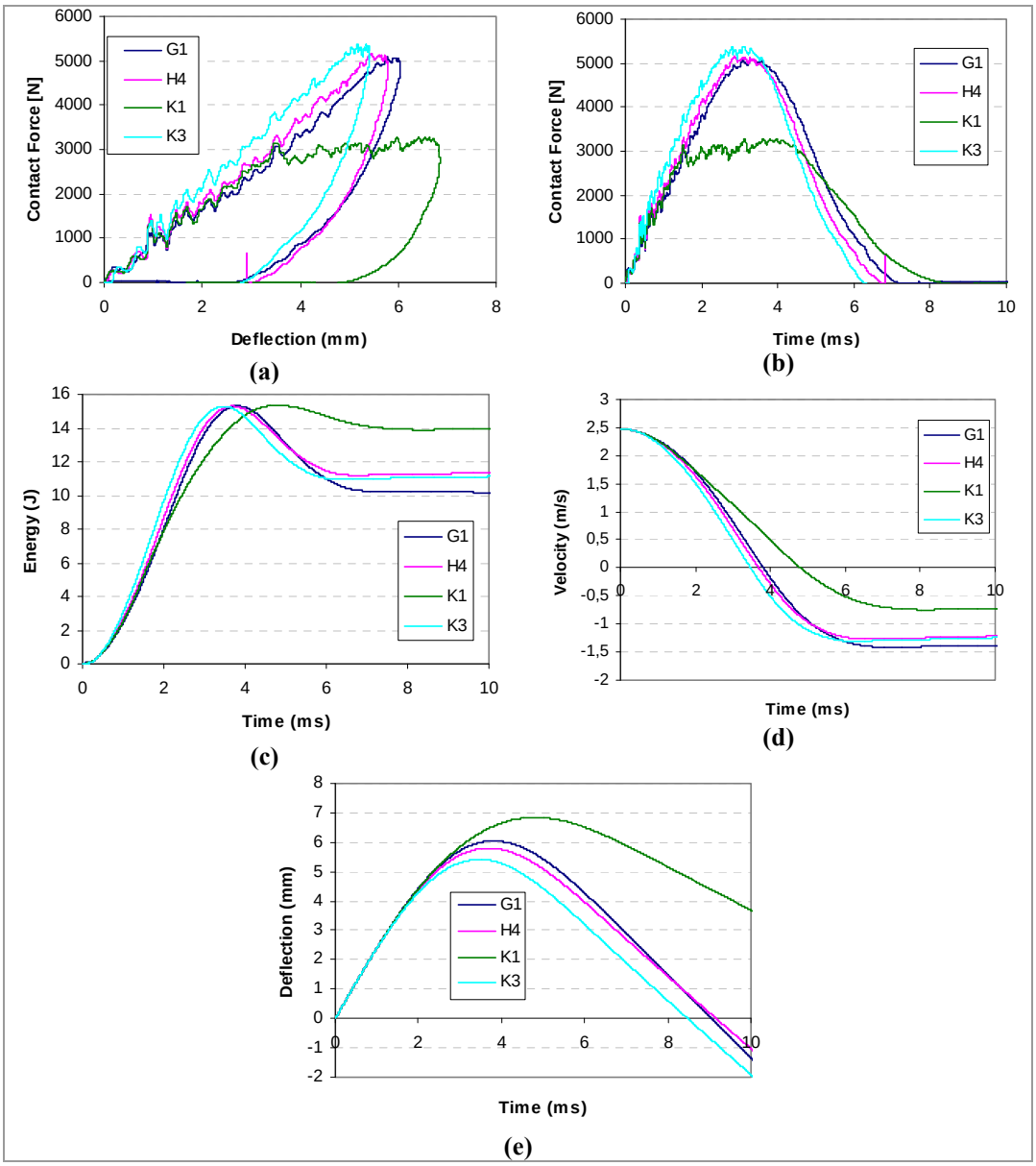

Figure 6.18 The specific curves of the cross-ply composites at the impact energy of 15 J

6.3.2.5 Energy Profile Diagrams and Maximum Contact Force versus Impact Energy Curves

Absorbed Energy versus impact energy curves, i.e., energy profile diagrams of some specimens are given in Figure 6.19. At low impact energy levels, absorbed energy is not dependent on orientation in the laminates having the same fibers. For example, the values of the absorbed energy at 20 °C in the G1, G2, and G3 laminates are nearly identical for impact energies ranging from 5 to 20 J. This finding is also valid for the H4, H5, H6 and K3, K4, K5 laminates as in Figures 6.19.b, c, d and f.

At intermediate impact energy levels, the laminates with lay up $[90/0/45/-45]_s$ absorb the energy more in comparison with the other orientations. For instance, at 30 J impact energy, the absorbed energy of the H6 laminate with a lay up $[90/0/45/-45]_s$ is 29 J while that of H4 and H5 laminates are about 25 and 21 J, respectively. At impact energy of 40 J, the absorbed energies have close values again for the orientations. At high impact energies, the absorbed energies of the G1 and H4 laminates with lay up $[90/0/0/90]_s$ are higher than other orientations. This is because of more mismatch effect and the occurrence of greater damage area with fiber brakeage and delamination in G1 and H4 laminate, compared to the G2, G3 and H5, H6 laminates.

If the effect of temperature on the absorbed energy is investigated, at low impact energy levels, at which complete rebounding case takes place, absorbed energy does not significantly change with the varied temperature. However, at intermediate impact energies, for the glass/epoxy and carbon/glass hybrid composites, the absorbed energy increases with increasing temperature from -50 to 90 °C. For example, at impact energy of 30 J, the absorbed impact energy of the G1 laminate is 23, 27 and 29 J at -50, 20 and 90 °C temperature, respectively. This is owing to the increase in ductile behavior with increasing temperature. The result indicated that at intermediate energy levels at which the partial rebound takes place, bending stiffness of the glass/epoxy and glass/carbon hybrid is a leading factor in the amount of absorbed energy. The results for only carbon/epoxy composites are more complex because of its brittle structure. At high impact energy levels, absorbed energy increases in glass/epoxy and carbon/glass hybrid composites while decreasing in carbon/epoxy composites with the increased temperature from -50 to 90 °C. As indicated earlier, at high velocities, shear-out failure mode rather than delamination takes place in carbon/epoxy composites. Since carbon fibers behave more brittle with decreasing temperature from 90 to -50 °C, for high impact energies, the absorbed energy, i. e, perforation threshold decreases. However, the opposite of this result was obtained for glass/epoxy and glass/carbon hybrid composites. This is probably attributed to the increase in thermal residual stresses with decreasing temperature. Also, at high velocities, the occurrence of delamination rather than shear out failure

mode in glass/epoxy and glass/carbon hybrid composites plays a governing role in energy absorption. High thermal stresses at low temperature lead to greater delamination and higher energy absorption for high impact energies. As a result, with decreasing temperature, perforation threshold decreases for carbon/epoxy composites while increasing for glass/epoxy and glass/carbon hybrid composites.

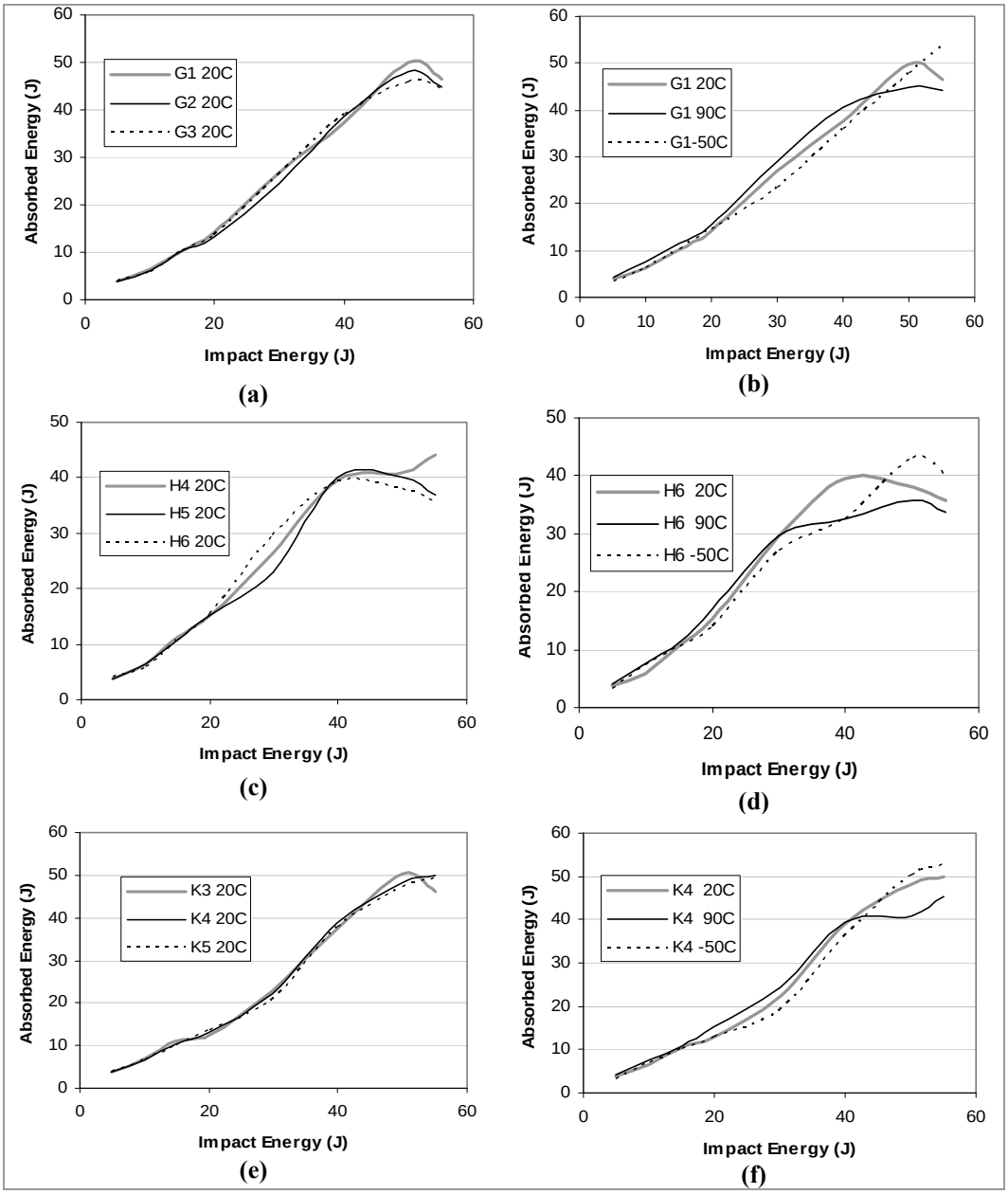

Figure 6.19 Energy profile diagrams for each of specimen type and temperature

As a result of comparisons of the carbon/glass hybrid composites with symmetric and antisymmetric orientations, it is seen from Figure 6.20.b that the K6 and K7

laminates with lay ups $[G_{90}/G_0/C_0/C_{90}]_s$ and $[C_{90}/C_0/G_{90}/G_0]_{as}$, respectively have very similar energy profile diagrams at room temperature. The only difference is that at intermediate energies, the absorbed energy of K7 laminate is higher than that of K6 laminate.

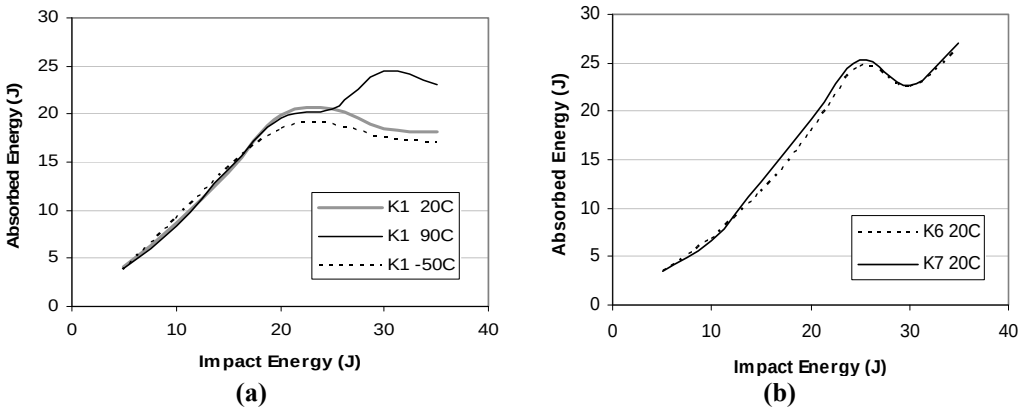

Figure 6.20 Energy profile diagrams for each of specimen type and temperature

When variation of the maximum contact force with impact energy at room temperature is investigated, it is seen that while impact energy increases, maximum contact force increases and it converges a constant value. Figure 6.21.a shows that K3 laminate has the highest contact force because of present of carbon woven fabric fiber in outer layers. The K3, K4 and K5 woven carbon-outside/unidirectional glass-inside clustered laminates provide both high impact resistance and carry the highest loading, compared to the other laminates. From the result, it was concluded that there can be tremendous advantage to be had by hybridizing the laminates. Especially for aerospace structures that are mostly made using carbon/epoxy composites, it is worth to include woven fabric layers at the top and bottom surface. Woven fabric layers at the top delay the penetration of the indentor while the layers at the bottom prevent the splitting damage which is the main cause for the initiation of widespread delamination damage.

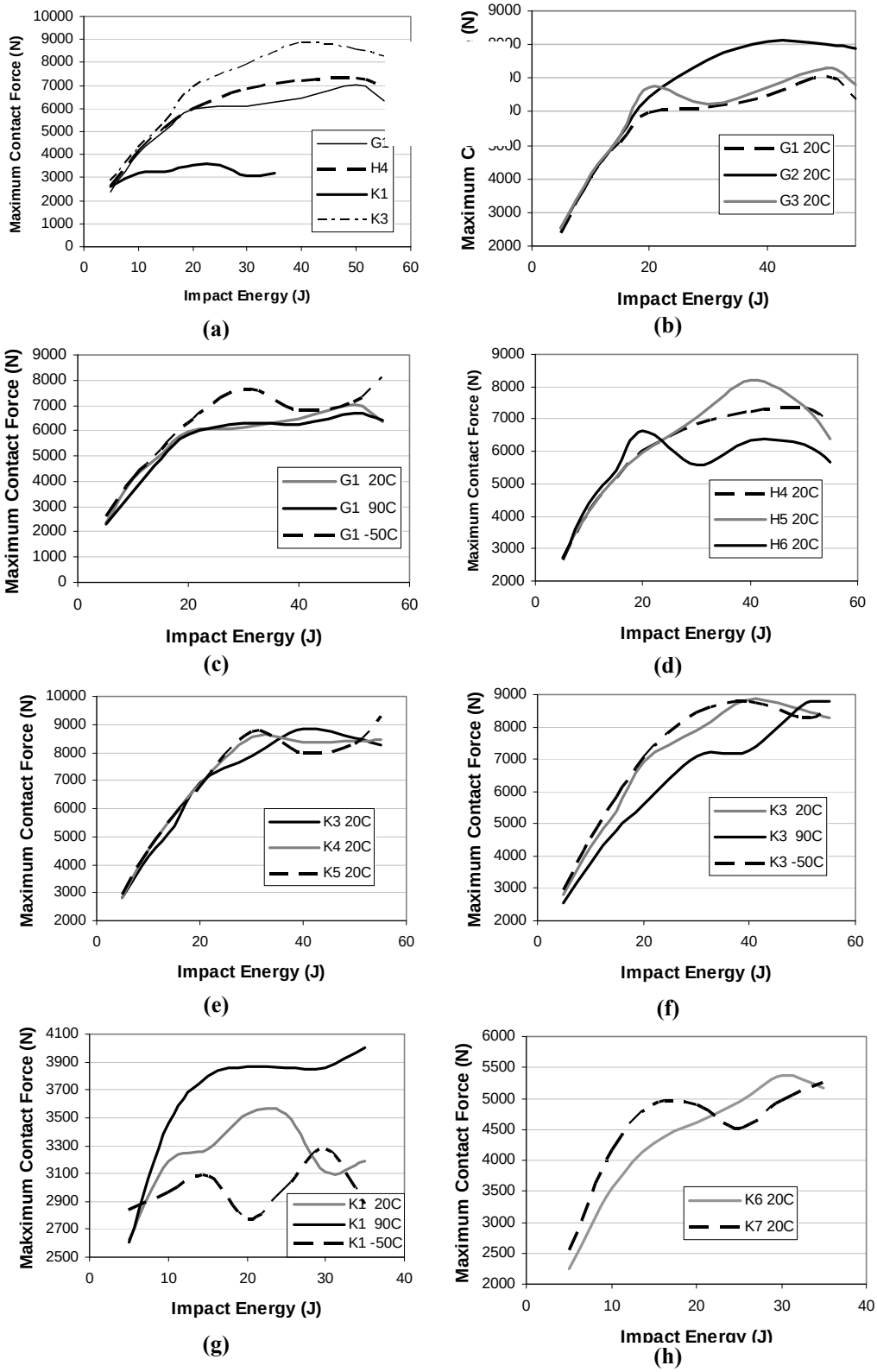

Figure 6.21 Maximum contact Force versus impact energy curves for each of specimen type and temperature

For impact energy of 5 J, the value of maximum force of the G1, H4, K1 and K3 laminates are likely the same, approximately 2.5 kN. While the impact energy increases, the value of maximum force of the G1, H4, K1 and K3 laminates reach 7, 7.2, 3.5 and 9 kN, respectively. The result point outs that the highest values of maximum contact force in the laminates are related to the energy required for first damage, namely the initial energy. For instance, initial energy value of K1 laminate is 4.3, while that of the K3 laminate is 25.3 J. Therefore, as a result, it is indicated that for intermediate and high impact energies, maximum contact force of a laminate is dependent on its initial energy rather than stiffness. The same result can be also drawn for the G1, G2 and G3 laminates. The result of a quasi-static analysis in ANSYS software shows that G3 laminate has the highest bending stiffness compared to the G1 and G2 laminates. Nevertheless, maximum contact force of G2 laminate has higher value in comparison with the G1 and G3 laminate. It is clearly seen that initial energy of G2 laminate is also higher than the G1 and G3 laminates. When the variation of contact force with temperature is investigated for the same impact energy, the results can not be clearly obtained. The reason is probably that with decreasing temperature, the decrease at the initial energy and in contact force resulting from increasing in thermal residual stress compensates the increasing contact force with increase in bending stiffness.

6.3.2.6 Measurement of Damage Areas

Thanks to the optically transparent nature of glass/epoxy composites, the impacted samples were visually inspected and photographs of them were taken by using a strong backlighting. Each overall damage areas were contoured and obtained by using AutoCAD software.

Variation of the overall damage area values with impact energy and temperature are shown in Figure 6.22. It is seen from the figures that damage area increases while impact energy increases for the same temperature and orientation. If damage area is compared in terms of orientations of the laminates for the same impact energy and temperature, in general, it is seen that damage area of G1 laminate is greater than that

of G2 and G3 laminates because of more mismatching effect. When variation of damage area with temperature is investigated for the same orientation, different results are obtained for low and high impact energies. At low impact energies (up to 15 J), as damage area is small and matrix cracks take place only, a correlation between damage area and temperature could not be determined. However, for intermediate and high impact energies (from 20 J to 55 J) at which delamination and fiber breakage as well matrix cracks take place, damage area increases while the temperature is decreasing from 90 °C to -50 °C. This is because embrittlement of the polymeric matrix, together with the interlaminar thermal stresses generated in the laminate at low temperature, contributes to facilitate the generation and propagation of damage when subjected to impact loads. Variation of damage area on back side of G1 laminate with temperature at impact energy of 55 J is shown in Figure 6.25.

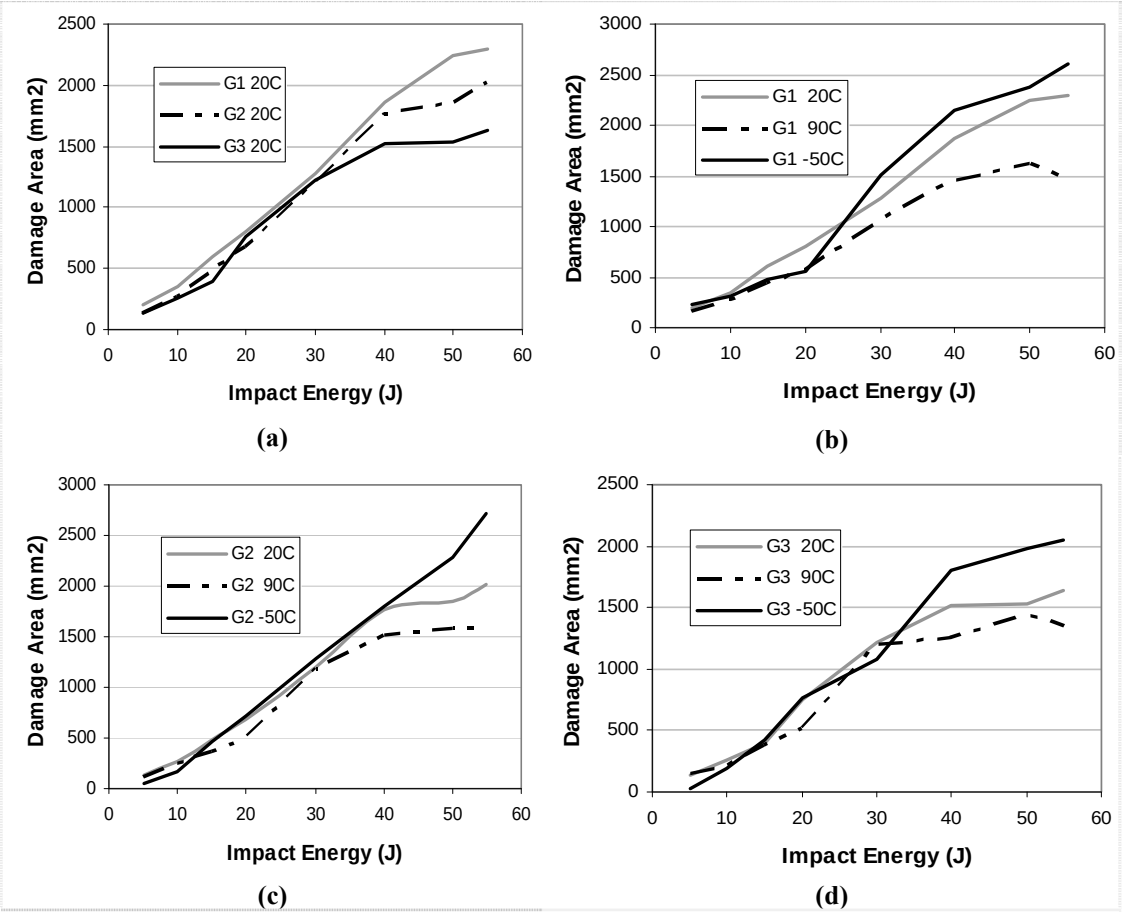

Figure 6.22 Damage areas of Glass/epoxy laminates under impact energies ranging 5 J to 55 J

6.3.2.7 Damage Modes

The impact damage modes in the specimens consist of a very complex process. It is a combination of matrix cracking, delamination, surface buckling, fiber shear-out, and fiber fracture, etc., which usually all act together. The delamination induced by the mismatching of the bending stiffness was propagated and aligned along the direction of the fibers. The damage zone includes a centrally depressed cone, surface buckling, matrix cracking, delamination, and fiber failure. Matrix cracks, in the form of shear failure mode, propagated radially from the top down, which inclined about $\pm 45^{\circ}$ out of the vertical position, and interconnected with the delamination damage proceeded with the ascending impacted force and fabric lamina was penetrated layer by layer.

A nearly undamaged conical zone just under the centrally depressed cone was observed in the non-penetrated cases, located inside the inclined matrix cracks. Fiber failure occurred at the indentation central line. Shear cracks showed up away from the indentation central line, but tensile cracks were located around the indentation central line. This indicates that the impact damage in the bottom layers is attributed to the bending stresses.

In perforated cases, failure modes for the specimens were observed as fiber shear-out and fiber breakage, tensile fiber failure and delamination. For high impact energies, fiber shear-out damage take places much more in carbon/epoxy laminates and damage propagate on smaller zone than glass/epoxy laminates. In addition, damage area increases with decreasing temperature in perforated cases for all specimens. However, damage area of glass/epoxy laminates is greater than carbon/epoxy laminates for high impact energies. The photographs of the specimens subjected to intermediate and high impact energies are given in Figures 6.23-26.

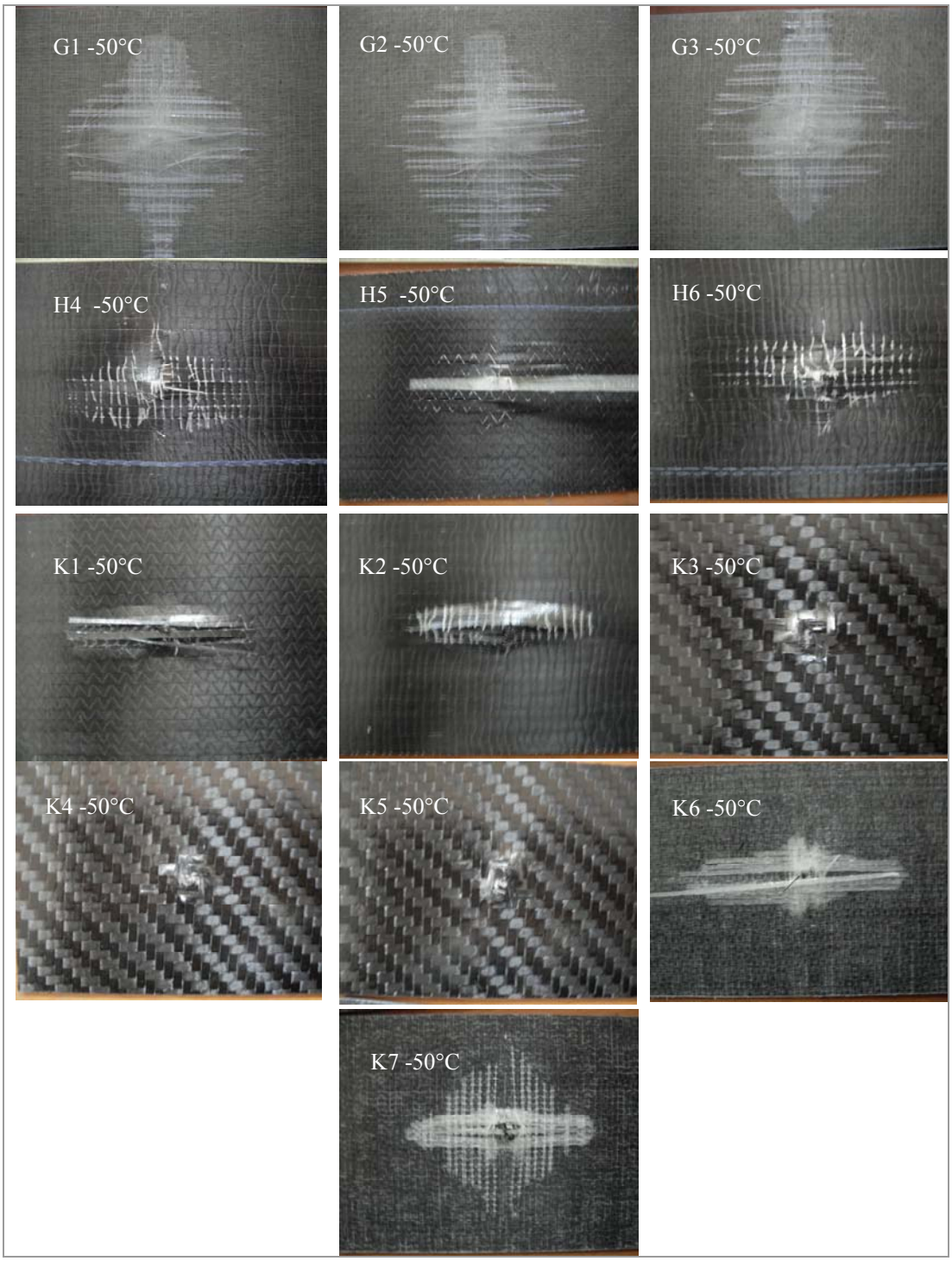

Figure 6.23 Photographs of the back surfaces of specimens subjected to high impact energies and -50 °C temperature

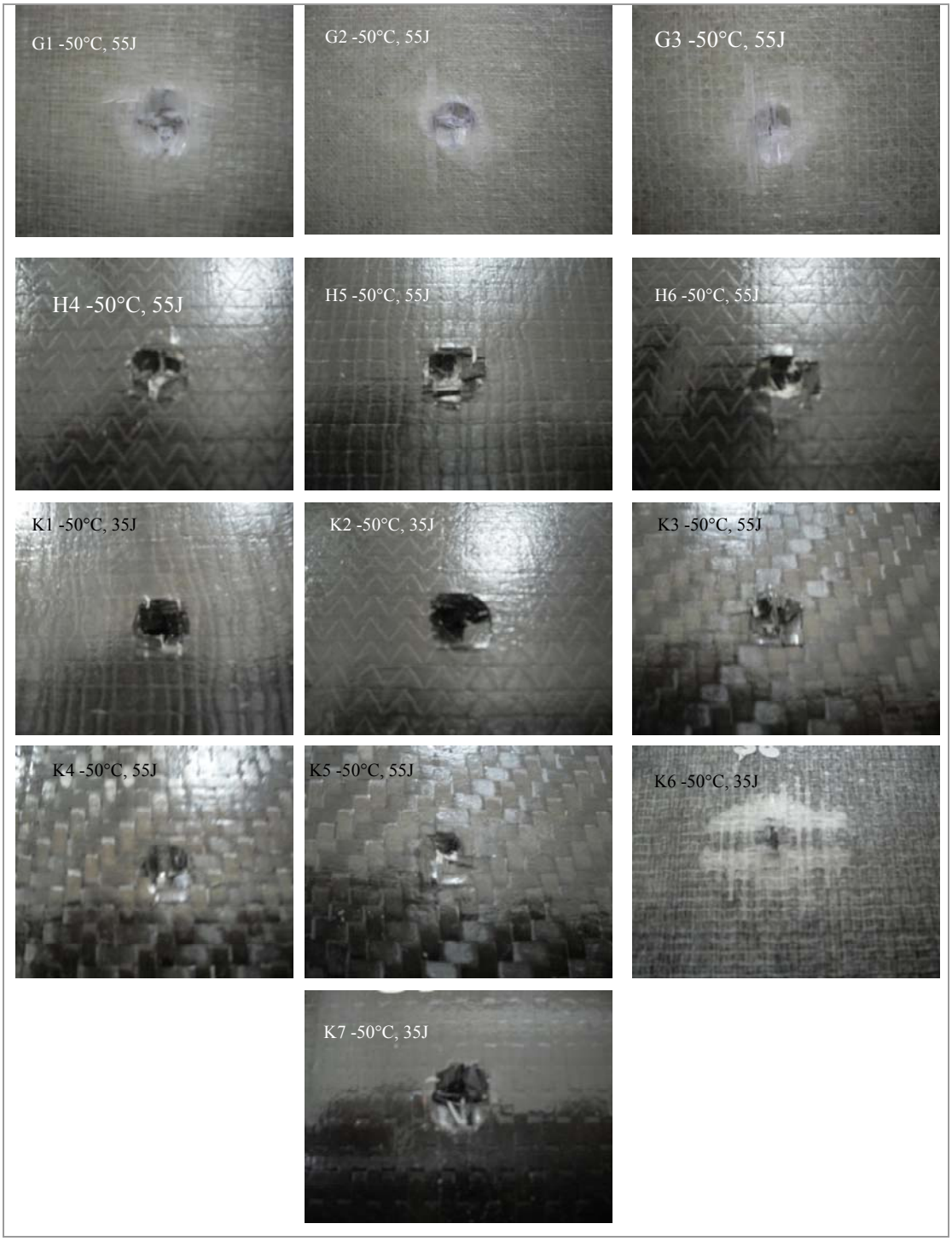

Figure 6.24 Photographs of impacted sides of impacted specimens subjected to high impact energies and -50 °C temperature

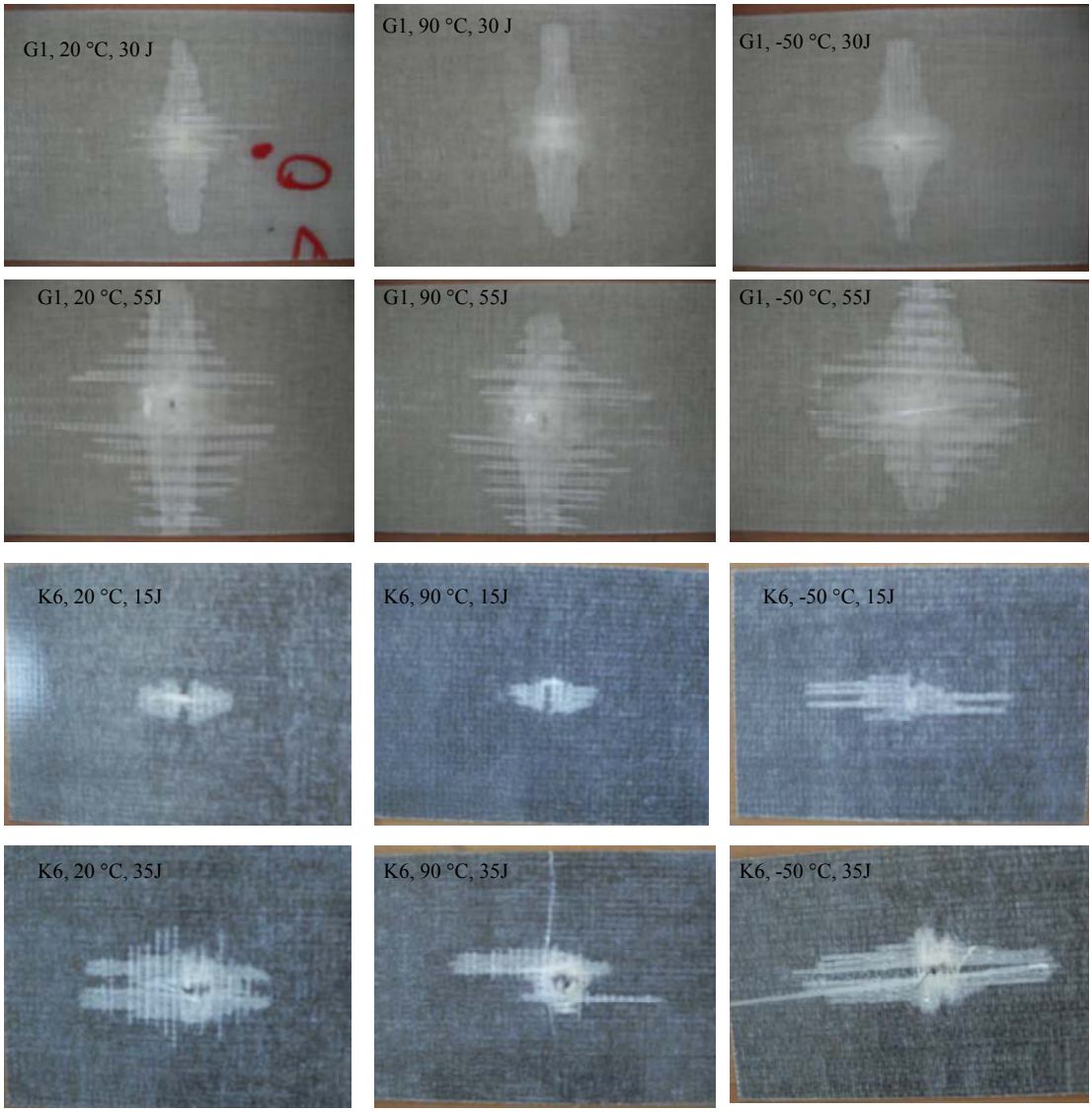

Figure 6.25 Variation of damage areas in specimens with temperature at intermediate and high impact energies

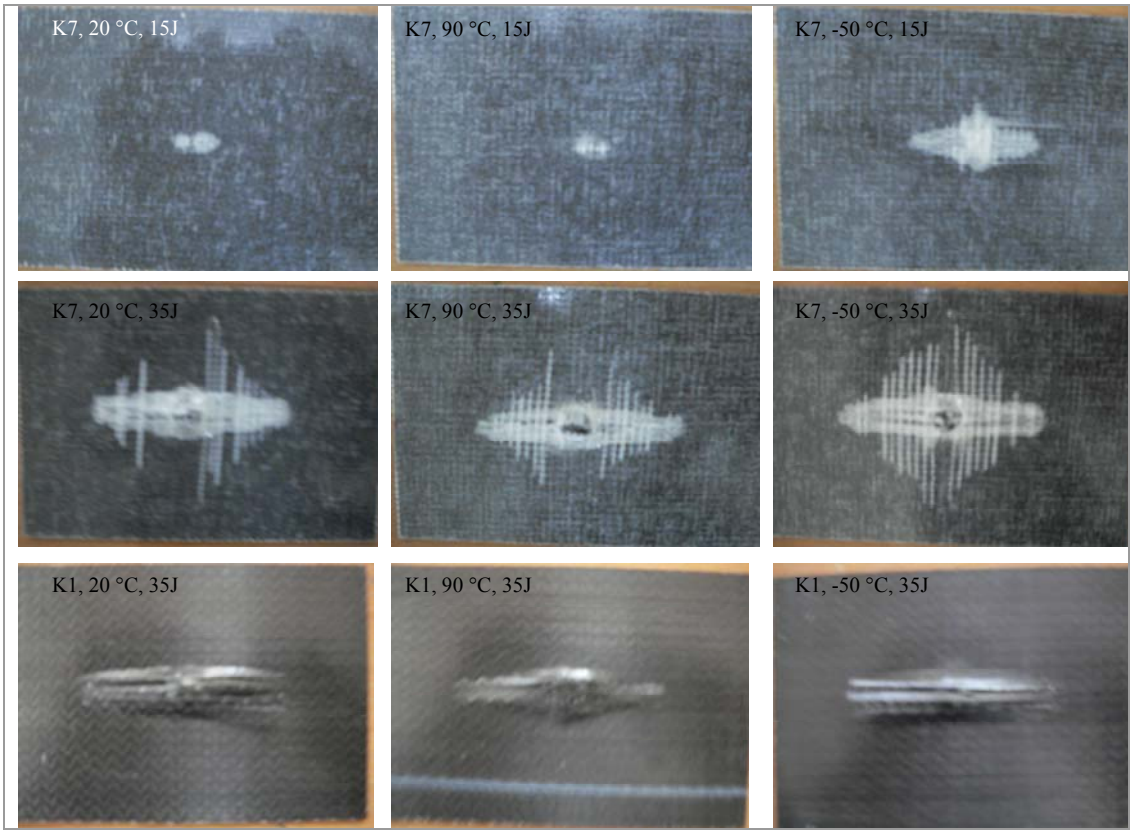

Figure 6.26 Variation of damage areas in specimens with temperature at intermediate and high impact energies

6.3.3 Impact Test Results of the Saturated Laminates

Some of G1, G2, G3, H4, H5, H6, K1, K2, K3, K4 and K5 samples were aged in glass cabin for 7 months, under 20°C sea water immersion condition The specimens were taken out of the cabin after 7 months and impact tests were performed at 20 and -50 °C temperatures at low, intermediate and high impact energy levels: 5, 15, 35 J for K1, K2 carbon/epoxy composites; 5, 30, 55 J for G1, G2, G3 glass/epoxy, H4, H5, H6, K3, K4 and K5 glass/carbon hybrid composites.

The specific energy values are given in Table 6.3. Generally, the results show that perforation energy thresholds of the laminates are not significantly changed following seawater immersion. The reason of this is probably that the specimens were kept in cabin without subjecting pre-stress and high temperature. Also, In general, fibers do not absorb moisture and therefore any change in material property due to moisture would only occur in the matrix (Woldesenbet, Gupta & Vinson,

2004) Since, the properties in the longitudinal direction are dominated by the fibers, the variation in properties between saturated and dry samples are not significant compared to the properties in the transverse and thickness directions. At high impact energies, in case of perforation, fiber breakage and delamination have dominant effects on absorbed energy. Therefore, the effects of sea water immersion on perforation energy are expected to be very little.

Perforation energy decreases slightly for G1, H4, K1 and K3 laminates with a lay up $[90/0/0/90]_s$ while it increases for G2, H5 samples following seawater immersion. In addition, with decreasing temperature from 20 to -50 °C, perforation energies of the laminates increases except for K1 and K2 carbon/epoxy laminates. Effects of temperature on perforation threshold of the saturated specimens are similar to that of dry specimens.

Table 6.3 Comparisons of the specific energy values

Sea Water Immersion				**Dry**			
Specimen Type and Temperature	**Initiation Energy (J)**	**Total Absorbed Energy (J)**	**Propagation Energy (J)**	**Specimen Type and Temperature**	**Initiation Energy (J)**	**Total Absorbed Energy (J)**	**Propagation Energy (J)**
TS G1 20C	17.62	45.64	28.02	**G1 20C**	16.30	46.46	30.16
TS G2 20C	20.01	47.42	27.41	**G2 20C**	27.62	44.80	17.18
TS G3 20C	18.33	42.18	23.85	**G3 20C**	18.55	44.50	25.95
TS H4 20C	13.51	42.33	28.81	**H4 20C**	14.40	44.01	29.61
TS H5 20C	21.49	41.77	20.27	**H5 20C**	19.48	37.07	17.59
TS H6 20C	15.86	35.48	19.62	**H6 20C**	15.61	35.74	20.13
TS K1 20C	4.69	18.14	13.45	**K1 20C**	4.36	18.18	13.82
TS K2 20C	7.70	18.92	11.22	**K2 20C**	6.64	19.96	13.32
TS K3 20C	20.16	47.91	27.75	**K3 20C**	21.59	50.37	28.78
TS K4 20C	21.30	48.43	27.13	**K4 20C**	22.07	49.93	27.86
TS K5 20C	20.23	49.39	29.16	**K5 20C**	28.09	49.34	21.25
TS G1 -50C	16.28	51.93	35.65	**G1 -50C**	15.18	53.86	38.68
TS G2 -50C	17.70	49.89	32.19	**G2 -50C**	21.34	50.32	28.98
TS G3 -50C	17.03	49.69	32.65	**G3 -50C**	17.43	54.05	36.62
TS H4 -50C	13.53	45.60	32.07	**H4 -50C**	13.75	47.12	33.37
TS H5 -50C	21.87	45.13	23.26	**H5 -50C**	19.97	40.41	20.44
TS H6 -50C	13.00	43.10	30.10	**H6 -50C**	13.58	42.54	28.96
TS K1 -50C	5.28	16.49	11.21	**K1 -50C**	4.11	17.05	12.94
TS K2 -50C	6.27	16.97	10.70	**K2 -50C**	6.14	18.15	12.01
TS K3 -50C	24.62	49.62	25.00	**K3 -50C**	22.33	53.84	31.51
TS K4 -50C	23.45	52.52	29.08	**K4 -50C**	20.15	52.73	32.58
TS K5 -50C	23.88	53.49	29.61	**K5 -50C**	18.57	51.48	32.91

It is known that plasticization of the matrix occurs as a result of absorbed moisture (Karasek, Strait & Amateau, 1995). Water molecules absorbed into the polymer network cause an increase in free volume which leads to an increase in ductility. The increased ductility of the matrix allows higher strains to be accommodated prior to cracking and delamination. If the strength of the matrix and fiber/matrix interface are not reduced significantly, the increase in matrix ductility also results in an increase in the energy required for incipient damage. Therefore, the increase at initial energies of G1, H5, H6, K1, K2 specimens after sea water immersion were observed. However, initial energies of G2 and K5 specimens with lay ups [90/0/45/45] and [KÖ/C_0/C_{45}/C_{45}]$_s$, respectively, decrease after sea water immersion. In the G2 and K5 laminates, since there are more +45° oriented glass fibers at inner layers, the decrease in the strength of the matrix following sea water immersion may induce the reduction of initial energy.

Load-deflection curves at intermediate and high impact energy levels for both dry and saturated samples are shown in Figure 6.27. The curves are almost identical for both conditions. The initial slope of load–deflection curves for dry and saturated samples indicates that the stiffness of the samples remained almost unchanged following water immersion.

Impact damage area was slightly less extensive in saturated samples, which is suggested to be the result of the propagation of interfacial damage present in saturated samples prior to impact, which absorbed impact energy and inhibited the delamination formation. The front and back faces of the impacted specimens for both dry and saturated conditions are shown in Figure 6.28-29.

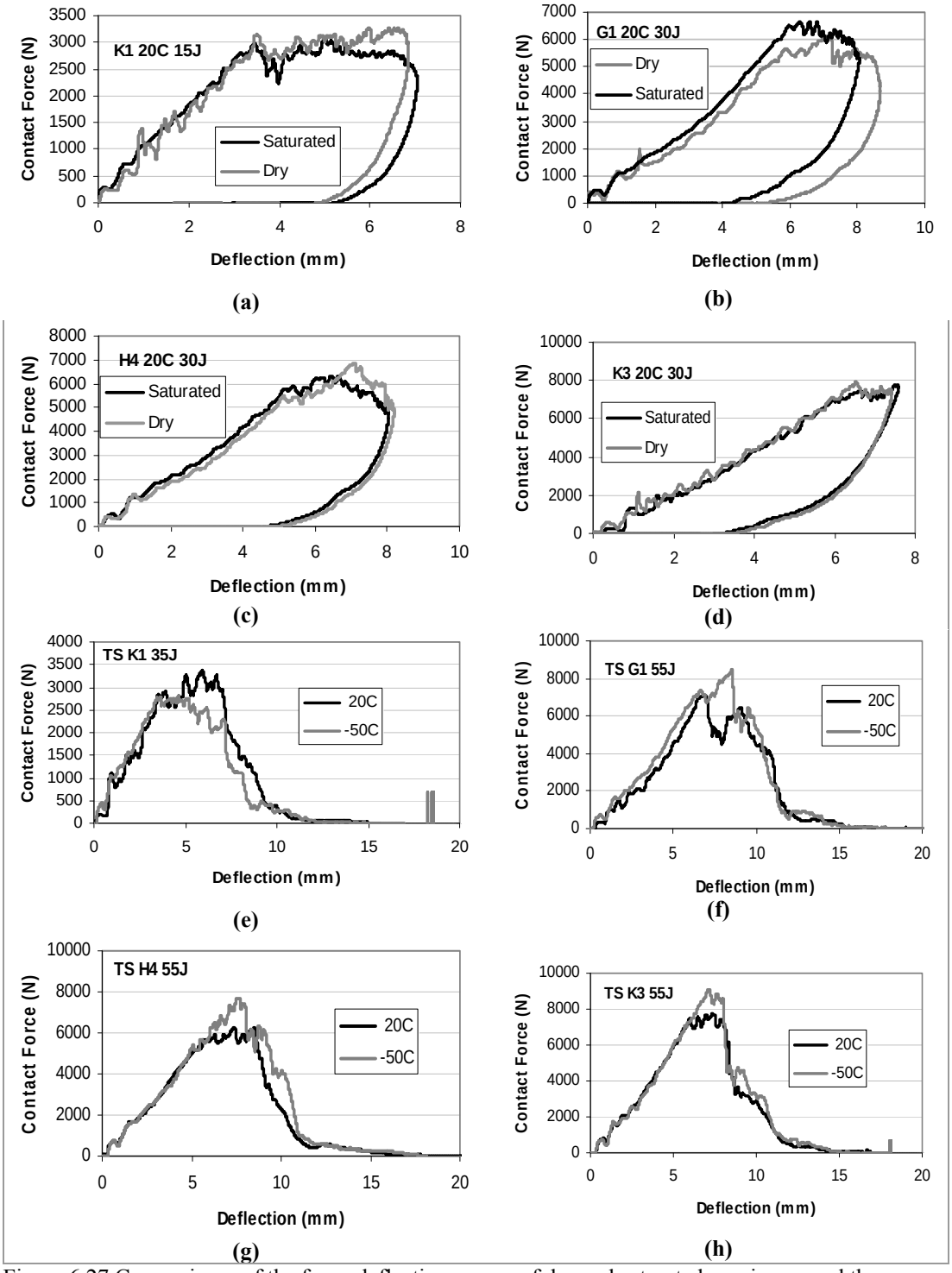

Figure 6.27 Comparisons of the force-deflection curves of dry and saturated specimens and the variation of the curves with temperature in the saturated laminates

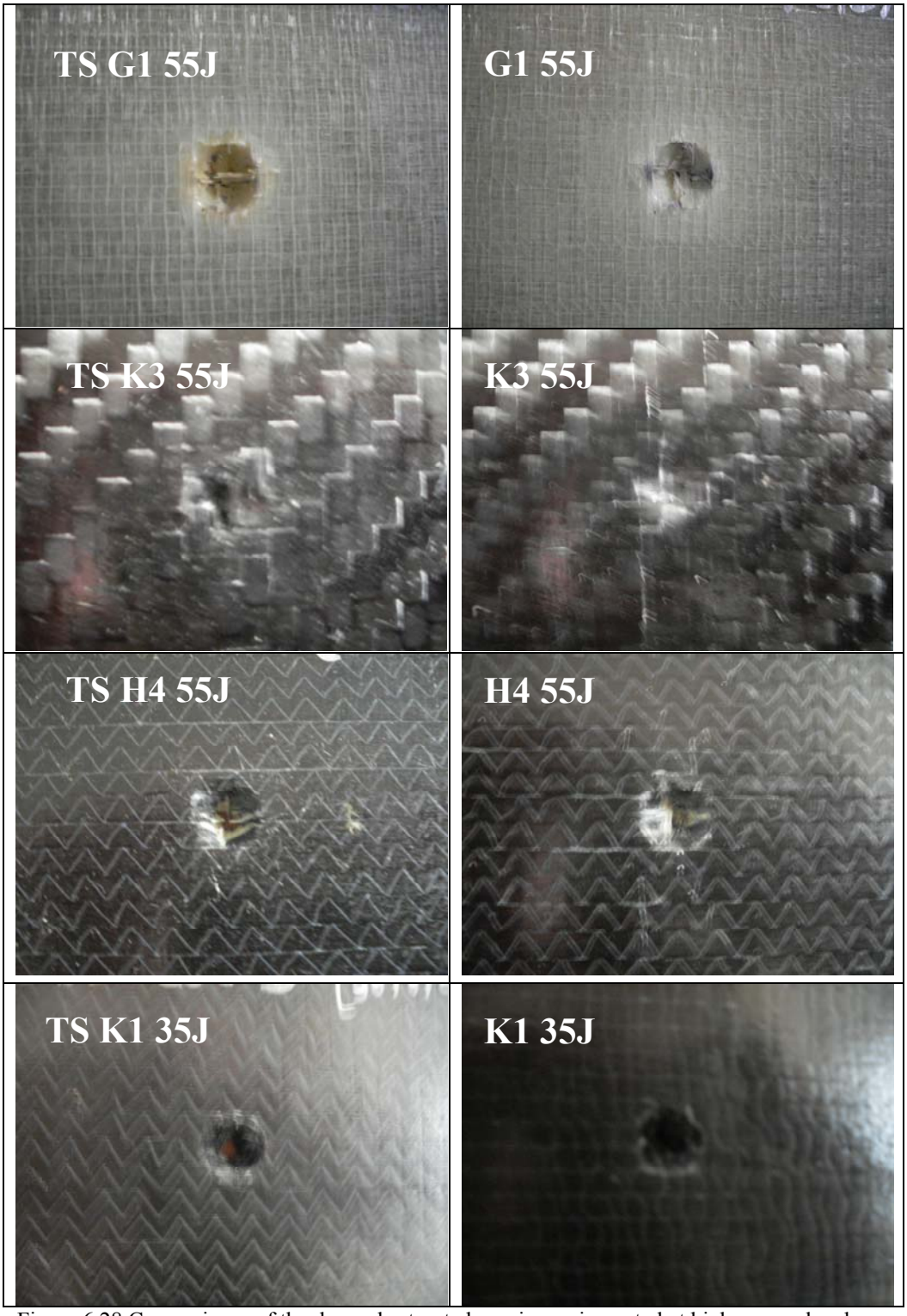

Figure 6.28 Comparisons of the dry and saturated specimens impacted at high energy level (Front Surface)

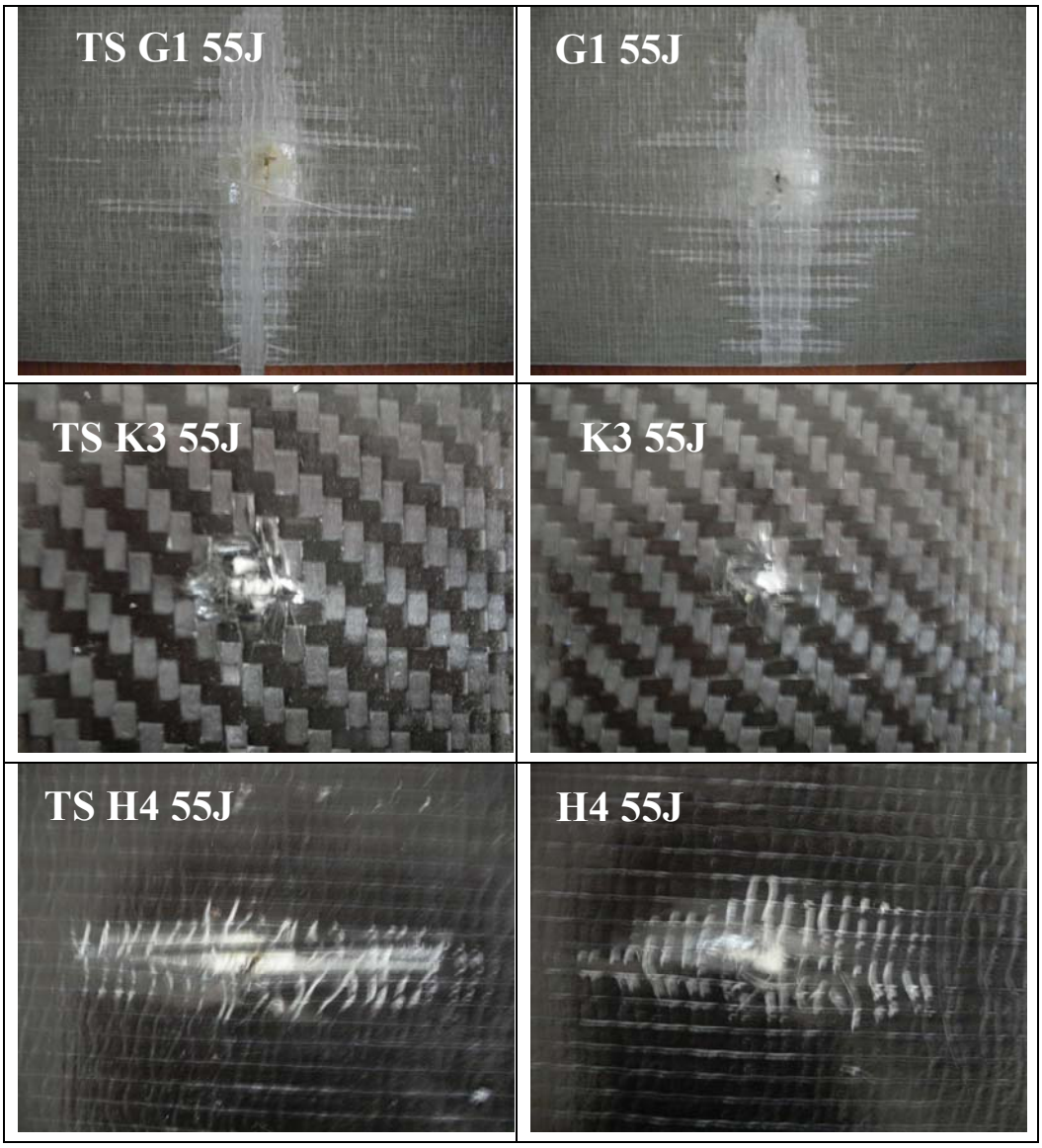

Figure 6.29 Comparisons of the dry and saturated specimens impacted at high energy level (Back Surface)

6.3.4 Comparisons of the impact parameters of the unidirectional laminated composites

Impact responses of the composite specimens were characterized in terms of impact parameters such as permanent deflection, maximum contact force, maximum contact time, energy to maximum contact force, and total energy absorption at low, intermediate, and high impact energy levels. The impact energies were selected as 5, 15, 35 J for the K1, K2, K6 and K7 laminates, 5, 30, 55 J for G1, G2, G3, H4, H5, H6, K3, K4, K5 laminates It can be seen from Tables 6.4-10 that the trends of

absorbed energy versus temperature are different at different impact energy levels. This is because of variation of the damage area and mechanism with changing impact energy level and temperature. For example, at low energy levels, back surface cracking, bending of laminates and plastic deformation of matrix are the most important factors governing energy absorption while at high impact energy (55 J), fiber breakage is the main contributor to energy absorption. When the variation of maximum contact force with temperature and impact energy is investigated for the same orientation, it is seen that with increasing impact energy at the same temperature, the amount of maximum contact force increases up to a constant value. When considering the effect of stacking sequences at 20 °C temperature, maximum contact force has the highest value in G2 laminate at impact energies of 30 and 55 J in spite of its lower bending stiffness than G3 laminate. This is because mismatching effects are lower in G2 laminate compared to G1 and G3 laminates.

At low impact energy of 5 J, a correlation between temperature and permanent deflection could not be determined. However, as indicated earlier, at intermediate impact energy level, at which the partial rebound of the impactor take place, the permanent deflection increases by increasing the temperature for the G1, G2, G3, H4, H5, H6, K3, K4 and K5 laminates except for K1 and K2 specimens. The result is also valid for the saturated specimens at temperatures 20 and -50 °C. For carbon/epoxy composites, a consistent variation of permanent deflection with temperature could not be observed. This is probably owing to high brittle structure of carbon fibers.

At high impact energy levels, although a clear correlation between the initial energy and temperature were established, a clear relation between the energy corresponding to maximum contact force and temperature could not be obtained. This is because the composite failure process is initiated before contact force reaches maximum value.

Table 6.4 The impact parameters of dry specimens at impact energy of 5 J

Nomenclature and Temperature (°C)	Permanent Deflection (mm)	Peak Time (ms)	Max. Force (N)	Max. Deformation (mm)	Energy to Max. Force (J)	Total Time (ms)	Absorbed Energy (J)
G1_20	2.32	3.31	2341	3.46	4.77	7.30	4.17
G2_20	2.06	3.09	2553	3.34	4.65	7.10	3.85
G3_20	2.12	3.32	2526	3.46	4.84	7.17	3.87
H4_20	2.27	3.42	2592	3.63	4.87	7.22	3.87
H5_20	2.15	3.34	2660	3.47	4.92	6.94	3.87
H6_20	2.06	3.30	2679	3.38	4.95	6.81	3.87
K1_20	2.05	3.07	2659	3.30	4.69	6.98	3.95
K2_20	2.27	3.42	2592	3.63	4.87	7.22	3.87
K3_20	2.17	3.07	2876	3.35	4.78	6.49	3.78
K4_20	2.27	3.20	2806	3.40	4.87	6.53	3.94
K5_20	2.09	3.18	2937	3.39	4.92	6.47	3.70
K6_20	1.25	3.80	2551	3.59	4.99	8.90	3.70
K7_20	1.52	3.49	2506	3.46	4.91	7.77	3.52
G1_90	2.23	2.98	2377	3.23	4.51	7.14	4.15
G2_90	1.98	3.42	2482	3.53	4.87	7.54	3.82
G3_90	1.93	3.42	2493	3.52	4.88	7.53	3.75
H4_90	2.17	3.07	2460	3.29	4.63	7.17	4.14
H5_90	2.25	3.36	2665	3.60	4.83	7.15	3.85
H6_90	2.38	3.58	2631	3.66	5.02	7.01	3.99
K1_90	2.11	3.07	2584	3.28	4.68	7.00	4.04
K2_90	2.05	2.94	2696	3.17	4.64	6.75	4.01
K3_90	2.69	3.36	2548	3.62	4.79	6.92	4.27
K4_90	2.50	3.09	2718	3.40	4.67	6.57	4.18
K5_90	2.36	3.08	2701	3.40	4.64	6.74	4.02
K6_90	1.74	3.30	2086	3.39	4.63	8.86	4.19
K7_90	1.60	3.28	2350	3.36	4.79	8.09	3.94
G1_-50	2.02	3.76	2602	3.90	4.90	7.76	3.28
G2_-50	2.12	3.53	2604	3.73	4.89	7.37	3.45
G3_-50	2.13	3.53	2601	3.83	4.77	7.63	3.40
H4_-50	1.68	3.05	2786	3.40	4.59	15.75	2.71
H5_-50	1.77	3.53	2934	3.58	5.02	6.97	3.09
H6_-50	2.23	3.31	2781	3.65	4.75	7.09	3.62
K1_-50	2.27	4.32	2730	3.87	5.04	7.50	3.73
K2_-50	2.02	3.18	2839	3.54	4.47	7.29	3.43
K3_-50	2.05	3.04	2948	3.35	4.73	6.55	3.56
K4_-50	1.81	3.02	3112	3.27	4.75	6.43	3.26
K5_-50	1.98	3.04	3027	3.31	4.69	6.46	3.38
K6_-50	1.41	3.51	2282	3.52	4.84	8.57	3.71
K7_-50	1.97	3.96	2567	4.07	4.96	8.20	3.30

Table 6.5 The impact parameters of the saturated specimens at impact energy of 5 J

Nomenclature and Temperature (°C)	Permanent Deflection (mm)	Peak Time (ms)	Max. Force (N)	Max. Deformation (mm)	Energy to Max. Force (J)	Total Time (ms)	Absorbed Energy (J)
TS_G1_20	1.88	3.31	2472	3.40	4.79	7.34	3.71
TS_G2_20	1.66	3.30	2619	3.36	4.86	7.16	3.36
TS_G3_20	1.63	3.29	2615	3.35	4.86	7.16	3.33
TS_H4_20	1.75	3.17	2760	3.29	4.83	6.80	3.45
TS_H5_20	1.81	3.12	2761	3.26	4.80	6.75	3.56
TS_H6_20	1.66	3.13	2832	3.26	4.84	6.74	3.35
TS_K1_20	1.72	3.37	2724	3.40	4.93	7.05	3.43
TS_K2_20	1.64	3.14	2802	3.26	4.81	6.90	3.43
TS_K3_20	1.83	3.03	2818	3.18	4.79	6.47	3.57
TS_K4_20	1.77	3.01	2897	3.19	4.76	6.50	3.45
TS_K5_20	1.80	3.10	2863	3.22	4.88	6.50	3.51
TS_G1_-50	1.58	3.75	2666	3.39	4.91	7.34	3.34
TS_G2_-50	1.54	3.33	2619	3.35	4.92	7.18	3.26
TS_G3_-50	1.71	3.26	2577	3.36	4.82	7.21	3.45
TS_H4_-50	1.88	2.96	2677	3.21	4.59	6.81	3.62
TS_H5_-50	1.74	3.19	2748	3.28	4.87	6.79	3.45
TS_H6_-50	1.60	3.34	2740	3.34	4.96	6.95	3.30
TS_K1_-50	1.91	3.30	2608	3.41	4.81	7.24	3.77
TS_K2_-50	1.75	3.11	2672	3.33	4.66	7.25	3.60
TS_K3_-50	1.78	3.02	2962	3.15	4.85	6.31	3.49
TS_K4_-50	1.54	3.33	3275	3.23	4.99	6.56	3.15
TS_K5_-50	1.75	3.40	3171	3.31	5.02	6.65	3.42

Table 6.6 The impact parameters of dry and saturated specimens at intermediate impact energy of 15 J

Nomenclature and Temperature (°C)	Permanent Deflection (mm)	Peak Time (ms)	Max. Force (N)	Max. Deformation (mm)	Energy to Max. Force (J)	Total Time (ms)	Absorbed Energy (J)
K1_20	5.53	2.66	3229	5.14	10.06	8.41	14.26
K2_20	5.60	1.74	3655	3.86	7.40	8.72	14.61
K6_20	2.46	3.13	4313	5.76	13.48	8.26	11.32
K7_20	3.43	2.90	4918	5.66	12.69	7.64	11.88
K1_90	5.03	2.02	3713	4.40	8.59	7.94	14.23
K2_90	4.93	2.21	4508	4.63	10.38	7.70	14.37
K6_90	4.24	3.26	3773	6.44	12.37	9.44	12.74
K7_90	3.22	3.11	4564	5.89	13.54	7.63	11.66
K1_-50	5.38	2.01	3037	4.40	7.90	9.11	14.29
K2_-50	4.95	2.39	3413	4.85	10.04	8.38	14.18
K6_-50	3.73	4.03	4442	7.37	14.71	8.62	11.09
K7_-50	4.52	2.79	4667	5.75	11.70	8.56	13.39
TS_K1_20	5.85	1.91	3050	4.16	7.40	9.28	14.66
TS_K2_20	5.32	1.72	3652	3.84	7.36	9.05	14.32
TS_K1_-50	4.42	3.07	3396	5.77	12.66	8.59	13.66
TS_K2_-50	7.78	1.49	2988	3.40	5.46	11.50	15.03

Table 6.7 The impact parameters of dry and saturated specimens at intermediate impact energy of 30 J

Nomenclature and Temperature (°C)	Permanent Deflection (mm)	Peak Time (ms)	Max. Force (N)	Max. Deformation (mm)	Energy to Max. Force (J)	Total Time (ms)	Absorbed Energy (J)
G1_20	5.41	2.19	6104	6.61	19.60	7.72	26.53
G2_20	4.64	2.45	7415	6.97	23.87	7.00	25.20
G3_20	5.19	1.93	6334	5.97	17.51	7.29	26.26
H4_20	5.20	2.44	6816	6.98	23.44	7.16	26.40
H5_20	3.87	2.84	7135	7.37	27.82	6.71	22.98
H6_20	6.53	1.89	5910	5.88	17.00	8.18	28.01
K3_20	3.65	2.32	8008	6.53	24.69	6.26	22.90
K4_20	3.92	2.29	8313	6.39	25.13	6.27	24.10
K5_20	3.46	2.36	8412	6.54	25.77	6.15	22.31
G1_90	6.66	2.24	6365	6.69	20.59	8.03	28.65
G2_90	5.79	2.33	7140	6.78	22.39	7.68	27.86
G3_90	6.96	1.86	6304	5.82	16.50	8.26	28.97
H4_90	5.69	2.33	6338	6.77	22.07	7.21	27.38
H5_90	6.73	2.28	6367	6.62	22.35	7.80	29.21
H6_90	7.88	1.74	5947	5.49	15.43	8.71	29.83
K3_90	4.89	2.66	7070	7.18	26.27	6.64	25.86
K4_90	4.02	2.31	8067	6.43	24.96	6.13	24.44
K5_90	4.23	2.45	8080	6.80	26.08	6.26	24.37
G1_-50	4.00	2.96	7244	7.49	28.52	6.80	23.70
G2_-50	2.78	3.01	8768	7.29	29.91	6.22	18.97
G3_-50	3.91	2.43	7000	6.60	23.20	6.99	23.87
H4_-50	4.68	2.37	7155	6.90	22.73	6.80	24.34
H5_-50	5.36	2.51	7296	7.10	24.69	7.35	27.01
H6_-50	4.40	2.16	7254	6.40	21.26	6.90	24.66
K3_-50	3.38	2.86	8427	7.27	29.03	6.19	20.81
K4_-50	2.92	2.81	9059	6.86	29.83	5.72	19.21
K5_-50	3.35	2.83	8382	7.18	28.92	6.12	20.57
TS_G1_20	4.91	2.19	6625	6.54	20.85	7.46	26.01
TS_G2_20	3.64	2.80	7491	7.42	27.66	7.09	23.15
TS_G3_20	5.01	1.88	6483	5.85	17.13	7.51	26.10
TS_H4_20	5.04	2.56	6270	7.04	24.62	7.66	26.78
TS_H5_20	5.19	2.59	7189	7.07	25.91	7.20	27.26
TS_H6_20	6.08	2.02	6182	6.16	18.80	8.52	28.18
TS_K3_20	3.50	3.27	7641	7.61	30.19	6.47	21.27
TS_K4_20	4.19	2.10	7872	6.20	22.06	6.65	25.09
TS_K5_20	3.46	2.36	8260	6.64	24.90	6.46	22.20
TS_G1_-50	3.70	2.73	7069	7.28	26.14	7.05	22.96
TS_G2_-50	2.74	2.98	8497	7.48	29.37	6.43	18.51
TS_G3_-50	3.72	2.01	7452	6.09	19.57	6.93	23.10
TS_H4_-50	3.91	3.11	7301	7.57	29.39	6.68	23.16
TS_H5_-50	3.76	2.37	7420	6.67	24.28	6.84	23.55
TS_H6_-50	4.04	2.89	6274	7.44	27.64	7.18	23.98
TS_K3_-50	2.76	2.90	8488	7.09	29.41	6.17	19.29
TS_K4_-50	3.00	2.52	8989	6.58	28.08	6.09	21.97
TS_K5_-50	2.67	2.65	8850	6.77	28.20	6.04	19.53

Table 6.8 The impact parameters of dry and saturated specimens at high impact energy of 35 J

Nomenclature and Temperature (°C)	Permanent Deflection (mm)	Peak Time (ms)	Max. Force (N)	Max. Deformation (mm)	Energy to Max. Force (J)	Total Time (ms)	Absorbed Energy (J)
K1_20	12.23	1.14	3192	4.08	7.76	4.02	18.19
K2_20	11.95	0.95	3916	3.47	6.12	3.95	18.84
K6_20	16.36	2.18	4971	7.25	18.81	6.19	24.57
K7_20	15.66	1.49	5071	5.26	11.86	6.71	28.34
K1_90	13.34	1.08	4406	3.90	8.40	4.75	22.03
K6_90	11.43	2.05	4757	6.91	17.80	8.07	30.44
K7_90	14.84	1.95	5457	6.69	16.97	6.94	30.29
K1_-50	12.32	1.40	2874	5.03	9.03	3.94	17.09
K2_-50	12.00	0.98	3237	3.57	6.03	3.91	18.16
K6_-50	13.14	1.87	5125	6.37	16.72	4.97	25.24
K7_-50	13.51	1.20	4385	4.30	8.79	4.79	22.20
TS_K1_20	13.66	1.59	3286	5.63	10.61	4.50	18.16
TS_K2_20	12.66	1.17	3946	4.26	7.70	4.19	18.91
TS_K1_-50	13.45	1.20	2835	4.34	7.43	4.32	16.49
TS_K2_-50	13.67	1.00	3182	3.66	6.02	4.43	16.96

Table 6.9 The impact parameters of dry specimens at high impact energy of 55 J

Nomenclature and Temperature (°C)	Permanent Deflection (mm)	Peak Time (ms)	Max. Force (N)	Max. Deformation (mm)	Energy to Max. Force (J)	Total Time (ms)	Absorbed Energy (J)
G1_20	16.70	1.73	6345	7.63	25.54	5.17	46.92
G2_20	16.11	1.72	7882	7.62	27.70	5.15	44.60
G3_20	17.41	1.35	6968	6.24	18.39	5.44	45.02
H4_20	17.72	1.76	6834	7.76	27.93	5.52	44.07
H5_20	17.00	1.44	6367	6.62	19.55	4.71	37.01
H6_20	15.92	1.12	5669	5.24	12.76	4.32	35.61
K3_20	15.69	1.71	8283	7.49	30.30	4.99	45.98
K4_20	17.68	1.32	8450	6.00	21.66	6.42	49.90
K5_20	16.09	1.58	9258	7.02	28.09	5.56	49.13
G1_90	16.17	1.52	6513	6.89	20.76	4.73	41.63
G2_90	15.07	1.84	7272	8.08	29.24	4.33	41.41
G3_90	16.57	1.38	6388	6.33	18.64	4.78	40.19
H4_90	17.31	1.84	7092	8.05	29.36	5.71	47.22
H5_90	15.49	1.74	6812	7.75	25.99	4.19	35.98
H6_90	15.13	1.24	6301	5.72	15.53	4.01	33.84
K3_90	11.01	1.97	8768	8.37	35.63	9.21	57.76
K4_90	15.09	1.64	7784	7.20	28.60	4.71	45.30
K5_90	17.83	1.75	8569	7.61	32.23	10.54	57.31
G1_-50	19.12	2.02	7894	8.64	34.39	8.26	54.73
G2_-50	15.85	1.55	7882	6.99	23.62	5.14	47.49
G3_-50	15.90	1.83	7587	8.00	30.01	5.80	48.48
H4_-50	15.79	1.55	6676	7.02	22.50	4.98	47.10
H5_-50	14.52	1.64	7149	7.35	24.98	4.07	40.24
H6_-50	16.83	1.21	5924	5.61	15.08	5.02	42.50
K3_-50	17.72	1.60	8507	7.11	28.10	7.54	53.77
K4_-50	18.00	1.60	9215	7.06	29.40	7.39	52.70
K5_-50	16.72	1.90	9300	8.04	36.63	6.32	51.44

Table 6.10 The impact parameters of saturated specimens at high impact energy of 55 J

Nomenclature and Temperature (°C)	Permanent Deflection (mm)	Peak Time (ms)	Max. Force (N)	Max. Deformation (mm)	Energy to Max. Force (J)	Total Time (ms)	Absorbed Energy (J)
TS_G1_20	15.79	1.66	6960	7.48	24.15	4.81	45.62
TS_G2_20	17.25	1.67	7725	7.39	27.54	5.72	47.40
TS_G3_20	15.54	1.33	6751	6.13	17.95	4.53	41.17
TS_H4_20	16.85	1.56	6474	6.98	23.68	5.06	42.13
TS_H5_20	14.62	1.51	7215	6.82	23.09	4.21	41.76
TS_H6_20	14.95	1.35	5944	6.19	18.61	4.01	35.33
TS_K3_20	14.65	1.80	8162	7.73	33.39	4.77	47.81
TS_K4_20	16.20	1.34	8580	6.11	21.00	5.39	47.90
TS_K5_20	15.16	1.73	9421	7.47	33.12	5.63	51.31
TS_G1_-50	17.98	1.99	7911	8.52	34.48	6.85	51.91
TS_G2_-50	16.92	1.74	8784	7.62	30.32	6.17	50.76
TS_G3_-50	17.19	1.60	7241	7.14	25.66	6.07	49.72
TS_H4_-50	16.55	1.81	7314	7.91	29.95	5.26	45.58
TS_H5_-50	14.32	1.82	7801	7.81	31.66	4.56	46.74
TS_H6_-50	15.04	1.46	6861	6.60	22.21	4.49	43.06
TS_K3_-50	14.35	1.68	8950	7.35	30.64	4.78	49.57
TS_K4_-50	16.77	1.39	9215	6.27	24.88	8.29	54.59
TS_K5_-50	16.01	1.79	9539	7.63	34.90	6.85	54.17

6.3.5 Impact Test Results of Woven Glass/Carbon Hybrid Composites

As indicated earlier, the K3, K4 and K5 woven carbon fiber/unidirectional glass fiber hybrid composites provided high impact resistance since the woven carbon fabric layer at the top delay the penetration of the impactor while the woven carbon layer at the bottom prevents the splitting damage and therefore, it was concluded that woven carbon/glass hybrid composites provided higher impact resistance in comparison with unidirectional glass/carbon composites. After this result was obtained, woven carbon fiber /woven glass fiber hybrid composites with eight layers were produced to investigate the effects of stacking sequences and temperature on impact behaviors of woven hybrid composites. In the laminates, the weights of woven carbon fiber and woven glass fiber used as reinforcing materials are 200 and 270 g/m^2, respectively. The stacking sequences were selected as glass-outside/carbon-inside clustered, $[GW/GW/CW/CW]_s$ and glass-inside/carbon-outside clustered, $[CW/CW/GW/GW]_s$, respectively. The nomenclatures of the laminates are W1 and W2, respectively.

Impact tests on the hybrid laminates at 20, 90 and -50 °C temperatures were performed. Impact energies were increased from 3 J to 15 J until perforation take place. By means of the method mentioned before, the perforation, initial and propagation energies were determined.

As shown in Table 6.11, for the same temperature, the perforation energy of the W1 laminate is higher than that of W2 laminate. This is because glass fibers outside of W1 laminate are more effective in dissipating impact energy when compared to carbon fibers outside of W2 laminate. For example, at 20 °C temperature, the propagation energy of W1 laminate is 8.26 J while that of W2 laminate is 5.22 J. Furthermore, it is interesting that for the same temperature, the initiation energy required for first damage of W1 laminate is lower than that of W2 laminate. This reason is that carbon-outside fibers have higher stiffness and strength in comparison with glass-outside fibers. When variation of perforation energy with temperature is investigated, it is seen that the perforation energy increases as temperature decreases. This result is consistent with that of unidirectional hybrid and glass/epoxy composites.

In unidirectional laminates, since initial damage occurs as matrix crack and delamination, thermal stresses contribute to the damage. However, in woven composites, no interlaminar thermally induced stresses appear since the fibers run in both directions and damage increase at low temperature is lower in comparison with unidirectional laminates. Therefore, the variation of the initial energy with temperature in woven laminate is less sensitive when compared to unidirectional laminates. In contrary of unidirectional laminates, the initial energy of woven laminate increase with decreasing temperature. It is thought that this result is associated with higher maximum contact force at lower temperature. Also, as different from unidirectional laminates, the initial energy and the energy corresponding to maximum force are the same values for woven laminates.

Table 6.11. Specific Energy Values for W1 and W2 laminates

Specimen Type and Temperature (°C)	Initiation Energy (J)	Total Absorbed Energy (J)	Propagation Energy (J)
W1 20C	3.96	12.19	8.23
W1 90C	3.93	11.81	7.88
W1 -50C	4.85	13.89	9.04
W2 20C	5.75	10.97	5.22
W2 90C	5.39	10.50	5.11
W2 -50C	5.88	12.10	6.22

Force-deflection curves of woven hybrid laminates at low, intermediate and high impact energies are given in Figure 6.30. The slopes of the curves are associated with their stiffness. Accordingly, since the slope of the curve of W2 laminate is greater than that of W1 laminate, W2 laminate is stiffer than W1 laminate. At low and intermediate impact energies of 3 and 9 J, it is interesting that both the laminates have the identical permanent deflection. As temperature increases from -50 to 90 °C at intermediate impact energy, maximum deflection and permanent deflection of both the laminates increase. Also, it is evident that in case of partial rebounding and perforation after contact force reach maximum value, it drops suddenly in W2 laminate while gradually with oscillations in W1 laminate. The reason for the difference is that carbon fibers in the outside layers behave more brittle than glass fibers in the outside layers. Also, carbon/epoxy laminate being stiffer deforms less and therefore carry higher load than other laminates. Glass/epoxy being more flexible absorbs energy more through global deformation and therefore carry lower load. The drop in load after the peak load is reached implies back surface splitting and penetration

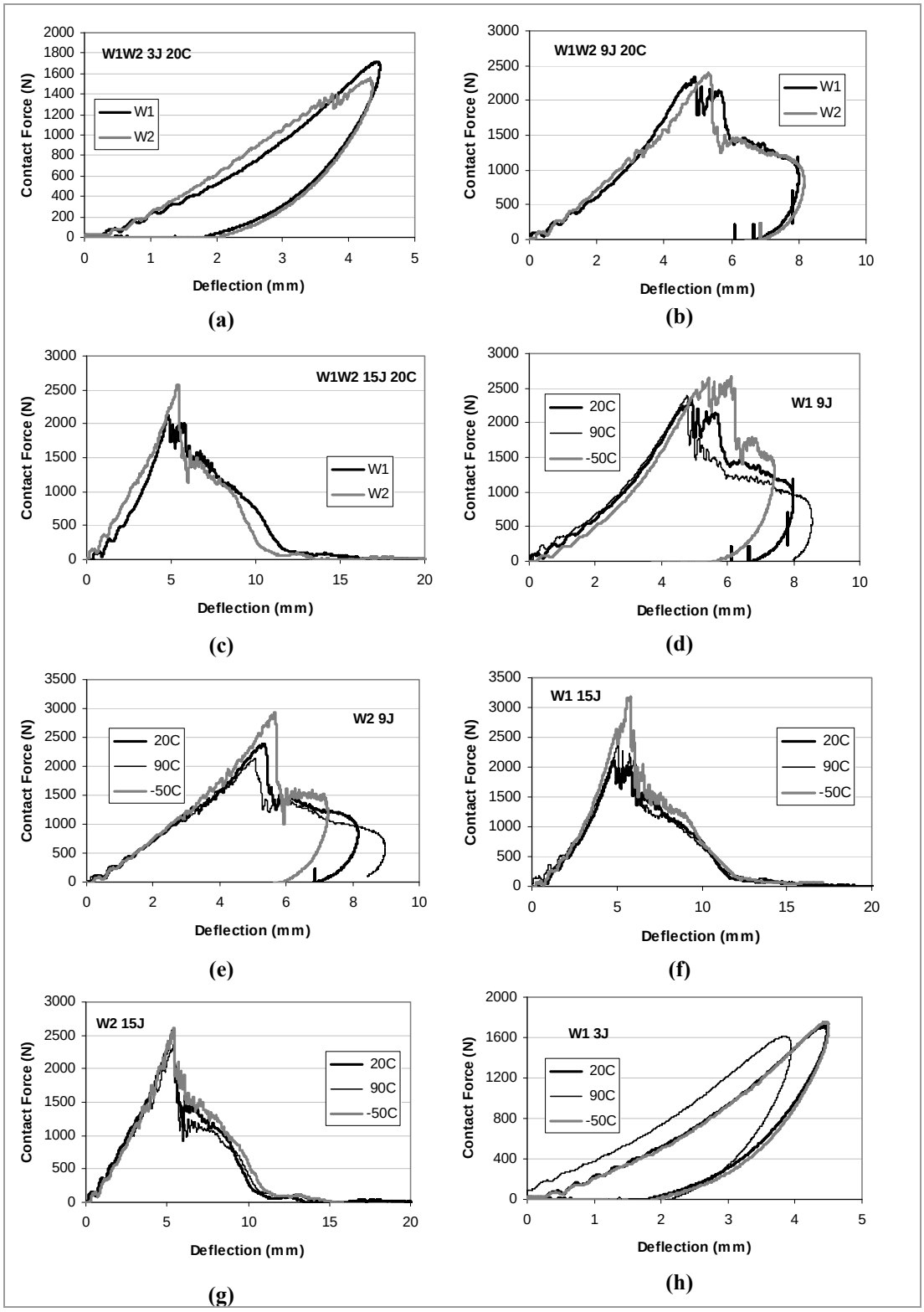

Figure 6.30 Force-deflection curves of woven hybrid laminates at low, intermediate and high impact energies

Figure 6.31 show the energy profile diagrams and maximum contact force versus impact energy curves for both the laminates. It is seen from Figure 6.31.a that the

absorbed energies are nearly identical up to penetration threshold. The perforation threshold of W1 laminate is slightly higher than that of W2 laminate. When the variation of absorbed energy with temperature is investigated, up to impact energy of 9 J, the absorbed energies at 20 and 90 °C are the same while slightly lower at -50 °C. Also, the perforation threshold is higher at lower temperature for both the laminates. As shown in Figure 6.31.b, with increasing the impact energy, maximum contact force reaches a constant value as well higher for W2 laminate. Maximum contact forces at 20 and 90 °C have close values while it is higher at -50 °C for both laminates. (Figure 6.31.c-d)

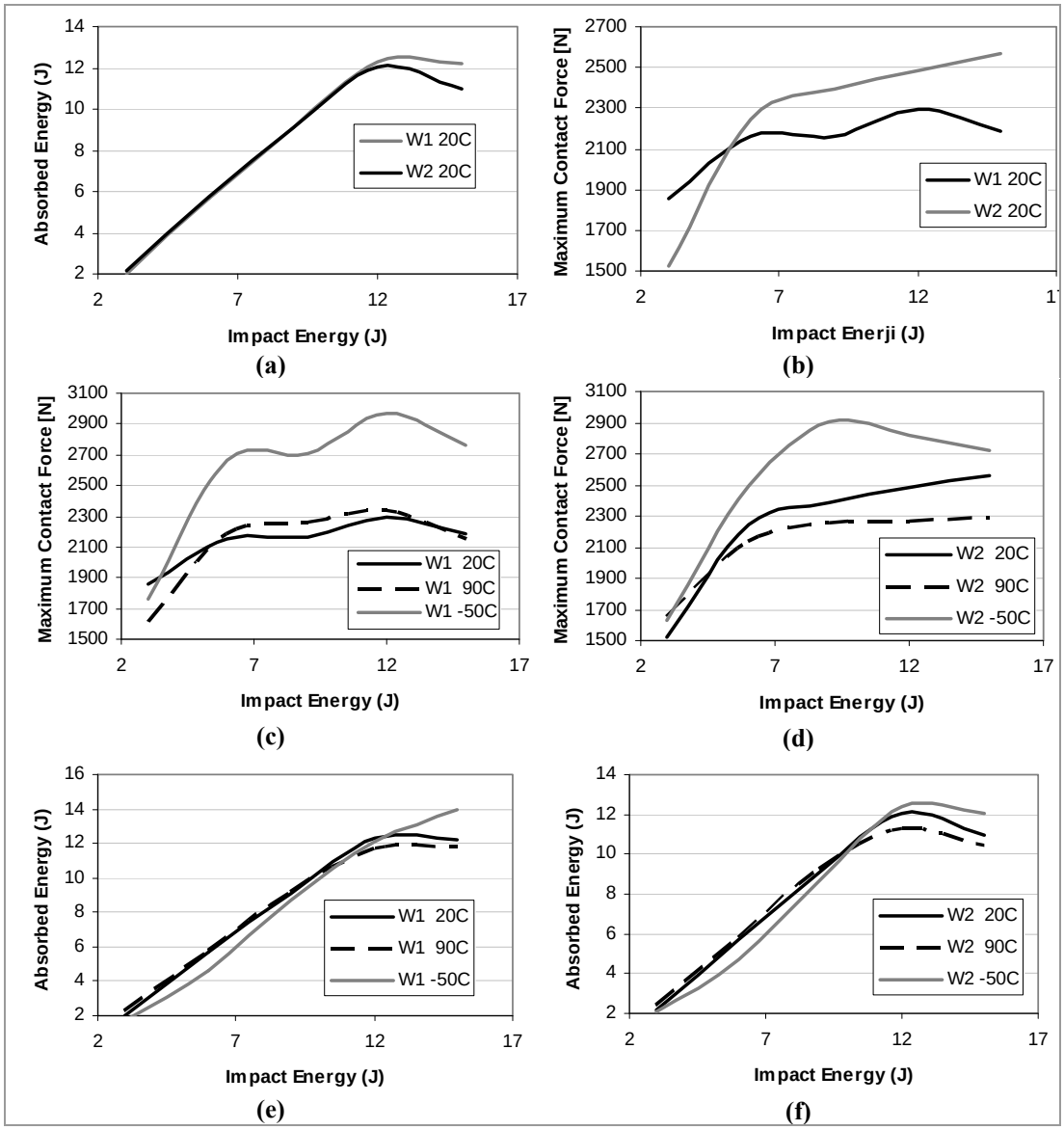

Figure 6.31 The energy profile diagrams and maximum contact force versus impact energy curves

Table 6.12 presents impact parameters like peak load, energy to peak load, time to peak load, deflection at peak load, and absorbed energy for W1 and W2 laminates at 20, 90 and -50 °C temperature. It is seen from the table that maximum load, energy to maximum load and absorbed energy increase with impact energy for both the laminates. Time to peak load decreases with increase in impact energy.

Table 6.12 The impact parameters of woven hybrid composites at 20, 90 and -50 °C temperature

Specimen Type Temperature (°C) and Impact Energy (J)	Permanent Deflection (mm)	Peak Time (ms)	Max. Force (N)	Max. Deformation (mm)	Energy to Max. Force (J)	Total Time (ms)	Absorbed Energy (J)
W1 20C 3J	2.14	4.87	1855	4.20	2.72	10.85	1.97
W1 20C 6J	5.16	4.20	2158	5.69	4.47	11.68	5.70
W1 20C 9J	7.12	2.89	2159	5.02	4.81	13.14	9.11
W1 20C 12J	12.55	2.27	2296	4.75	4.24	15.60	12.30
W1 20C 15J	16.75	2.13	2184	5.06	4.06	10.58	12.18
W1 90C 3J	2.27	4.84	1606	3.90	2.96	10.07	2.31
W1 90C 6J	4.92	3.63	2190	4.90	4.24	11.71	5.81
W1 90C 9J	7.66	2.34	2263	4.09	4.14	13.60	9.22
W1 90C 12J	14.71	2.07	2341	4.28	4.32	13.56	11.77
W1 90C 15J	16.48	2.01	2151	4.77	4.11	10.17	11.80
W1 -50C 3J	0.75	5.63	1760	4.62	3.06	12.88	1.69
W1 -50C 6J	3.41	4.86	2664	5.65	5.54	10.10	4.59
W1 -50C 9J	5.99	3.39	2705	5.74	5.92	11.43	8.72
W1 -50C 12J	8.12	3.06	2965	6.18	6.77	13.87	12.07
W1 -50C 15J	16.26	2.37	2758	5.47	6.11	12.72	13.91
W2 20C 3J	2.59	5.48	1525	4.51	3.00	11.11	2.20
W2 20C 6J	4.58	4.22	2244	5.41	5.04	12.13	5.72
W2 20C 9J	7.09	3.08	2390	5.24	5.40	13.31	9.07
W2 20C 12J	15.14	2.66	2486	5.44	5.52	15.50	12.06
W2 20C 15J	13.93	2.29	2564	5.32	5.71	7.97	10.96
W2 90C 3J	2.46	5.98	1648	3.88	2.95	10.38	2.43
W2 90C 6J	4.17	4.05	2140	4.91	5.26	11.86	5.77
W2 90C 9J	8.29	2.97	2253	5.03	5.20	13.79	9.23
W2 90C 12J	16.23	2.63	2265	5.39	5.32	13.79	11.32
W2 90C 15J	14.21	2.25	2291	5.24	5.28	7.91	10.49
W2 -50C 3J	2.32	5.23	1629	4.36	2.98	10.76	2.05
W2 -50C 6J	3.62	4.87	2492	5.78	5.84	9.98	4.70
W2 -50C 9J	5.65	3.44	2908	5.65	6.60	11.58	8.71
W2 -50C 12J	12.83	2.97	2816	6.03	6.25	16.18	12.41
W2 -50C 15J	14.06	2.33	2719	5.41	5.87	8.65	12.09

At low impact energy of 3J, there is little dent or matrix cracking at the point of impact due to contact forces. At impact energy of 6 J, the laminates exhibit matrix cracking both at the point of impact as well as on the back surface. At intermediate

impact energy of 9 J, the damage area in the front surface displays delamination in a cross shape with the points lying in the warp amd weft directions of the fibers. The damage of the back surface was observed as a combination of extensive delamination at the central region and interface debonding in the surrounding regions. At 12 J, both the woven laminates are partially penetrated by the impactor. The back face is split both along the fill and warp directions. Size of cracks along the two directions is little more than that of the diameter of the impactor, which is 12.7 mm. At 15 J, complete perforation takes place. The damages of the W1 and W2 laminates at the front and back surfaces at 15 J are shown in Figure 6.32.

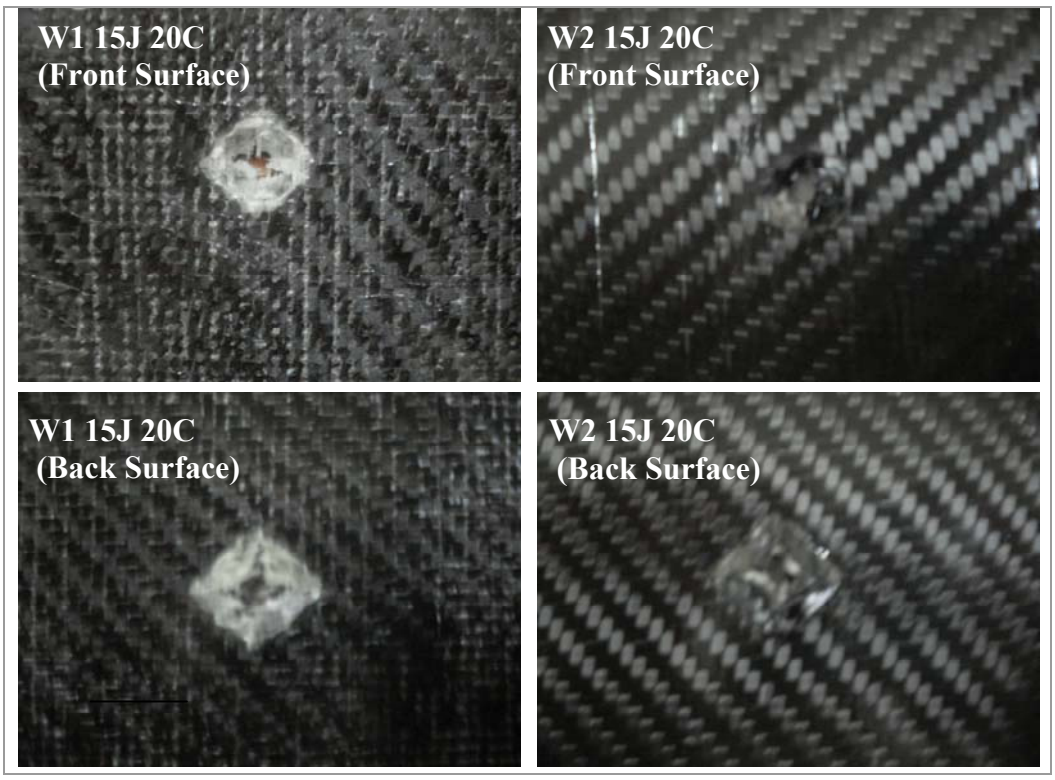

Figure 6.32 The damages of the W1 and W2 laminates at high impact energy of 15 J

Owing to the interlacing of fibers in two equally perpendicular directions, woven fabric composites present excellent resistance to impact damage (Hosur, Adbullah, Jeelani, 2005). Normally impact damage is initiated as matrix crack, which extends to the interface of two laminae and progresses as delamination. Matrix cracks begin as either tensile or shear cracks. In both cases, the crack will initiate transverse to the fibers within a layer. They will propagate through the thickness when they come

across stiffer fibers in the ply leading to development of delamination. The extent of delamination will depend on the portion of impact energy available to fracture the interface. In the case of thin unidirectional laminates, the ply on the back surface splits open during the impact event and the splitting leads to the large delamination. This process triggers generation and propagation of multiple delaminations, which leads to the reduction in residual properties, especially the compressive strength. In comparison, the plain weave fabric composites offer considerable advantage. In woven laminates, fibers run in both directions and are woven such that the fiber tows in each direction run above and below the tows in the other direction. When a laminate made of woven fabrics is subjected to impact loading beyond threshold energy level, a crack is initiated within the ply. When it tries to propagate through the thickness, it will have to cut through the fiber in the fill or warp direction. Unless the energy available is high enough to fracture the fiber tow, the growth of crack is arrested. Hence, the delamination initiation and progression will be restrained. This will help in significantly reducing the delamination damage.

6.3.6 Microscopic Inspection

More information about impact induced damages in composite laminates was obtained by taking the photographs of the cross-sections by a digital camera with high resolution after cutting the specimen through the impact point by means of a water jet cutter. In the laminates, damage consisted mainly of matrix cracks, debonding and fiber failure (all of them increased with the impact energy). Matrix cracks of 45° at low impact energies create an inverse pine tree, which characterizes thin laminate behaviour under impact loading (Abrate, 1998). As energy increases, these cracks join and produce delaminations and, finally, fiber fracture and fiber-matrix debonding of the lower plies. This trend was observed when keeping the temperature constant and increasing impact energy. Also, it is seen that when keeping a constant impact energy and decreasing the temperature from 90 to -50 °C, higher crack density, larger delamination areas, and fiber–matrix debonding regions were observed. The photographs of the sections of composite laminates are given in Figure 6.33-35.

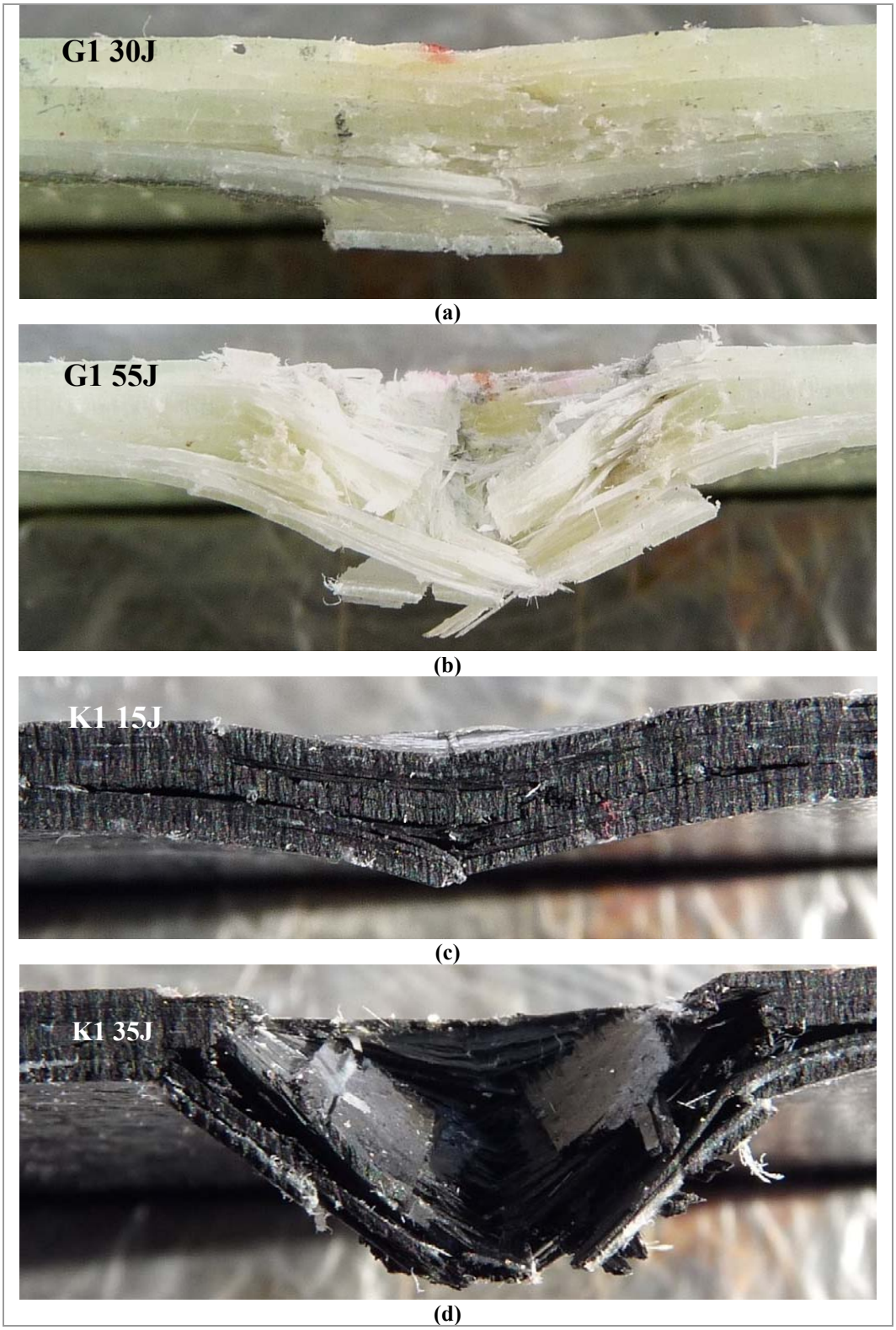

Figure 6.33 The photographs of the cross sections of the impacted laminates

(e)

(f)

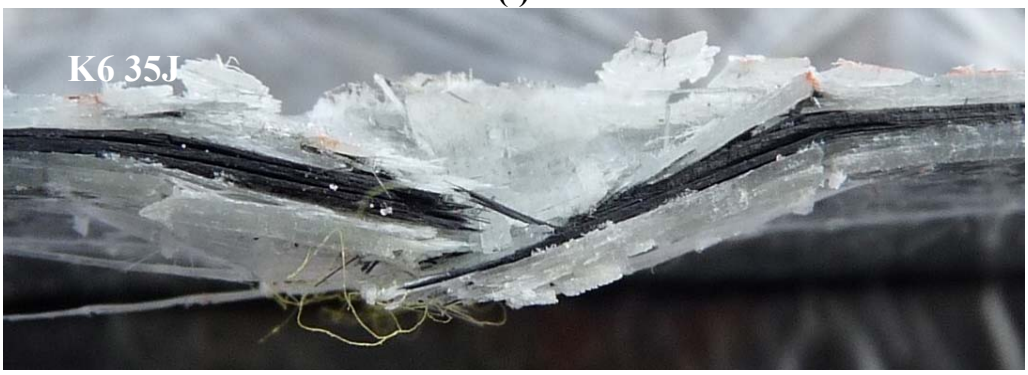

(g)

(h)

Figure 6.34 The photographs of the cross sections of the impacted laminates

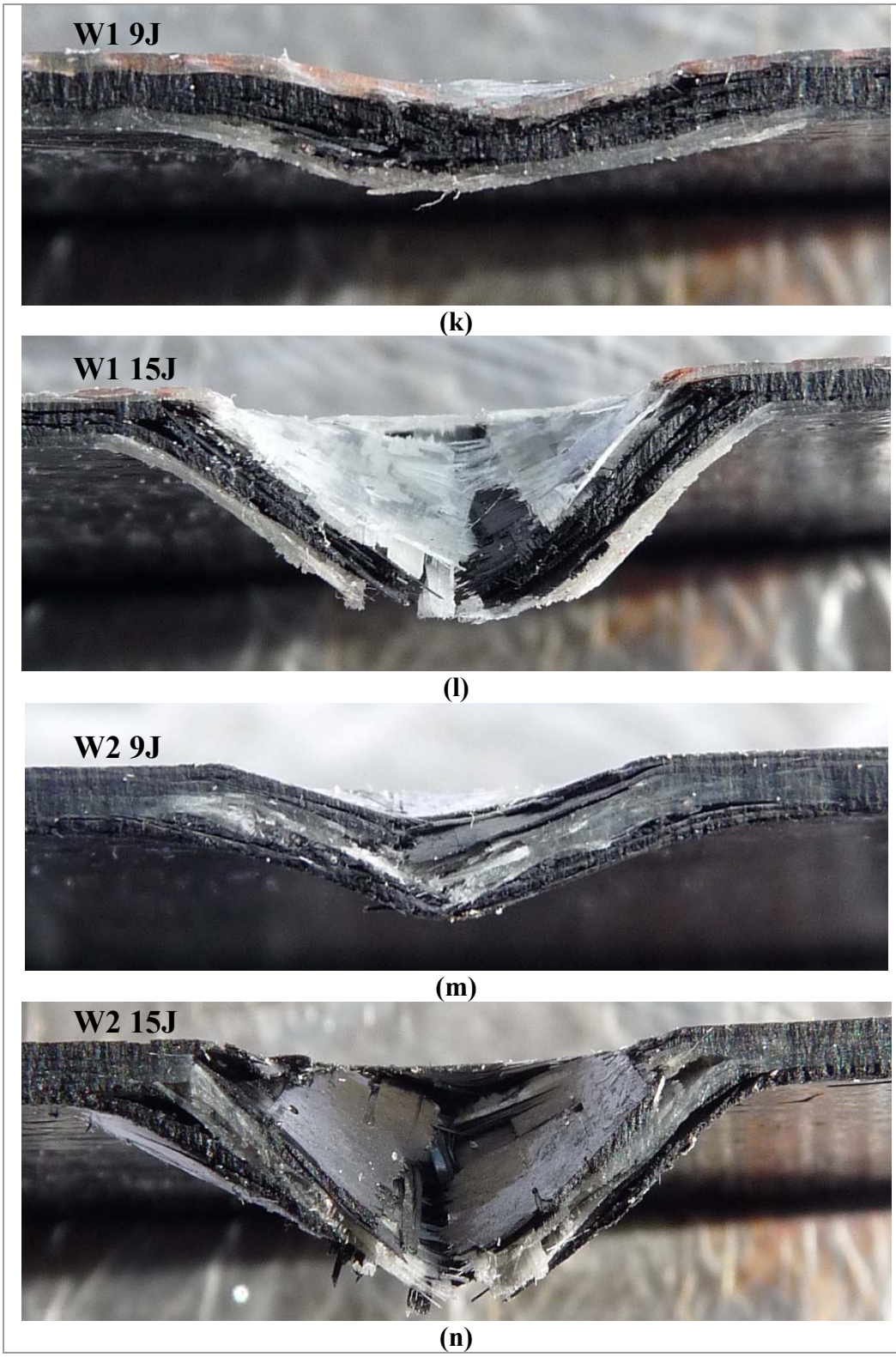

Figure 6.35 The photographs of the cross sections of the impacted laminates

Delaminated surfaces were also observed by a optical microscope. These observations showed no noticeable change on the fracture surfaces with temperature. Delamination always produced the same pattern: separation of fibers and matrix, leaving carbon and glass fibers in the lower ply and fiber marks in the upper ply (Figure 6.36). As a result, no differences were found in the fracture surface topography at 20, -50 and 90 °C.

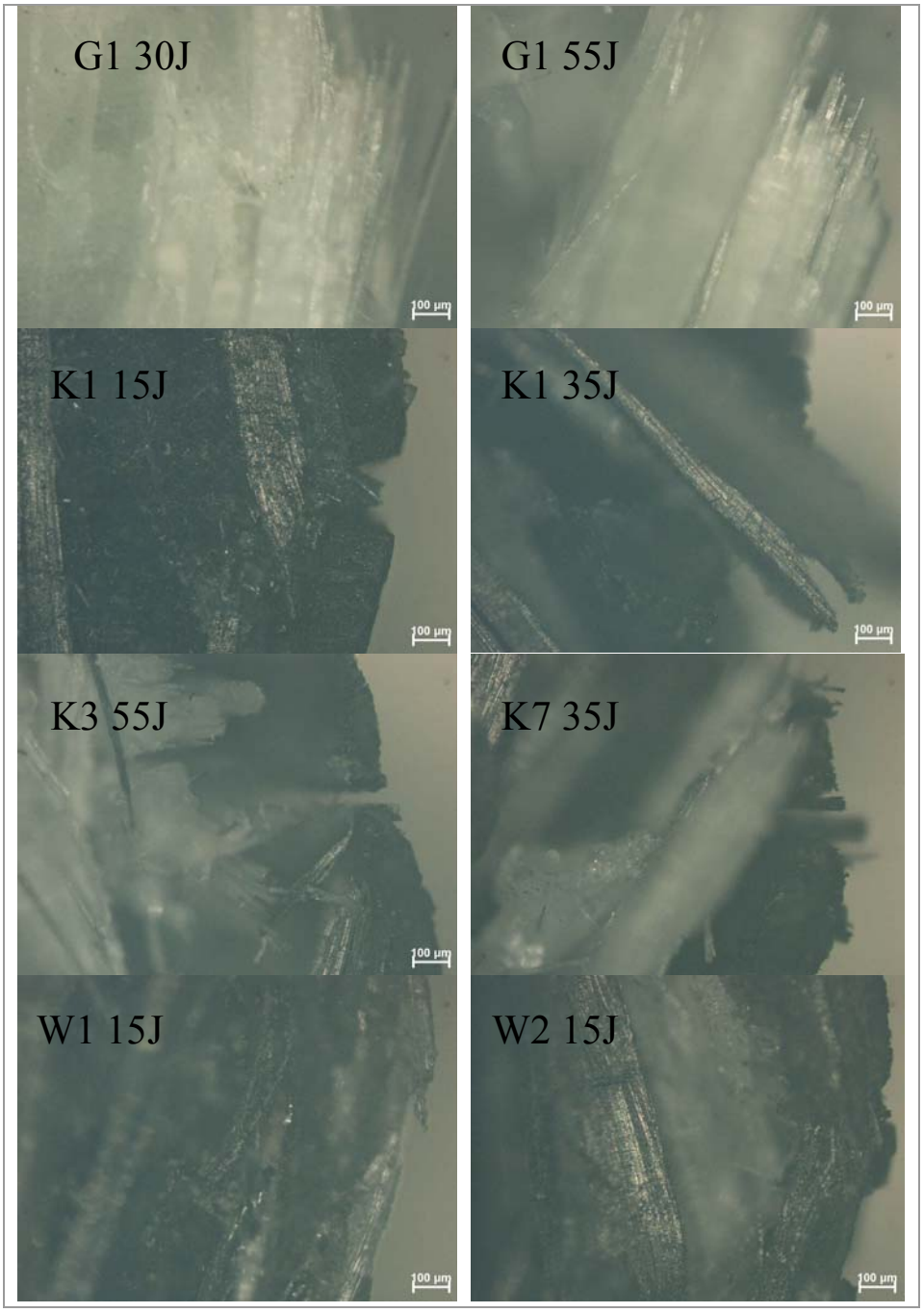

Figure 6.36 Optical microscope images of the damaged zones in the impacted laminates

CHAPTER SEVEN

STATIC THREE-POINT BENDING TESTS

It is of particular interest to understand to what extent the impacted materials can sustain further loading. It has been found that tensile, compression and flexural properties are reduced when impact damage is present in specimens (Bibo, Hogg & Role, 1996; Guild, Hogg, & Richard, 1993). In this study, flexural testing was carried out to evaluate post impact properties, namely flexural strength and modulus. It was expected that a correlation between the impact energies, the damage magnitudes and residual flexural properties would be founded.

To examine the residual bending strength of the specimen subjected to impact damage, a static three-point bending test was carried out using a fixture attached to INSTRON testing machine for experiments involving impacted-side compression. The used three-point bending test apparatus is shown in Figure 7.1. In the bending test, maximum loading and bending stresses were defined to be those when the specimen first fractured. Fractured bending stresses were measured making the assumption that the specimens were homogeneous isotropic material (Malvern, Sun, & Liu, 1989), because the stresses of the laminates are linearly proportional to strain up to the point of rupture.

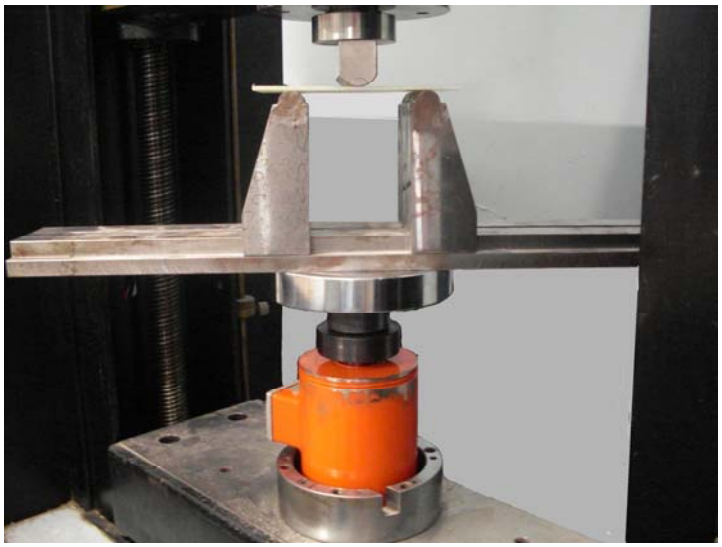

Figure 7.1The three-point bending test apparatus

The effects of dimensional error can be eliminated by using true measurement. The maximum flexural stress, σ, was measured using the linear elastic small displacement bending equation as follows:

$$I = \frac{bh^3}{12} \qquad \sigma = \frac{(PL/4)(d/2)}{I} = \frac{3PL}{2bh^2}$$

where σ is the bending stress (MPa), P is is the maximum loading at fracture (N), L is the length of the span (mm), b is the width of specimen (mm), h is the thickness of specimen (mm), and I is the moment of inertia (mm^4).

The bending modulus (E_B) was calculated from the measured load/crosshead displacement curves by using beam equation:

$$E_B = \frac{L^3 m}{4bh^3}$$

where m is the slope of load/deflection curve in elastic regime

7.1 Three-Point Bending Test Results

As shown in Table 7.1, the maximum loading at fracture, the maximum bending stress, the maximum shear stress and the bending modulus were obtained for each type, temperature and impact energy level. It is seen from the tables that as expected, at any temperature, with increasing impact energy level, the amount of residual bending strength and stiffness in all the specimen types is reduced. This is because with increasing impact energy, crack length and interlaminar damage increases and consequently reduces post-impact bending strength and modulus. Also, in general, the residual bending stiffness slightly less reduced with increasing impact energies when compared to residual bending strength. The bending stiffness is not particularly sensitive to the damage presence. Relatively bending strength is more severely affected by impact damage, leading to higher reductions. This higher sensitivity can

be explained by the fact that the impact damage is localized in most cases and for that reason it has less effect on global properties such as bending stiffness. The calculation of bending stiffness only involves the initial linear part of force/deflection curves. Conversely localized impact damage has adverse effect on the load bearing capability of materials, referred to as ‘‘residual strength’’ or ‘‘strength after impact’’. The flexural strength is calculated using the ultimate force that the specimens could sustain and this is dramatically reduced due to the presence of impact degradation

Generally, for the same impact energy level and temperature, the G1, H4, K3, K1 laminates with $[90/0/0/90]_s$ have higher residual bending strength than their other orientations. For example, at impact energy level of 40 J and 20 °C temperature, residual bending strength of the G1 laminate is 557 MPa, while that of the G2 and G3 laminates are 431 and 422 MPa, respectively. This is because more fibers carry the bending moment in cross-ply laminates. Therefore, it can be concluded that the cross-ply laminated composites provide high post-impact strength.

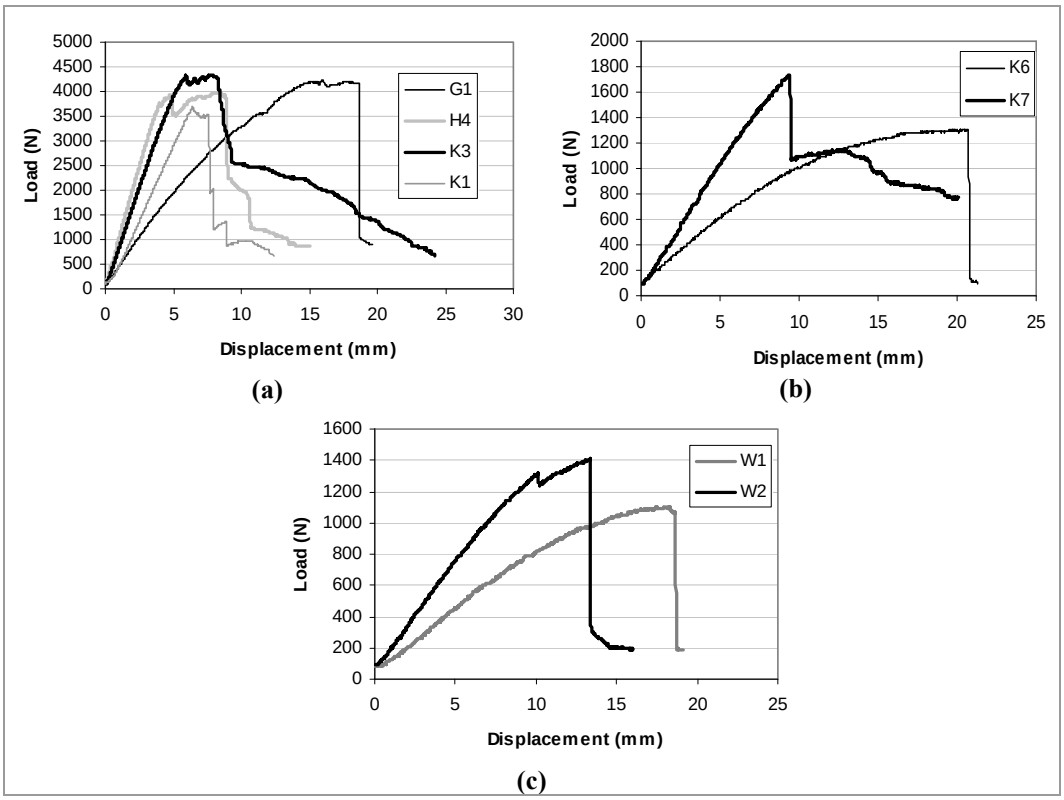

Figure 7.2 Load-displacement curves obtained from three point tests

The K1 specimens impacted at 5 J have highest residual bending strength and stiffness. If post-impact performance of the cross-ply laminates at impact energy of 5 J and 20 °C are compared by means of force-deflection curves given in Figure 7.2, it is evident that the order of the decreasing residual bending stiffness is K1, K3, H4 and G1 laminates. The residual bending stiffness of K7 laminate is two times higher than that of K6 (Figure 7.2).

At low impact energy of 5 J, the residual strengths of the laminates do not change nearly with changing impact temperature because damage was located in the contact area. At high impact energies, since impact damage areas vary with temperature, it is expected that the residual strengths also change. However, as shown in Tables 7.1-5, the effect of impact temperature on the residual bending strength is mixed. The reason is that the global mechanical properties of the impacted specimens return to that at room conditions during three-point bending test process. Also, the width of the laminates is much greater than damage expansion even at high impact energies and so that, a reduction in bending strength is almost insensitive to the difference of damage areas with impact temperature.

Table 7.1 After impact, three-point bending test results of dry laminates

Specimen Type-Temperature (°C) -Impact Energy	**P_{max} [N]**	**σ_{max} [MPa]**	**τ_{max} [MPa]**	**E_B [MPa]**
G1-50C-5J	3894	706.24	11.39	23990
G1-50C-10J	3806	625.13	10.55	23193
G1-50C-20J	3796	671.83	10.92	23060
G1-50C-30J	3767	603.69	10.30	21623
G1-50C-40J	3649	569.83	9.87	19657
G2-50C-5J	3345	570.72	8.56	24925
G2-50C-10J	3315	581.06	9.48	19783
G2-50C-20J	3149	479.78	8.40	19609
G2-50C-30J	3217	456.38	8.27	19557
G2-50C-40J	3060	512.98	8.56	19313
H4-50C-5J	4208	706.79	10.92	47312
H4-50C-10J	3973	676.85	10.35	46225
H4-50C-20J	3845	562.51	10.05	45261
H4-50C-30J	3482	532.16	9.31	41579
H4-50C-40J	2727	471.69	7.75	39006

Table 7.2 After impact, three-point bending test results of dry laminates

Specimen Type-Temperature (°C) -Impact Energy	P_{max} [N]	σ_{max} [MPa]	τ_{max} [MPa]	E_B [MPa]
H5-50C-5J	4188	663.35	11.40	53102
H5-50C-10J	4110	613.67	10.85	47440
H5-50C-20J	3561	543.15	9.51	47159
H5-50C-30J	2678	456.02	7.55	43856
H5-50C-40J	2756	442.91	7.56	41877
H6-50C-5J	3757	595.79	10.24	54948
H6-50C-10J	3590	545.04	9.57	50765
H6-50C-20J	3423	549.88	9.38	48422
H6-50C-30J	3315	513.85	8.93	45145
H6-50C-40J	2898	479.83	8.03	40978
K1-50C-5J	3453	767.77	11.13	62382
K1-50C-10J	3237	698.42	10.26	57448
K1-50C-15J	3413	647.95	10.16	56835
K1-50C-20J	3070	685.59	9.90	54789
K2-50C-5J	3050	610.00	9.30	53060
K2-50C-10J	3453	628.68	10.06	52889
K2-50C-15J	3786	658.69	10.79	48878
K2-50C-20J	2648	497.29	7.83	46787
K3-50C-5J	3835	599.48	10.05	44067
K3-50C-10J	3619	558.69	9.71	42074
K3-50C-20J	3502	564.43	9.89	44865
K3-50C-30J	3207	474.01	8.41	37267
K3-50C-40J	3531	522.47	9.27	35565
K4-50C-5J	3708	532.57	9.59	37869
K4-50C-10J	2982	519.12	8.50	35115
K4-50C-20J	2844	418.87	7.46	35106
K4-50C-30J	2697	362.77	6.76	33939
K4-50C-40J	2638	438.81	7.35	32182
K5-50C-5J	3168	462.41	8.27	34144
K5-50C-10J	2697	396.19	7.06	34760
K5-50C-20J	2658	374.94	6.82	33759
K5-50C-30J	2580	369.06	6.67	29050
K5-50C-40J	2246	313.65	5.72	27509
K6-50C-5J	1393	502.19	5.71	26209
K6-50C-10J	1363	455.60	5.38	23165
K6-50C-15J	1108	408.69	4.60	21131
K6-50C-20J	1049	391.19	4.38	20649
K7-50C-5J	2060	561.26	7.33	33775
K7-50C-10J	2020	493.64	6.82	32743
K7-50C-15J	1922	491.88	6.64	32576
K7-50C-20J	1530	484.82	5.88	29518

Table 7.3 After impact, three-point bending test results of dry laminates

Specimen Type-Temperature (°C) -Impact Energy	P_{max} [N]	σ_{max} [MPa]	τ_{max} [MPa]	E_B [MPa]
G1-90C-5J	4120	601.24	10.75	15908
G1-90C-10J	3933	591.71	10.43	15126
G1-90C-20J	4041	576.37	10.45	13377
G1-90C-30J	3610	534.42	9.49	13087
G1-90C-40J	3472	510.80	9.10	12634
G2-90C-5J	3629	506.79	9.25	12292
G2-90C-10J	2756	471.22	7.78	12414
G2-9C-20J	3561	491.23	9.03	11366
G2-90C-30J	3325	460.09	8.45	11584
G2-90C-40J	2550	431.26	7.17	11665
G3-90C-5J	3413	483.70	8.77	12464
G3-90C-10J	3247	467.10	8.41	12353
G3-90C-20J	3472	496.26	8.96	11931
G3-90C-30J	2923	485.83	8.14	10689
G3-90C-40J	3031	453.70	8.00	10532
H4-90C-5J	4071	594.74	10.63	43919
H4-90C-10J	3845	590.56	10.30	30220
H4-90C-20J	4110	641.05	11.10	32530
H4-90C-30J	4100	591.93	10.65	33793
H4-90C-40J	3041	517.11	8.56	33657
H5-90C-5J	4228	670.02	11.52	50426
H5-90C-10J	3502	516.40	9.20	41070
H5-90C-20J	3394	457.26	8.52	40191
H5-90C-30J	3443	504.25	9.01	37417
H5-90C-40J	3198	470.44	8.38	36412
H6-90C-5J	4100	682.75	11.44	53151
H6-90C-10J	3914	672.62	11.10	49411
H6-90C-20J	3286	502.16	8.79	40751
H6-90C-30J	3158	530.79	8.86	40271
H6-90C-40J	3001	514.75	8.49	39057
K1-90C-5J	4149	825.57	12.64	57155
K1-90C-10J	3570	752.09	11.19	51728
K1-90C-15J	4031	723.44	11.67	49839
K1-90C-20J	4061	718.52	11.68	45992
K2-90C-5J	4071	754.34	11.98	52047
K2-90C-10J	4022	745.34	11.83	54877
K2-90C-15J	3404	672.57	10.34	50258
K2-90C-20J	3816	643.71	10.70	43812
K3-90C-5J	4071	640.47	11.01	38081
K3-90C-10J	4273	641.13	11.30	38137
K3-90C-20J	3610	494.92	9.13	27235
K3-90C-30J	4080	533.94	10.08	26244
K3-90C-40J	3168	437.98	8.05	24507

Table 7.4 After impact, three-point bending test results of dry laminates

Specimen Type-Temperature (°C) -Impact Energy	P_{max} [N]	σ_{max} [MPa]	τ_{max} [MPa]	E_B [MPa]
K4-90C-5J	3315	481.36	8.63	34548
K4-90C-10J	3256	488.88	8.62	32041
K4-90C-20J	3825	558.97	9.99	31714
K4-90C-30J	2697	373.27	6.86	22276
K4-90C-40J	2580	378.97	6.75	28164
K5-90C-5J	3227	484.62	8.54	32141
K5-90C-10J	3090	450.75	8.06	29489
K5-90C-20J	2648	446.06	7.42	30638
K5-90C-30J	2589	408.49	7.02	29215
K5-90C-40J	2481	364.57	6.49	26706
K6-90C-5J	1187	422.84	4.84	18777
K6-90C-10J	1088	387.19	4.43	17276
K6-90C-15J	1078	404.43	4.50	16978
K6-90C-20J	1030	378.34	4.26	16405
K7-90C-5J	1559	505.82	6.07	34931
K7-90C-10J	1442	452.58	5.52	32495
K7-90C-15J	1245	390.75	4.76	29009
K7-90C-20J	1451	449.56	5.51	30051
G1-20C-5J	4218	603.19	10.90	15589
G1-20C-10J	3835	545.54	9.85	14748
G1-20C-20J	3904	594.76	10.41	14167
G1-20C-30J	3462	558.79	9.50	14011
G1-20C-40J	3453	557.34	9.47	11821
G2-20C-5J	3355	525.41	9.06	14207
G2-20C-10J	3247	533.74	9.01	12881
G2-20C-20J	3247	484.04	8.56	11789
G2-20C-30J	2854	445.71	7.69	12235
G2-20C-40J	2727	431.56	7.39	11881
G3-20C-5J	3276	504.63	8.77	12421
G3-20C-20J	2972	424.84	7.67	11340
G3-20C-30J	3080	436.81	7.92	11143
G3-20C-40J	2864	422.19	7.52	10004
H4-20C-5J	3973	629.04	10.81	51769
H4-20C-10J	3727	584.13	10.08	50124
H4-20C-20J	3649	558.07	9.77	47048
H4-20C-30J	2962	526.29	8.52	46080
H4-20C-40J	2727	459.87	7.65	43907
H5-20C-5J	3953	595.67	10.50	52423
H5-20C-10J	3727	598.59	10.21	46600
H5-20C-20J	3355	471.71	8.61	45856
H5-20C-30J	3668	524.38	9.47	43358
H5-20C-40J	3197	494.20	8.58	40282
H6-20C-5J	4296	705.89	11.91	57179
H6-20C-10J	3119	597.06	9.33	53687
H6-20C-20J	3531	525.34	9.32	44290
H6-20C-30J	2992	568.25	8.91	47801
H6-20C-40J	3090	507.63	8.57	44909

Table 7.5 After impact, three-point bending test results of dry laminates

Specimen Type-Temperature (°C) -Impact Energy	P_{max} [N]	σ_{max} [MPa]	τ_{max} [MPa]	E_B [MPa]
K1-20C-5J	4306	708.23	13.51	57644
K1-20C-10J	3423	644.89	10.16	49823
K1-20C-15J	3767	698.15	11.08	42864
K1-20C-20J	3139	590.38	9.30	39897
K2-20C-5J	3433	683.99	10.47	57197
K2-20C-10J	2815	602.95	8.89	57962
K2-20C-15J	2648	588.31	8.53	48684
K2-20C-20J	2854	528.15	8.38	45302
K3-20C-5J	4345	653.17	11.51	45763
K3-20C-10J	4041	598.71	10.63	40404
K3-20C-20J	3835	624.07	10.57	36362
K3-20C-30J	3610	478.99	8.98	36158
K3-20C-40J	3237	475.71	8.47	32817
K4-20C-5J	3041	473.23	8.19	39616
K4-20C-10J	3041	400.26	7.53	36290
K4-20C-20J	2893	457.04	7.86	32546
K4-20C-30J	2825	387.37	7.14	32127
K4-20C-40J	2629	401.59	7.03	29738
K5-20C-5J	2992	384.00	7.32	32953
K5-20C-10J	2874	386.43	7.20	31831
K5-20C-20J	2668	383.50	6.90	30354
K5-20C-30J	2472	346.00	6.31	30045
K5-20C-40J	2275	321.20	5.84	28260
K6-20C-5J	1304	479.18	5.39	17472
K6-20C-10J	1216	452.97	5.07	15463
K6-20C-15J	1098	372.69	4.36	14397
K6-20C-20J	922	350.60	3.88	13596
K7-20C-5J	1736	574.57	6.79	36372
K7-20C-10J	1648	556.40	6.50	35983
K7-20C-15J	1393	426.76	5.25	34387
K7-20C-20J	1393	443.57	5.38	31996

When the residual strengths of the saturated impacted laminates are investigated, it is seen in Table 7.6 that the strengths of the saturated laminates also decreases with increasing impact energy. If the laminates is compared with dry laminates, it is noticed that the bending residual strengths of the saturated laminates are slightly higher that that of the dry laminates. This reason is probably that the layers expands after sea water immersion and so that, the residual stresses occuring during manufacture are vanished. In this case, the slight increase in the strength of the saturated laminates is possible.

Table 7.6 After impact, three-point bending test results of the saturated laminates

Specimen Type-Temperature (°C) -Impact Energy	P_{max} [N]	σ_{max} [MPa]	τ_{max} [MPa]	E_B [MPa]
TS G1-20C-5J	3659	597.70	10.09	18433
TS G1-20C-30J	3374	498.49	8.85	11548
TS G2-20C-5J	3256	526.17	8.94	12741
TS G2-20C-30J	2933	437.14	7.73	11671
TS G3-20C-5J	3531	495.07	9.04	11450
TS G3-20C-30J	3198	456.37	8.24	9908
TS H4-20C-5J	4316	640.09	11.36	49175
TS H4-20C-30J	3708	553.31	9.79	40197
TS H5-20C-5J	4394	709.71	12.07	53530
TS H5-20C-30J	3031	429.26	7.81	39478
TS H6-20C-5J	3600	513.78	9.31	46630
TS H6-20C-30J	3315	504.82	8.83	43520
TS K1-20C-5J	3413	732.78	10.81	61952
TS K1-20C-15J	2727	557.10	8.43	46372
TS K2-20C-5J	3580	743.01	11.15	55490
TS K2-20C-15J	3639	707.46	10.97	53007
TS K3-20C-5J	4551	654.75	11.79	40066
TS K3-20C-30J	3884	550.78	9.98	33274
TS K4-20C-5J	3433	541.76	9.31	38830
TS K4-20C-30J	3296	464.05	8.44	31825
TS K5-20C-5J	3207	517.04	8.73	37804
TS K5-20C-30J	2972	452.95	7.93	32454
TS G1-50C-5J	4031	661.95	11.17	15202
TS G1-50C-30J	3580	548.06	9.56	14299
TS G2-50C-5J	3482	507.48	9.07	12109
TS G2-50C-30J	2874	419.37	7.50	9759
TS G3-50C-5J	3443	468.33	8.66	12260
TS G3-50C-30J	3080	489.07	8.38	12019
TS H4-50C-5J	4500	609.99	11.32	45130
TS H4-50C-30J	3551	529.52	9.37	41427
TS H5-50C-5J	4071	590.43	10.59	49524
TS H5-50C-30J	3796	520.88	9.60	43584
TS H6-50C-5J	4542	666.74	11.92	49391
TS H6-50C-30J	3767	602.19	10.27	45078
TS K1-50C-5J	3835	720.71	11.35	49233
TS K1-50C-15J	3668	711.25	11.02	46085
TS K2-50C-5J	2923	580.64	8.89	51173
TS K2-50C-15J	2550	477.75	7.52	49262
TS K3-50C-5J	4345	557.82	10.63	33572
TS K3-50C-30J	3305	517.74	8.93	33230
TS K4-50C-5J	3256	512.71	8.81	37882
TS K4-50C-30J	3041	448.06	7.98	30290
TS K5-50C-5J	2727	386.17	7.00	32614
TS K5-50C-30J	2354	366.76	6.35	29271

The stiffness of the carbon-outside/glass-inside W2 laminate is approximately two times higher that that of the carbon-inside/glass-outside W2 laminate. Also, for the same impact energy and temperature, the residual bending strength of W2 laminate is higher than that of W1 laminate. When the effect of the temperature on residual strength is investigated, it is seen that the reduce in residual strength at high impact energy of 15J is greater for temperatures of -50 and 90 °C when compared at 20 °C.

Table 7.7 After impact, three-point bending test results of the woven hybrid laminates

Specimen Type-Temperature (°C) -Impact Energy	**P_{max} [N]**	**σ_{max} [MPa]**	**τ_{max} [MPa]**	**E_B [MPa]**
W1-20C-3J	1128	564.54	5.43	20659
W1-20C-6J	1098	541.50	5.25	16479
W1-20C-9J	1010	473.63	4.71	18338
W1-20C-12J	931	478.76	4.55	18438
W1-50C-3J	1069	508.17	5.02	13165
W1-50C-6J	1020	510.44	4.91	16701
W1-50C-9J	971	493.56	4.72	20543
W1-50C-12J	882	458.46	4.33	13332
W1-90C-3J	1147	581.58	5.56	17209
W1-90C-6J	1039	469.86	4.76	18911
W1-90C-9J	1010	486.84	4.78	15034
W1-90C-12J	882	440.86	4.24	16609
W2-20C-3J	1412	705.91	6.79	42607
W2-20C-6J	1265	556.54	5.25	40999
W2-20C-9J	1206	661.19	6.07	43452
W2-20C-12J	1069	631.98	6.08	38567
W2-50C-3J	1363	699.26	6.64	47206
W2-50C-6J	1216	608.23	5.85	48668
W2-50C-9J	1265	630.37	6.07	43135
W2-50C-12J	1030	516.11	4.97	42827
W2-90C-3J	1294	660.99	6.28	45765
W2-90C-6J	1314	549.69	5.29	44410
W2-90C-9J	1098	672.72	6.39	41060
W2-90C-12J	1069	534.28	5.14	41417

CHAPTER EIGHT
CONCLUSIONS

In this study, low velocity impact tests on the glass/epoxy, carbon/epoxy and glass/carbon hybrid laminated composite plates at 20, 90 and -50 °C temperatures were performed to investigate impact behaviors of the laminates. Impact responses of the composite specimens were characterized in terms of impact parameters such as permanent deflection, maximum contact force, maximum contact time, energy to maximum contact force, and total energy absorption at low, intermediate, and high impact energy levels. Energy profile diagrams and force versus deflection curves were plotted for each temperature and specimen type. Impact tests on the saturated specimens kept in seawater for 7 months were also conducted at the same impact energy levels as that of dry specimens. The initial damage perforation and propagation energies were obtained for each temperature and specimen type. The impacted specimens were observed by visual inspection. A high-intensity light was used to identify the projected delamination areas in the impacted glass/epoxy composite laminates. The photographs of the cross-sections of the impacted specimens were taken. Delaminated surfaces were observed by an optical microscope. There point bending tests on the impacted specimens were also performed. In addition, mechanical properties of unidirectional glass/epoxy and carbon/epoxy composite plates were determined at 20 and 90 °C temperature. Thermal residual stresses at 20, 90 and -50 °C temperatures were obtained by using ANSYS software and the effects of the residual stresses on matrix cracking damage before impact were analyzed. The results obtained from this study can be summarized as follows.

The mechanical test results showed that when the temperature is increased from 20 °C to 90 °C, mechanical properties of the unidirectional glass/epoxy and carbon/epoxy composite plates are significantly reduced.

The results obtained from both thermal stress analyses and impact tests showed that the contribution of thermal stresses to impact damage increases with decreasing

temperature. Therefore, the residual stresses at low temperatures have a significant effect on the impact damage and the initial energies of unidirectional laminated composites. As a result, damage area increases while the initial energy decreases with decreasing temperature

It was seen that impact resistance of glass/epoxy laminates is higher about two times than that of carbon/epoxy laminates for the same orientations. The perforation thresholds of hybrid composites consisting of glass and carbon fibers have the values between that of glass/epoxy laminates and carbon/epoxy laminates expect for K3, K3, K4 and K5 specimens

The perforation energy threshold of the cross-ply laminated composites is higher than that of the other orientations. When change of perforation energy with temperature was examined, different results were obtained according to reinforcement material used. For glass/epoxy and glass/carbon hybrid laminates, propagation energy decreased with increasing temperature. The opposite of this result was obtained for carbon/epoxy composites.

The K3, K4 and K5 woven carbon-outside/unidirectional glass-inside clustered laminates provide both high impact resistance and carry the highest loading, compared to the other laminates. From the result, it was concluded that there can be tremendous advantage to be had by hybridizing the laminates.

K3 and K6 laminates present high impact resistance at 90 °C temperature, since the partial rebounding takes place while complete perforation occurs in other specimens. As a result of comparisons of the carbon/glass hybrid composites with symmetric and antisymmetric orientations, it was seen that the K6 and K7 laminates with lay ups $[G_{90}/G_0/C_0/C_{90}]_s$ and $[C_{90}/C_0/G_{90}/G_0]_{as}$, respectively have very similar energy profile diagrams at room temperature.

At intermediate impact energy levels, at which the partial rebound of the impactor take place, the permanent deflection increases by increasing the temperature for the

G1, G2, G3, H4, H5, H6, K3, K4 and K5 laminates except for K1 and K2 specimens. The result is also valid for the saturated specimens at temperatures 20 and -50 °C. For carbon/epoxy composites, a consistent variation of permanent deflection with temperature could not be observed. This is probably owing to high brittle structure of carbon fibers.

At low impact energies, matrix cracks of 45° create an inverse pine tree. As energy increases, these cracks join and produce delaminations and, finally, fiber fracture and fiber-matrix debonding of the lower layers. This trend was observed when keeping the temperature constant and increasing impact energy. Also, when keeping a constant impact energy and decreasing the temperature from 90 to -50 °C, higher crack density, larger delamination areas, and fiber-matrix debonding zones were detected. Impact damage area was slightly less extensive in the saturated samples as compared to dry specimens.

In unidirectional laminates, since initial damage occurs as matrix crack and delamination, thermal stresses contribute to the damage. However, in woven composites, no interlaminar thermally induced stresses appear since the fibers run in both directions and damage increase at low temperature is lower in comparison with unidirectional laminates. Therefore, the variation of the initial energy with temperature in woven laminate is less sensitive when compared to unidirectional laminates. In contrary of unidirectional laminates, the initial energy of W1 and W2 woven laminates increase with decreasing temperature. The absorbed energies of W1 and W2 laminates are nearly identical up to penetration threshold. The perforation threshold of W1 laminate is slightly higher than that of W2 laminate. Also, the stiffness of the carbon-outside/glass-inside W2 laminate is approximately two times higher that that of the carbon-inside/glass-outside W2 laminate.

At any temperature, with increasing impact energy level, the amount of residual bending strength and stiffness in all the specimen types was reduced. Also, in general, the residual bending stiffness slightly less reduced with increasing impact energies compared to residual bending strength.

REFERENCES

Abrate, S. (1998). *Impact on composite structures*. Cambridge: Cambridge University Press.

Advanced material committee. (1988) *Advanced materials hand book*, HwanSun, Japan.

Aktas, M. (2007). *Temperature effect on impact behavior of laminated composite plates*. Phd Thesis. Dokuz Eylül University.

Aoki, T., Ishikawa, T., Kumazawa, H., & Morino, Y. (1999) Mechanical behaviour of cf/polymer composite laminates under cryogenic environment. *In ICCM 12,* 5

Aslan, Z., & Karakuzu, R. (2002). Transient dynamic analysis of laminated composite plate subjected to low- velocity impact. *Mathematical & Computational Applications, 7,* (2), 73–82.

Aslan, Z., Karakuzu, R., Okutan, B. (2003). The response of laminated composite plates under low-velocity impact loading. *Composite Structures, 59,* 119-127.

Atas C., & Liu D. (2008). Impact response of woven composites with small weaving angles. *Int J Impact Eng, 35*, 80–97.

Baucom, J. N., & Zikry, M. A. (2005). Low-velocity impact damage progression in woven E-glass composite systems. *Compos Part A, 36* (5), 658–64.

Bibi, G., Leicy, D., Hogg, P. J., & Kemp M. (1994). High temperature damage tolerance of carbon fibre reinforced plastic. *Composites,* 414–24.

Bibo, G.A., & Hogg, P. J. (1996). Role of reinforcement architecture on impact damage mechanisms and post impact compression behaviour. *J Mater Sci,31*, 1115 37.

Caprino, G., Lopresto V., Scarponi, C., & Briotti, G. (1999). Influence of material thickness on the response of carbon-fabric/epoxy panels to low velocity impact. *Composite Science and Technology, 59,* 2279–2286.

Challenger, K. D. (1986). The damage tolerance of carbon fiber reinforced composites: a workshop summary. *Compos Struct*, 295–318.

Chamis, C. C., & Hanson, M.P., Serafini, T. T. (1972). Impact resistance of unidirectional fiber composites. In: Composite materials: testing and design (Second Conference). *ASTM STP, 497*, 324–49.

Cheon, S. S., Lim, T. S., & Lee, D. G., (1999). Impact energy absorption characteristics of glass fiber hybrid composites. *Comp. Struct, 46,* 267–278.

Cho C., & Zhao G. (2002). Effects of geometric and material factors on mechanical response of laminated composites due to low velocity impact. *J Compos Mater, 36*, 1403–28.

Datta, S., Krishna, A.V., & Rao, R.M. (2004). Low velocity impact damage tolerance studies on glass–epoxy laminates – effects of material, process and test parameters. *J Reinf Plast Compos, 23*(3), 327–45.

Dutta P. K. (1994). Low temperature compressive strength of glass fiber reinforced polymer composites. *J Offshore Mech Arctic Eng, 116,* 167–72.

Dutta, P. K., Faran, K. J., & Hui, D. (1999). Influence of low temperature on energy absorption in laminated composites. *In ICCM 9,* 5, 311–20.

Erickson, M. D., Kallmeyer, A. R., & Kellogg, K. G. (2005). Effect of temperature on the low-velocity impact behavior of composite sandwich panels. *Journal of Sandwich Structures and Materials, 7,* 245–264.

Fuoss, E., Straznicky, P. V., & Poon, C. (1998). Effects of stacking sequence on the impact resistance in composite laminates – Part 1: parametric study. *Compos Struct 41,* 67–77.

Fuoss, E., Straznicky, P.V., & Poon, C. (1998). Effects of stacking sequence on the impact resistance in composite laminates. Part 2: prediction method.*Compos Struct, 41*, 177–86.

Go´mez, D. T., Zaera R., Barbero, E., & Navarro, C. (2005). Damage in CFRPs due to low velocity impact at low temperature. *Composites: Part B, 36,* 41–50

Greszczuk, L.G. (1973). Foreign object damages to composite materials. *ASTM STP*, 568.

Guild, F.J., Hogg, P.J., & Richard, J. C. (1993). A model for the reduction in compression strength of continuous fibre composites after impact damage. *Composite, 24* (4), 333–9.

Gustin, J., Joneson, A., Mahinfalah, M., & Stone, J. (2005). Low velocity impact of combination Kevlar/fiber carbon sandwich composite. *J Compos Struct, 69* (4), 396–406.

Harris, B. & Bunsell, A. R. (1975). Impact properties of glass fibre/carbon fibre hybrid composites. *Composites, 6,* 197–201.

Hirai, Y., Hamada, H., & Kim, J. K. (1998). Impact response of glass woven fabric laminates: Part 2. Effect of temperature. *Compos Sci Technol, 58* (1), 119–28.

Hosur M.V., Adbullah M., & Jeelani S. (2005) Studies on the low-velocity impact response of woven hybrid composites. *Compos Struct, 67,* 253–62.

Hosur, M. V., Jain, K., Chowdhury, F., Jeelani S., Bhat M. R., & Murthy C. R. L. (2007). Low-velocity impact response of carbon/epoxy laminates subjected to cold–dry and cold–moist conditioning. *Composite Structures 79*, 300–311

Im, K. H., Cha, C. S., Kim, S. K., & Yang, I. Y. (2001). Effects of temperature on impact damages in CFRP composite laminates. *Composite: Part B, 32,* 669–682.

Imielin´ska, K., Guillaumat, L. (2004). The effect of water immersion ageing on low-velocity impact behaviour of woven aramid-glass fibre/epoxy composites. *Compos Sci Technol 64,* 2271–8.

Ishai, O. & Shragi, A. (1990). Effect of impact loading on damage and residual compressive strength of CFRP laminated beams. *Compos Struct, 14* (4), 319–337.

Jang J., & Lee C., (1998). Performance improvement of GF/CF functionally gradient hybrid composite. *Polymer Testing, 17,* 383-394.

Jang, B. Z., Lieu, Y. K., Chang, Y. S., & Hwang, L. R. (1987). Cryogenic failure mechanisms of fiber–epoxy composites for energy applications. *Polymer Composites, 8,* 188.

Jang, B.Z., Chen, L.C., Wang, C.Z., Lin, H.T., & Zee, R.H. (1989). Impact resistance and energy absorption mechanisms in hybrid composites. *Composites Science and Technology, 34,* 305–335.

Jones, R. M. (1999). *Mechanics of composite materials.* London: Taylor & Francis

Karasek, M. C., Strait L. H., & Amateau M. F. (1995). Effect of temperature and moisture on the impact behaviour of graphite/epoxy composites: parts I and II. *J Mater Res Technol, 17* (1), 3–15.

Khalid, A. A. (2006). The effect of testing temperature and volume fraction on impact energy of composites. *Materials and Design, 27,* 499–506.

Khojin, A. S., Bashirzadeh, R., Mahinfalah, M., & Jazar, R. K. (2006). The role of temperature on impact properties of Kevlar/fiberglass composite laminates, *Composites: Part B, 37* (7–8), 593–602.

Khojin, A. S., Mahinfalah, M., Bashirzadeh, R., & Freeman B. (2007) Temperature effects on Kevlar/hybrid and carbon fiber composite sandwiches under impact loading. *Composite Structures, 78,* 197–206.

Kim, J. K., Sham, M. L., Sohn, M. S. & Hamada, H. (2001). Effect of hybrid layers with different silane coupling agents on impact response of glass fabric reinforced Vinylester matrix composites. *Polymer, 42,* 7455–7460.

Kowsika, M. V. S. L. N., & Mantena, P. R. (1997). Static and low-velocity impact response characteristics of pultruded hybrid glass–graphite/epoxy composite beams. In: R.F. Gibson and G.M. Newaz, Editors, Proceedings of the 12th American Society for Composites, Tecnomic Publishing Co, Lancaster, 610–619.

Lal, K. M. (1982). Prediction of residual Tensile strength of Transversely Impacted Composite laminates. *Research in structural and solid Mechanics,* NASA conference publication*,* 2245; 1982.

Lee, Y.S., Kang, K. H., & Park, O. (1997). Response of hybrid laminated composite plates under low velocity impact. *Comput. Struct, 65* (6), 965–974.

Levin K. (1986). Effect of low velocity impact on compression strength of quasi-isotropic laminate. In: Proceedings of American society for composites: 1st technical conference. Technomic, Lancaster, PA, 313–25.

Liu, D. (2004). Characterization of impact properties and damage process of glass/epoxy composite laminates. *J Compos Mater, 38*, 1425–42.

Ma, C. C. M., Huang, Y. H. & Chang, M. J. (1991). Hygrothermal effect on the PEEK/C.F. and PPS/C. F under impact loading (I). *ANTEC,* 2029–2096.

Malvern, L. E., Sun, C. T., & Liu, D. (1989). Delamination damage in central impacts at subperformation speeds on laminated Kevlar/Epoxy plates. *ASTM STP 1012*, 387–405.

Mitrevski, T., Marshall, I. H., & Thomson, R. (2006). The influence of impactor shape on the damage to composite laminates. *Compos Struct, 76,* 116–22.

Mitrevski, T., Marshall, I. H., Thomson, R., Jones, R., & Whittingham, B. (2005). The effect of impactor shape on the impact response of composite laminates. *Compos Struct, 67,* 139–48.

Morais, W. A., de Monteiro, S. N., & d'Almeida, J. R. M. (2005). Effect of the laminate thickness on the composite strength to repeated low energy impacts. *Composite Structures, 70,* 223–228.

Morii, T., Hamada, H., Desaeger, M., Gotoh, A. (1995). Yokoyama A., Verpoest I. & Maekawa Z., Damage tolerance of glass mat/epoxy laminates hybridized with flexible resin under static and impact loading. *Composite Structures, 32,* 133–139.

Naik, N. K., Ramasimha R, Arya H., Prabhu S.V., & ShamaRao N. (2001). Impact response and damage tolerance characteristics of glass–carbon/epoxy hybrid composite plates. *Compos Part B, 32,* 565–74.

Naik, N. K., & Ramasimha, R. (2000) Impact response of hybrid glass–carbon/epoxy composite plates. In Proceedings of ICEM-9, Bethel: Society for Experimental Mechanics, Inc., 198–201.

Naik, N. K., Meduri, S., & Sekher, Y. C. (2000). Polymer matrix woven fabric composites subjected to low velocity impact: Part II-Effect of plate thickness. *Journal of Reinforced Plastics and Composites, 19* (13), 1031–1055.

Novak, R. C., DeCrescente, M. A. (1972). Impact behavior of unidirectional resin matrix composites tested in the fiber direction. In: Composite materials: testing and design (Second Conference). *ASTM STP, 497*, 311–23.

Onal, L., & Adanur, S. (2002). Effect of stacking sequence on the mechanical properties of glass–carbon hybrid composites before and after impact. *J Ind Text, 31* (4), 255–271.

Park, R. & Jang, J. (1998). The effects of hybridization on the mechanical performance of aramid/polyethylene intraply fabric composites. *Comp. Sci. Technol. 58,* 1621–1628.

Parvatareddy, H., Wilson T. P. H, & Dillard D. A. (1996). Impact damage resistance and tolerance of high performance polymeric composites subjected to environmental aging. *Compos Sci Technol, 56,* 1129–40.

Pintado J. M., Carrion J. G., Garcı´a J. L., & Blas F. 1998. Mechanical behavior of composite materials at cryogenic temperatures. *In Proceedings of the Fourth European Conference Composites: Test Standard.*

Poe, C.C., Portnova, M.A., Sankar, B.V., & Jackson, W. C. (1991). Comparison of impact results for several polymeric composites over a wide range of low impact velocities. First NASA advanced Composites Technology Conference, *NASA Conference Publication 3104*, Part 1

Puente J. L., Zaera R., & Navarro C. (2002). The effect of low temperatures on the intermediate and high velocity impact response of CFRPs. *Composites: Part B, 33,* 559–566

Reed, R. P., & Golda, M. (1994). Cryogenic properties of unidirectional composites. *Cryogenics, 11*, 909–28.

Rojstaczer, S., Cohen, D., & Marom, G.. (1985). Thermal expansion of Kevlar fibers and composites. *J Mater Sci Lett*, 4, 1233.

Rydin, R. W. (1996). *Using the drop weight impact tower to assess impact resistance of FRP composite plates.* PhD Thesis, University of Delaware.

Sa´nchez, S. S., Go´mez-del, R. T., Barbero, E., Zaera, R., & Navarro, C. (2002). Static behavior of CFRPs at low temperatures. *Composites Part B, 33,* 383–90.

Sadasivam, B., & Mallick, P. K. (2002). Impact damage resistance of random fiber reinforced automotive composites*. J Thermoplast Compos Mater, 15,* 181–91.

Saka, K., & Harding, J. (1990). A simple laminate theory approach to the prediction of the tensile impact strength of woven hybrid composites. *Composites 21*, 439–447.

Sala, G. (2000) Composite degradation to fluid absorption. *Composites B, 31,* 357.

Samuel, I. I., Patrick, F. M., Guoqiang, L., Su-Seng, P., & Michael, A. S. (2007). Impact and post impact response of laminated beams at low temperatures, *Composite Structures, 79,* 12–17

Schutz, J. B. (1998). Properties of composite materials for cryogenic applications. *Cryogenics 38*, 3–12.

Sevkat, E., Liaw, B., Delale, F., & Raju, B. B. (2009). Drop-weight impact of plain woven hybrid glass–graphite/toughened epoxy composites. *Composites: Part A, 40*, 1090–1110.

Short, G. J., Guild, F. J., & Pavier, M. J. (2002). Post-impact compressive strength of curved GFRP laminates. *Composites Part A, 33*, 1487–95.

Smith, B.W., & Grove, R.A. (1989). Determination of crack propagation directions in graphite/epoxy structures. Composites and metals. *ASTM STP 948*, 154–173.

Son, K. H., & Kwon, Y. J. (2001). Effects of temperature on impact damages in CFRP composite laminates. *Composites Part B, 32,* 669–82.

Sonparote, P. W., & Lakkad, S. C. (1982). Mechanical properties of carbon/glass fibre reinforced hybrids, *Fiber Sci. Technol, 16,* 309–312.

Sreekala, M. S., George, J., Kumaran, M.G. & Thomas, S. (2002). The mechanical performance of hybrid phenol-formaldehyde-based composites reinforced with glass and oil palm fibres. *Comp. Sci. Technol, 62,* 339–353.

Street, K. N., Russell, A. J., & Bonsang, F. (1988). Thermal damage effects on delamination toughness of a graphit/epoxy composite. *Compos Sci Technol, 32*, 1–14.

Sugun, B. S., & Rao, R. M. (2004). Low velocity impact characterization of Glass, Carbon and Kevlar composites using repeated drop tests. *J Reinf Plast Compos, 23*, 1583–99.

Takeda, T. (1985). Impulsive response and fracture of composites (I). *J Jpn Soc Compos Mater, 11* (4), 151–161.

Tanaka T., &Kurokawa T. (1996). Damage and residual bending strength of graphite/epoxy composite laminates subjected to normal impact. *J Jpn Soc Aeronaut Space Sci*, 37, 29–36.

Thanomsilp, C. & Hogg, P. J. (2003). Penetration impact resistance of hybrid composites based on commingled yarn fabrics. *Comp. Sci. Technol, 63,* 467–482.

Tiberkak, R., Bachene, M., Rechak, S., & Necib, B. (2008). Damage prediction in composite plates subjected to low velocity impact. *Compos Struct*, *83,*73–82.

Timmerman, J. F., Tillman, M. S., Hayes, B. S., & Seferis, J. C. (2001). Matrix and fiber influences on the cryogenic microcracking of carbon fiber/epoxy composites. *Composites Part A: Appl Sci Manuf*, 33, 323–9.

Tjong, S. C., Xu, S. A. & Mai, Y. W. (2003). Impact fracture toughness of short glass fiber reinforced polyimide 6,6 hybrid composites containing elastomer particles using essential work of fracture concept. *Mater. Sci. Eng, A347,* 338–345.

Tjong, S. C., Xu, S. A., Li, R. K. & Mai, Y. W. (2002). Mechanical behavior and fracture toughness evaluation of maleic anhydride compatibilized short glass fiber/SEBS/polypropylene hybrid composites. *Comp. Sci. Technol, 62*, 831–840.

Wang, C. J., Jang, B. Z., Panus, J. & Valaire, B. T. (1991). Impact behavior of hybrid-fibre and hybrid-matrix composites. *Journal of Reinforced Plastics and Composites, 10,* 356–378.

Whittingham, B., Marshall, I. H., Mitrevski, T., & Jones R. (2004). The response of composite structures with pre-stress subject to low velocity impact damage. *Compos Struct 66,* 685–98.

Wu, H. Y. T., & Chang, F. K. (1989). Transient dynamic analysis of laminated composite plates subjected to transverse impact. *Comput Struct*, *31,* 453–66.

Yang, I.Y., Sim, J.K., & Im, K. H. (1996). Impact damages and residual bending strength of CFRP composite laminates subjected to impact loading. *KSME Int J, 10* (4), 423–434.

Young, D. & Sung, B. (1986). Horizontal wing structure of civil airplane using composite materials. *J Jpn Soc Aeronaut Space Sci* 34, 394; 608–618.

Zimmerman, R. S., & Adams, D.F. (1987). Impact performance of various fiber reinforced composites as a function of temperature. In: Proceeding of 32nd International SAMPE symposium. Anaheim, CA, 1461–71.